Effect of inhomogeneities on various astrophysical and cosmological processes in the Universe

Thesis submitted for the partial fulfillment of the requirements for the degree Doctor of Philosophy in Science
by

Shashank Shekhar Pandey

Department of Physics,
Faculty of Natural and Mathematical Sciences,
Presidency University,
Kolkata, India.
2025

Effect of inhomogeneities on various astrophysical and cosmological processes in the Universe

Thesis submitted for the partial fulfillment of the requirements for the degree Doctor of Philosophy in Science
by

Shashank Shekhar Pandey

Under the supervision of

Dr. Archan S. Majumdar,
Senior professor,
Dept. of Astrophysics & High Energy Physics,
S. N. Bose National Centre for Basic Sciences,
Kolkata, India

Department of Physics,
Faculty of Natural and Mathematical Sciences,
Presidency University,
Kolkata, India.
2025

Thesis Details

Thesis Title : Effect of inhomogeneities on various astrophysical and cosmological processes in the Universe

Name of the candidate : Shashank Shekhar Pandey

Registration No. : RC001-22RS209110344

Date of Registration : 12th August 2022

Department : Department of Physics

Shashank 12/08/25

Signature of the Candidate

To my parents, Sunita Pandey and Bal Bodh Pandey, and my sister, Vaishnavi Pandey, whose unwavering love, sacrifices, and guidance made this journey possible.

To Lord Shiva,

नमामीशमीशान निर्वाणरूपं
विभुं व्यापकं ब्रह्म वेदस्वरूपम्।
निजं निर्गुणं निर्विकल्पं निरीहं
चिदाकाशमाकाशवासं भजेऽहम्॥

"I bow to Lord Shiva, who embodies liberation, is all-pervading, the eternal essence of the Vedas and Brahman. Free from attributes, desires, and duality—He is pure consciousness residing in the infinite sky. I worship Him."

To Lord Hanuman,

अतुलितबलधामं हेमशैलाभदेहं, दनुजवनकृशानुं ज्ञानिनामग्रगण्यम्।
सकलगुणनिधानं वानराणामधीशं, रघुपतिप्रियभक्तं वातजातं नमामि॥

"(I Salute Sri Hanuman) Who is an Abode of Unparallel Power, and Whose Huge Body is like a Golden Mountain, Who is like a raging Fire over the Forest of Demons, and the Foremost among the Jnanis (the Wise ones), Who is a Storehouse of All Good Qualities and the Master of the Monkeys, Who is a Dear Devotee of Raghupati (Sri Rama) and the Son of Vayudeva; I Salute Sri Hanuman."

Acknowledgement

I would like to express my deepest gratitude to everyone who has supported and inspired me throughout my PhD journey.

First and foremost, I am profoundly grateful to my supervisor, Prof. Archan S. Majumdar, for allowing me to work under his guidance. His unwavering support, constant encouragement, and confidence in my abilities have been instrumental in shaping this thesis. Our insightful discussions not only strengthened my scientific reasoning but also broadened my perspective on the subject. I am especially thankful for the freedom he granted me to explore my research interests independently, which has been invaluable to my learning experience. I am also thankful to him for actively introducing me to our various collaborators, which has helped me in extending my scientific circle. He also allowed me to attend various conferences, for which I am thankful. I am also grateful for his prompt reviews of our manuscripts, which ensured timely submission and publication. I am also thankful for his advice and his prompt actions regarding various administrative issues that I faced during my PhD tenure.

I also extend my heartfelt gratitude to Prof. Sunandan Gangopadhyay, Dr. Ramakrishna Das, Prof. Soumen Mondal, and Dr. Tapas Baug for their invaluable guidance and enriching discussions - both scientific and beyond - which have deeply influenced my PhD journey. I am especially thankful to Sunandan Sir and Ramakrishna Sir for being part of my evaluation committee and for their patience and suggestions during my yearly evaluation talks.

A special thanks to my cosmology group members, past and present: Dr. Arnab Sarkar (Arnab da), Dr. Amna Ali (Amna di), Dr. Ashadul Halder (Ashadul da), and Shubhadeep Mukherjee. Their continued support, help and motivation helped me a lot through my PhD journey.

I am also grateful to my collaborators - Dr. Ruchika Kaushik, Dr. Shreya Banerjee, Dr. Andrew Miller, Dibash, and Charchit for their help and for introducing me to new avenues of cosmology.

A special thanks to the astrophysics group members at our department, past and present, for inviting me to be a part of their group and with whom I spent most of my time: Rajib, Dr. Subhajit Kar, Dr. Ruchi Pandey (Ruchi di), Dr. Gesesew Reta Habtie (Gessy), Dorothy, Usman, Nishant (Nishu), Ariful, Avijit, Aman, Tunir, Soumita, Avirup, Ajay, and others. I am especially grateful to Rajib, who was with me throughout these five years. His unwavering support during my toughest moments is something I will cherish forever. I am also grateful to Gessy, Dorothy, Sagar, and Usman for joining me for our night tea time and for all the laughs and talks.

I am also thankful to Shivani, though I met her very late in my PhD journey and that too for a short time but I will deeply cherish it.

To my fellow department members from the quantum information and high energy physics side: Arun da, Subhankar da, Soham, Ashis da, Arnab da - thank you for all the discussions, help, and for making this journey brighter.

I am also thankful to the SNB sports community for allowing me to be a part of the various sports groups. I started playing most of the sports after coming here, and it helped me a lot in keeping my mind fresh and energetic. Thanks especially to - Biswajit (Panda) da, Neeraj da, Premashish da, Arun bhaiya, Sanuja, Samrat, Ramu, Krishnendu (kaka) da, Sourav, Souvik, Gopi, Dibyajyoti (DJ) da, Shaheerah, and others.

To my SNB PhD 2020 friends - Koushik, Manoj, Soumen, Soham, Anirban, Shinjini, Sudipta, Indrajit, Riya, and others - thank you for your companionship and support. Your friendship brought a sense of belonging that enriched my Ph.D. experience in countless ways.

I am also thankful to my childhood friends - Vaibhav, Shubham, Abhinav, Shantanu, Amit, and others for their continuous encouragement and support. Also, thanks to my B.Sc. friends - Gopesh, Shantanu, Shashank, Gaurav and others and to my M.Sc. friends - Sachin, Neeraj, Pulkit, Pratik, Rahul and others.

I am also deeply thankful to my younger sister, Vaishnavi (Swadha), for being there with me and encouraging me. To my family - Pinku bhaiya, Geeta bhabhi, Fufa ji, Masi, Mausa, Tauji, Taiji, Gudiya didi, Jeeja ji, Doctor mama, Guddu mama, Raju mama, Shikha mami, and to my cousins - Aditya, Shivangi,

Chanchal Bhaiya, Rahul, Sani bhaiya - my deepest love and gratitude. Your unwavering support and affection mean the world to me.

To my Nana and Nani, I hope I have made you proud. Please keep watching over us.

Above all, words fall short of expressing my deepest gratitude to my parents for their unconditional love, encouragement, and unwavering belief in me. Your support has been my pillar of strength throughout this journey. Very few in our country are privileged enough to pursue a PhD without any economic pressure, and I am grateful to both of you for this privilege. I will be forever grateful for your sacrifices and presence in my life.

I am also thankful to the Council of Scientific and Industrial Research (CSIR), Govt of India, for fellowship support through the CSIR-JRF/SRF-NET fellowship. They have worked hard towards improving the fellowship disbursal mechanism and overall fellow experience. Their timely disbursal of fellowship and timely approvals of various requests have helped me a lot.

Finally, I sincerely thank the S. N. Bose National Centre for Basic Sciences (SNBNCBS), Kolkata, for its financial support and access to essential research facilities, which were instrumental in carrying out this work. I am also thankful for the financial support that I received for attending various national and international conferences during my tenure. I also extend my gratitude to Presidency University for offering the CRPI program to SNBNCBS students and providing valuable academic resources and opportunities.

Ishaklak 12/08/25

Signature of the candidate with date

Declaration

I hereby declare that this thesis contains original research work carried out by me under the guidance of Dr. Archan S. Majumdar, Senior Professor, Department of Astrophysics & High Energy Physics, S. N. Bose National Centre for Basic Sciences (SNBNCBS), Kolkata, India, as part of the PhD programme.

All information in this document has been obtained and presented in accordance with academic rules and ethical conduct.

I also declare that, as required by these rules and conduct, I have fully cited and referenced all materials and results that are not original to this work.

I also declare that this work has not been submitted for any degree, either in part or in full, to any other institute or University before.

Shashak 12/08/25

Signature of the candidate with date

सत्येन्द्र नाथ बसु राष्ट्रीय मौलिक विज्ञान केन्द्र
SATYENDRA NATH BOSE NATIONAL
CENTRE FOR BASIC SCIENCES
सत्येन्द्र नाथ वसु जातीय मौल विज्ञान केन्द्र

Certificate

This is to certify that the thesis entitled "Effect of inhomogeneities on various astrophysical and cosmological processes in the Universe" submitted by Shri Shashank Shekhar Pandey , Registration Number RC001-22RS209110344 and date of registration 12th August 2022, in partial fulfilment of the requirements for the award of "Doctor of Philosophy" , is a record of bonafide research work carried out by him under my supervision.

Neither his thesis nor any part of the thesis has been submitted for any degree/diploma or any other academic award anywhere before.

12/8/25

Dr. Archan S. Majumdar
Senior Professor
S. N. Bose National Centre
for Basic Sciences
Block-JD, Sector-III, Salt Lake
Kolkata-700106

Dr. Archan S. Majumdar

Senior Professor

Department of Astrophysics & High Energy Physics

S. N. Bose National Centre for Basic Sciences

Abstract

Astronomical surveys have revealed prominent inhomogeneity in matter distribution in the Universe. In this thesis, we analyze the effect of these matter distribution inhomogeneities on various astrophysical and cosmological processes. We have employed Buchert's averaging procedure to incorporate the effect of these inhomogeneities in our analysis.

In our first work, we analyze the effect of the matter distribution inhomogeneities on the redshift-dependent part of the gravitational wave amplitude. In the context of a toy model within the above framework, we first show how the redshift versus distance relation gets affected through the averaging process. We then study the variation of the redshift-dependent part of the observed GW amplitude for different combinations of our model parameters.

In our second work, we consider the propagation of gravitational waves (GWs) in the late-time Universe in the presence of matter distribution inhomogeneities, and we also consider the cosmic fluid to be viscous. In this work, we investigate the cumulative effect of inhomogeneities and viscosity of the cosmic fluid on the observables associated with the sources of the GWs. Employing Buchert's averaging procedure in the backreaction framework, we consider a model of spacetime in which matter is distributed inhomogeneously across space. Using the modified redshift versus distance relation, through the averaging process in the context of the model, we study the variation of the redshift-dependent part of the observed gravitational wave amplitude for different combinations of our model parameters while simultaneously considering damping of the gravitational wave amplitude due to the viscosity of the cosmic fluid.

In our next work, we formulate a model of spacetime with inhomogeneous matter distribution in multiple domains. In the context of the backreaction framework using Buchert's averaging procedure, we evaluate the effect of backreaction due to the inhomogeneities on the late-time global evolution of the Universe. We constrain the model parameters using observational analysis of the Union2.1 Type Ia supernova data employing the Markov Chain Monte Carlo method.

Finally, in our fourth and final work, we explore the 21-cm signal in our Universe containing an inhomogeneous matter distribution at considerably large scales. Employing Buchert's averaging procedure in the context of a model

of spacetime with multiple inhomogeneous domains, we evaluate the effect of our model parameters on the observable 21-cm signal brightness temperature. Our model parameters are constrained through the Markov Chain Monte Carlo method using the Union2.1 Type Ia supernova observational data.

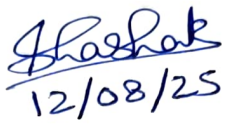

List of publications

Publications and communicated works relevant to the thesis:

- **Shashank Shekhar Pandey**, Arnab Sarkar, Amna Ali, A.S. Majumdar. "Effect of inhomogeneities on the propagation of gravitational waves from binaries of compact objects." In: *Journal of Cosmology and Astroparticle Physics* 2022.06 (2022), p. 021. DOI: 10.1088/1475-7516/2022/06/021. URL: https://dx.doi.org/10.1088/1475-7516/2022/06/021

- **Shashank Shekhar Pandey**, Arnab Sarkar, Amna Ali, Archan S. Majumdar. "Viscous attenuation of gravitational waves propagating through an inhomogeneous background." In: *The European Physical Journal C* 83.5 (2023), p. 435. ISSN: 1434-6052. DOI: 10.1140/epjc/s10052-023-11605-9. URL: https://doi.org/10.1140/epjc/s10052-023-11605-9

- Ashadul Halder, **Shashank Shekhar Pandey**, A.S. Majumdar. "Future deceleration due to backreaction in a Universe with multiple inhomogeneous domains." In: *Journal of Cosmology and Astroparticle Physics* 2023.08 (2023), p. 064. DOI: 10.1088/1475-7516/2023/08/064. URL: https://dx.doi.org/10.1088/1475-7516/2023/08/064

- **Shashank Shekhar Pandey**, Ashadul Halder, A. S. Majumdar. "Analyzing the 21-cm signal brightness temperature in the Universe with inhomogeneities." In: *Physical Review D* 110.4 (Aug. 2024). Publisher: American Physical Society, p. 043531. DOI: 10.1103/PhysRevD.110.043531. URL: https://link.aps.org/doi/10.1103/PhysRevD.110.043531 (visited on 09/24/2024)

Additional publications during the Ph.D. thesis but not forming part of it:

- Ashadul Halder, **Shashank Shekhar Pandey**, A. S. Majumdar. "Global 21-cm brightness temperature in viscous dark energy models." en. In: *Journal of Cosmology and Astroparticle Physics* 2022.10 (Oct. 2022). Publisher:

IOP Publishing, p. 049. ISSN: 1475-7516. DOI: 10.1088/1475-7516/2022/10/049. URL: https://dx.doi.org/10.1088/1475-7516/2022/10/049 (visited on 08/29/2023)

- **Shashank Shekhar Pandey**, Arnab Sarkar, Amna Ali, Archan S. Majumdar. "Effect of Inhomogeneities on the Propagation of Gravitational Waves from Binaries of Compact Objects." In: *Proceedings of the XXV DAE-BRNS High Energy Physics (HEP) Symposium 2022, 12–16 December, Mohali, India*. Ed. by Satyajit Jena et al. Singapore: Springer Nature Singapore, 2024, pp. 538–541. ISBN: 978-981-97-0289-3

Additional communicated article during the Ph.D. thesis but not forming part of it:

- Subhadeep Mukherjee, **Shashank Shekhar Pandey**, A. S. Majumdar. *Constraining the Hubble parameter with the 21 cm brightness temperature signal in a universe with inhomogeneities*. 2025. arXiv: 2505.22219 [astro-ph.CO]. URL: https://arxiv.org/abs/2505.22219

Contents

Table of Abbreviations

Abbreviation	**Full Form**
ΛCDM	Lambda Cold Dark Matter
CDM	Cold Dark Matter
FLRW	Friedman-Lemaître-Robertson-Walker
LSS	Large Scale Structure
SDSS	Sloan Digital Sky Survey
GA	Giant Arc
FRW	Friedman-Robertson-Walker
CM	Center of Mass
MCMC	Monte Carlo Markov Chain
SNe/SN	Super Novae
GW	Gravitational Waves
LIGO	Laser Interferometer Gravitational-Wave Observatory
aLIGO	advanced Laser Interferometer Gravitational-Wave Observatory
RHS	Right Hand Side
LHS	Left Hand Side
LISA	Laser Interferometer Space Antenna
EM	Electro-Magnetic
CMB	Cosmic Microwave Background
vΛCDM	viscous Lambda Cold Dark Matter
SIDM	Self-Interacting Dark Matter
v2d	viscous 2-domain inhomogeneous model
EDGES	Experiment to Detect Global Epoch of reionization Signal
SARAS	Shaped Antenna measurement of the background RAdio Spectrum
PBH	Primordial Black Holes

List of Figures

Chapter 1

General Introduction

1.1 Motivation

Cosmology is the scientific discipline that studies the universe's origin, structure, evolution, and eventual fate. It uses observations and theoretical models to understand the universe's largest scales. However, our ability to observe the universe is constrained. Also, the most widely recognized and successful theory governing the dynamics of the universe is general relativity, but its overwhelming complexity presents a significant challenge.

These limitations have compelled cosmologists to make simplifying assumptions to build a general relativistic model of our universe, which data can constrain. The Cosmological Principle is one such assumption. It states that the universe is homogeneous and isotropic on the largest of scales. This principle led to the formation of the Friedman-Lemaître-Robertson-Walker (FLRW) class of cosmological models, constituting the groundwork of most modern cosmology.

The modern paradigm of cosmology, the Lambda Cold Dark Matter (ΛCDM) model, is an FLRW model comprising four energy components: the cosmological constant Λ, symbolizing dark energy; cold dark matter (CDM); along with ordinary matter and radiation, as defined in the standard model of particle physics.

While the ΛCDM model has effectively established the foundational concepts of standard cosmology and generally aligns well with the observed data, it has faced certain conflicting observations [1–5], with the Hubble tension being particularly notable [6, 7]. Additionally, there are fundamental enigmas - physically unexplained dark elements making up 95% of the universe's energy content. Due to the limited theoretical understanding of the parameters in the ΛCDM model, particularly the cosmological constant, it is primarily considered a phenomenological fit rather than a thoroughly understood theory. Its effectiveness does not eliminate the likelihood that an entirely different model might align well with the data.

In addition, recent observations of large-scale structures (LSS) suggest the pos-

sibility of incorporating further elements into the standard cosmology framework. While the universe appears homogeneous and isotropic on the largest scales, numerous astrophysical surveys have detected significant inhomogeneities in matter distribution extending to substantial length scales.

In [8], the authors analyzed galaxy large-scale structures using the Sloan Digital Sky Survey (SDSS). They found indications that galaxy structures are associated with large-amplitude density fluctuations across various scales, constrained solely by the scale of the sample used. They also reported that these inhomogeneities do not reconcile with the predictions of standard theoretical cosmological models, and are also in conflict with mock catalogues of cosmological N-body simulations.

In [9], the researchers examined the Sloan Digital Sky Survey-DR7 catalogue focusing on luminous red galaxies. The study found notable deviations, exceeding 3σ, from the ΛCDM mock catalogues on samples of luminous red galaxies up to 500 h^{-1} Mpc, and observed minor deviations of approximately 2σ at 700 h^{-1} Mpc.

Recently, a Giant Arc (GA) of galaxies with a proper size of approximately 1 Gpc at the present epoch has been discovered [10]. The GA is one of the newest and largest structures within a growing collection of extensive LSSs that could potentially (though carefully) question the Cosmological Principle that underpins the 'standard model' of cosmology.

The persistent complexity in the distribution of matter within our universe, as explored since the inception of FLRW cosmology, could potentially question the validity of the assumptions of homogeneity and isotropy that form the basis of both the FLRW model class and the ΛCDM model.

Inhomogeneous cosmology is a branch of cosmology that aims to tackle the main issues of the ΛCDM model within the context of general relativity's gravitational framework. This area of study focuses on the complex dynamics of spacetime that emerge when matter is distributed inhomogeneously across the spatial sections of our universe. Researchers in inhomogeneous cosmology aim to investigate the limitations of the FLRW model in providing a precise depiction of large-scale geometry and serving as the global background metric for cosmic structures.

The premise of the FLRW model is that when averaged over large scales, the universe appears to be homogeneous and isotropic. According to this proposition, one first takes the average of the metric and the energy-momentum tensor, then plugs these smooth quantities into the Einstein equation. However, physically, one should first plug the inhomogeneous quantities into the Einstein equation and then take the average. Because the Einstein equation is non-linear, these two procedures are not equivalent. The idea that the average behaviour of inhomogeneous and/or anisotropic spacetimes generally differs from that of homogeneous

and isotropic spacetimes goes back to 1963 [11, 12]. George Ellis in 1983 gave the first comprehensive discussion [13, 14] and called finding the smooth metric which best fits the real clumpy universe the fitting problem. The difference between the behaviour of the average and smooth quantities and the influence of inhomogeneity and/or anisotropy on the average behaviour is also known as backreaction [15–17]. The way in which physics on small and intermediate scales affects or is 'reacting back' on the large-scale dynamical description of the universe is a central concept in inhomogeneous cosmology. In the present era of precision cosmology, the cosmological backreaction warrants special attention.

Einstein and Straus in 1945 developed the Swiss cheese class of space-times, which was one of the first frameworks for addressing inhomogeneous and anisotropic models in cosmology [18]. The Swiss cheese models enable the examination of non-perturbative structures within a general relativistic context, albeit in a notably simplified scenario where the Schwarzschild solution represents compact objects within an FLRW spacetime.

Toshifumi Futamase in [19] devised an approximation method to build a metric depicting a realistic, clumpy universe within the framework of general relativity. This involved spatial averaging to illustrate how the universe's expansion is collectively driven by matter clumps. Futamase and Sasaki's work in [20] explored how inhomogeneities in matter distribution affect electromagnetic wave propagation by employing an approximate metric suitable for an inhomogeneous Universe. From this analysis, they formulated a generalized distance-redshift relation applicable to an inhomogeneous Universe.

The intricacies of general relativity, coupled with the challenges of addressing the Einstein equations for non-uniform matter distributions and evaluating the implications through tensorial averaging methods, have led to the development of various strategies to tackle this issue [15]. Numerous specifications and approaches can be pursued to address the diverse aspects of the broad challenges present in inhomogeneous cosmology. An averaging process is essential to analyze the impact of inhomogeneities on the universe's evolution. Several types of averaging methods have been proposed in the literature [13, 19, 21].

One notable method for handling relativistic averaging in cosmology is the tensor averaging framework developed by Zalaletdinov [22–24]. Zalaletdinov introduced a covariant and exact averaging procedure wherein an averaged version of Einstein's equations was attained using a covariant averaging scheme of tensors via bilocal operators. In this method of averaging, the complete tensorial Einstein field $G_{\mu\nu} = \frac{8\pi G}{c^4} T_{\mu\nu}$, where $G_{\mu\nu} = R_{\mu\nu} - \frac{1}{2} g_{\mu\nu} R$ represents the Einstein tensor, is averaged to produce a new system of covariant equations at a specific scale $\langle G \rangle_{\mu\nu} = \frac{8\pi G}{c^4} \langle T \rangle_{\mu\nu}$, with $\langle\rangle$ symbolizing a particular averaging process that maintains the covariance of any averaged tensorial field. Notably, the averaged

Einstein equations typically are not resolved by the averaged metric $\langle g \rangle_{\mu\nu}$ derived from the same averaging technique. The discrepancy between the Einstein tensor of $\langle g \rangle_{\mu\nu}$ (i.e., $G_{\mu\nu}(\langle g_{\mu\nu} \rangle)$) and the averaged local Einstein tensor $\langle G \rangle_{\mu\nu}$ can be termed the backreaction term. Although Zalaletdinov's averaging framework retains the tensorial structure of the Einstein equations, it introduces extra complexity into the averaging operation, which lacks substantial physical justification. Moreover, the complexity of this averaging procedure renders the application of theoretical results to specific cases challenging.

The averaging method utilized in this thesis originates from the work of Thomas Buchert [25, 26]. It employs a truncated hierarchy focusing on the averaged scalar components of Einstein's equations and is the most prevalent averaging strategy in the field of inhomogeneous cosmology. Buchert's procedure simplifies the problem by concentrating solely on the averaging of scalar quantities, effectively reducing the task to solving three coupled equations with four independent variables that describe the state of a spatial region in the universe: its volume, mean density, average scalar curvature, and backreaction. This backreaction reflects the domain's inhomogeneity level.

Within Buchert's framework [25–27], the temporal progression of spatial averages diverges from what is expected using the evolved spatial metric. This discrepancy leads to the introduction of a geometrical backreaction term, which accounts for deviations from the typical behavior predicted by the Friedmann equations. Buchert's averaging scheme offers a novel perspective on the large-scale expansion of the universe without assuming uniformity. Several studies have explored the possibility of explaining the accelerated expansion of the universe in its later stages through backreaction [17, 28–31].

The disadvantage of Buchert's scheme is that it does not establish a definition for the averaging of tensors, which means that it lacks natural definitions for elements like averaged tensorial fluid variables or an averaged metric tensor.

One advantage of the Buchert approach is that it provides a clear and intuitive set of equations for the averaged variables of spacetime. These dynamical equations can be reshaped to resemble the FLRW equations typical in conventional cosmology, enabling a direct comparison to identify differences in dynamical behavior. The elements influencing the dynamics of a region that do not have an FLRW equivalent are labeled as backreaction terms. This measurement of backreaction is important because it highlights the potential emergence of effective energy sources that exhibit dark energy-like characteristics, arising from structures at smaller scales [32].

[33, 34] outline a method to connect the global variables from Buchert's framework to the observations made by 'typical observers' within statistically homogeneous and isotropic universes. In their approach, the average redshift and

average angular diameter distance as perceived by several typical observers are examined. This offers a conceptual understanding of how average quantities on spatial surfaces might relate to measurements made by typical observers, though it is largely reliant on assumptions regarding statistical homogeneity, isotropy, and the pace of structural evolution rather than precise derivations. Through Buchert's averaging method, it's demonstrated that spatial averaging impacts the redshift-distance relation [33–38]. The relationship between spatial averages and the redshift-distance correlation has undergone further scrutiny [35, 37]. In this thesis, we are motivated to utilize Buchert's averaging procedure as it offers a framework for linking our theoretical computations (spatial averages) with observational data (redshift-distance relations) [33–35].

Numerous investigations within Buchert's framework aim to understand how matter inhomogeneities impact large-scale cosmological dynamics, as well as light and gravitational wave propagation [17, 27, 29, 30, 33–36, 39–58]. The comprehensive effects of cosmic backreaction on the universe's evolution remain disputed [31], yet theoretically, backreaction could influence cosmic evolution [39].

Research investigating the impact of matter inhomogeneities on large-scale cosmological dynamics and light propagation has been conducted independently of Buchert's averaging method as well [21, 38, 59–66].

Investigating the role of local inhomogeneities has led to intriguing effects regarding electromagnetic wave propagation in the averaged universe. Research into the behavior of photons in an averaged geometry has been conducted [33, 34, 64], with some employing a gauge-invariant technique for averaging over the past null cone [21, 59]. Other investigations have examined light propagation through inhomogeneous Swiss-cheese models by reproducing the Hubble diagram [65–67]. A derived version of the averaged null geodesic equation [58] reveals that the equation for light propagation incorporates an effective Hubble parameter for the averaged spacetime, which differs from that of a homogeneous spacetime.

Averaging over inhomogeneities leads to modified cosmological-distance versus redshift relations [35, 36]. This adjustment presents intriguing consequences for identifying signs of inhomogeneity by using measurements of the cosmic expansion rate [42].

The various studies mentioned for establishing a macroscopic cosmological model of our universe aim to illustrate the complexity and richness encountered in inhomogeneous cosmology when developing a macroscopic dynamic theory of the universe, and motivate us to further contribute to this rich domain of cosmology.

1.2 Brief Outline of the thesis

This thesis explores the effect of including matter distribution inhomogeneities in the universe in analyzing various astrophysical and cosmological processes. By carefully formulating various models of inhomogeneous matter distribution, it aims to examine multiple phenomena of our universe. A brief overview of the thesis is given as follows:

(Chap. 2) thoroughly presents the averaging procedure employed in this thesis. It begins with an in-depth introduction of Buchert's averaging procedure. We derive Buchert's equations and discuss their similarities and differences with the FLRW equations. We also discuss how the acceleration of spacetime can occur within this framework. We also highlight the specific framework that we have employed in this thesis and show the separation formulas for arbitrary partitions.

In (Chap. 3) we present our first analysis based on one of our work [47], where we examined the effect of matter distribution inhomogeneities on gravitational wave (GW) observables, specifically on the redshift-dependent part of the GW amplitude. In the context of a toy model within our backreaction framework, we initially demonstrate the impact of the averaging process on the redshift-distance relationship. Subsequently, we analyze how the redshift-dependent part of the GW amplitude changes with various model parameter combinations. Our findings reveal that the variation in GW amplitude with redshift can substantially differ from what is observed in the ΛCDM model. This underscores the crucial role of local inhomogeneities in the precise measurement of gravitational wave source parameters.

Next, we carry this analysis forward by now incorporating viscous matter along with matter distribution inhomogeneities. In (Chap. 4), which is based on our work [48], where we investigate the viscous attenuation of GW in a universe with matter distribution inhomogeneities. As with the previous analysis, here also the averaging procedure will modify the Hubble dynamics as compared to FLRW models, which results in a modified redshift-distance relation. We subsequently examine how the redshift-dependent component of the GW amplitude varies while simultaneously taking into account the attenuation of the amplitude caused by the cosmic fluid's viscosity. Our analysis reveals substantial deviations following the inclusion of viscous attenuation, which vary based on the selected values of our model parameters. Our findings underscore the significant role of viscosity in the context of an inhomogeneous Universe model, particularly relevant for the accurate measurement of parameters related to compact-binary gravitational wave sources.

In (Chap. 5), which is based on our work [53], we investigated the future deceleration due to backreaction in a universe with multiple inhomogeneous domains.

We develop a spacetime model characterized by an inhomogeneous matter distribution across multiple sub-domains. Within the backreaction framework, utilizing Buchert's averaging method, we assess the impact of inhomogeneities on the Universe's late-time global evolution. Upon studying this universe's future trajectory, we observe a potential shift from the current accelerating phase to one of deceleration, dictated by specific model parameters. We constrain our model parameters using observational analysis of the Union2.1 supernova Ia dataset using the Markov Chain Monte Carlo (MCMC) method.

In (Chap. 6), which is based on our work [68], we analyzed 21 cm brightness temperature in a universe with inhomogeneous matter distribution. We investigate the 21-cm signal within our Universe, which features a non-uniform distribution of matter on significantly large scales. By utilizing Buchert's averaging approach within a spacetime framework consisting of several inhomogeneous domains, we analyze how our model parameters influence the observable brightness temperature of the 21-cm signal. These parameters are constrained by employing the Markov Chain Monte Carlo method using the Union2.1 supernova Ia data. Our results indicate that the presence of inhomogeneities in the Universe may lead to a significant dip in brightness temperature compared to the ΛCDM model prediction.

In (Chap. 7), we conclude the thesis by giving a brief summary and possible future directions.

Chapter 2

Formalism

In this thesis, Buchert's averaging procedure has been used for incorporating matter distribution inhomogeneities in the analysis.

In this averaging procedure, matter is characterized as an irrotational ideal fluid with zero pressure [17, 25].

In this averaging procedure, notions of proper time and scale factor and the relation between redshift and scale factor are implemented in the same way as in the FRW case. The reliance on proper time can similarly be articulated in terms of redshift, just like in the FRW scenario [17].

Even though inhomogeneities and anisotropies might be averaged out on larger scales, enabling the FRW scale factor to serve as a reasonable description, it does not follow that the FRW metric truly reflects the average geometry. This stems from the fact that the FRW metric assumes spatial curvature as homogeneous and isotropic, whereas in a typical spacetime, the spatial curvature is in fact inhomogeneous and anisotropic. Moreover, its evolution diverges from the evolution of FRW spatial curvature, even on average. This disparity arises because regions with positive and negative curvature evolve in distinct, uncorrelated ways, which prevents the manifestation of FRW-like characteristics [17].

From a physical standpoint, areas exhibiting negative spatial curvature tend to expand more rapidly than those with positive spatial curvature, leading to the expectation that these regions will eventually occupy most of the volume, rendering the average spatial curvature negative. The distinctive evolution of spatial curvature, along with the interplay between overdense and underdense regions, is key to the backreaction theory proposed to explain accelerated expansion. The dynamics of spatial curvature is fundamental to understanding when the scale factor accurately represents the universe and when it adheres to the FRW equations [17].

We will assume that the average properties of the universe can be described in terms of an overall scale factor without deriving the conditions under which this assumption is valid [17].

To find the correct dynamical equations, merely plugging the overall scale factor into the Einstein equation is inadequate. Rather, the complete inhomogeneous and/or anisotropic metric should be incorporated into the Einstein equation, followed by averaging. This approach is necessary because the averaged dynamics of an inhomogeneous and/or anisotropic spacetime differ from those of a smooth spacetime, despite having the same initial conditions. In essence, the average characteristics of an inhomogeneous and/or anisotropic spacetime fail to satisfy the Einstein equation. There is a common misconception that substituting an averaged metric directly into the Einstein equation yields the same result as inserting the actual metric into the equation and then averaging it. This discrepancy arises due to the non-linear nature of the Einstein tensor $\mathsf{G}_{\mu\nu}$ with respect to the metric, leading to $\langle \mathsf{G}_{\mu\nu}(g_{\alpha\beta})\rangle \neq \mathsf{G}_{\mu\nu}(\langle g_{\alpha\beta}\rangle)$, where $\langle\rangle$ denotes the process of averaging. A more precise explanation is that the issue stems from the fact that averaging and time evolution do not commute [17].

The prevailing belief is that even when non-linear structures commence forming, the mean behavior aligns with the FRW equations when smoothing is conducted on the scale of these nonlinearities. However, this assumption is contradicted by the derivation of equations governing average expansion [25, 26, 69]. The existence of inhomogeneities and anisotropies influences the way the scale factor evolves. Moreover, neither the statistical homogeneity and isotropy nor the fact that inhomogeneous and anisotropic areas are relatively minor in size compared to the visual horizon is adequate to reinstate FRW dynamics. [17].

2.1 The Buchert's equations

We consider the universe's matter to be representable as dust, which is effectively a pressureless ideal fluid. Additionally, we assume that this dust exhibits no rotation, meaning it has zero vorticity. These assumptions are made to make our calculations easier, as now there won't be any pressure and vorticity-related terms. In this case, the flow is geodesic. Geodesic motion ensures the existence of spacelike hypersurfaces everywhere orthogonal to the dust four-velocity, enabling a clean 3+1 split and unambiguous spatial averages [17, 25, 27].

The Einstein's equations are

$$R_{\mu\nu} - \frac{1}{2} g_{\mu\nu} R = 8\pi G \rho u_\mu u_\nu - \Lambda g_{\mu\nu} \tag{2.1}$$

where, $R_{\mu\nu}$ is the Ricci tensor, R its trace, $u_{\mu\nu}(u_{\mu\nu}u^{\mu\nu} = -1)$ is the fluid's 4-velocity, Λ is the cosmological constant and ρ is the rest mass density. ρ obeys the conservation law

$$(\rho u^\mu u^\nu)_{;\mu} = 0 \tag{2.2}$$

We select a coordinate system that is orthogonal to the flow, specifically Gaussian or normal coordinates, that move with the fluid, expressed as $x^\mu = (t, X^k)$. Consequently, we have $u_\mu = (-1, 0, 0, 0)$ and $u^\mu = (1, 0, 0, 0)$. These coordinates are used to mark geodesics in spacetime, meaning $u^\nu u^\mu_{;\nu} = 0$. By opting for a zero 3-velocity, the coordinates are inherently comoving.

Then the metric can be written in the synchronous gauge [17, 70, 71]

$$ds^2 = -dt^2 + {}^{(3)}g_{ij}dX^i dX^j, \tag{2.3}$$

where t is the proper time that labels the hypersurfaces, X^i are Gaussian normal coordinates in the hypersurfaces, and g_{ij} is the full inhomogeneous spatial three-metric of the hypersurfaces of constant t. The Einstein equation (Eq. 2.1) gives us the following three exact, local, covariant scalar equations

$$\dot{\theta} + \frac{1}{3}\theta^2 = -4\pi G\rho - 2\sigma^2 + \Lambda \tag{2.4}$$

$$\frac{1}{3}\theta^2 = 8\pi G\rho - \frac{1}{2}{}^{(3)}R + \sigma^2 + \Lambda \tag{2.5}$$

$$\dot{\rho} + \theta\rho = 0 \tag{2.6}$$

where a dot indicates differentiation with respect to t. The expansion rate of the local volume element is given by $\theta(t, X^k) = (\sqrt{{}^{(3)}g})^{-1}\partial_t(\sqrt{{}^{(3)}g})$, while the scalar $\sigma^2(t, X^k) = 2\sigma^{ij}\sigma_{ij} \geq 0$ is derived from the shear tensor σ_{ij}. Here, Λ represents the cosmological constant, and ${}^{(3)}R(t, X^k)$ denotes the Ricci scalar of the hypersurface at a constant t, which corresponds to the spatial curvature. The acceleration equation (Eq. 2.4) is known as the Raychaudhuri equation, and the Hamiltonian constraint is outlined in (Eq. 2.5).

Converting the Einstein equation into a set of scalar equations results in an open system: although we have three equations, there are four independent variables involved. Essentially, it is not possible to reduce the evolution of the shear tensor (or, equivalently, the Ricci tensor on the hypersurface where t is constant) to just one scalar equation. The integrability condition between (Eq. 2.4) and (Eq. 2.5) is

$$\partial_t\left({}^{(3)}R\right) + \frac{2}{3}\theta\,{}^{(3)}R = 2\partial_t\sigma^2 + 4\theta\sigma^2, \tag{2.7}$$

so specifying either the shear or the spatial curvature fixes the other. Note that no approximations have been made: the equations (Eq. 2.4)-(Eq. 2.6) are exact for irrotational dust, with arbitrarily large density variations.

Deriving the Buchert's equations

We are concerned with the evolution of average quantities, with particular interest in how the average expansion rate changes. To explore this, we adhere to the framework established by [17, 25, 27]. The spacetime is divided into flow-orthogonal hypersurfaces, which are characterized by a metric g_{ij} as outlined in (Eq. 2.3) and a proper time t. Our objective is to examine the evolution of a compact spatial domain D, which moves with the fluid on these hypersurfaces. This comoving attribute ensures that the domain remains embedded within the general three-metric, meaning its configuration reflects the geometric structure of local inhomogeneities. A key quantity defining such a domain is its volume, which is the exclusive measure utilized here since we aim to address inquiries concerning the domain sizes and their temporal changes. The volume of a compact spatial domain D on these hypersurfaces is defined as [27]

$$V_D := \int_D d\mu_g \tag{2.8}$$

where $d\mu_g := \sqrt{{}^{(3)}g(t, X^1, X^2, X^3)}dX^1dX^2dX^3$. In order to characterize the average evolution and juxtapose it with FRW models, a scale factor must be defined. The most straightforward way to extend the concept of a universal scale factor to an inhomogeneous or anisotropic spacetime is to define it using the volume of the hypersurface where t remains constant. Therefore, we define a dimensionless ('effective') scale factor via the volume

$$a_D(t) := \left(\frac{V_D}{V_{D_0}}\right)^{1/3}, \tag{2.9}$$

normalized by the volume of the initial domain V_{D_0}, which can be considered the volume of the domain at the present time t_0. Therefore, at present time t_0, $a_D(t_0) = 1$. The average over a scalar quantity f is defined as,

$$\langle f\rangle_D(t) := \frac{\int_D f(t, X^1, X^2, X^3)d\mu_g}{\int_D d\mu_g} \tag{2.10}$$

where the integral is over the hypersurface of constant t. An important property of the averaging (Eq. 2.10) is that it does not commute with time evolution,

$$\partial_t\langle f\rangle_D = \langle\partial_t f\rangle_D + \langle f\theta\rangle_D - \langle f\rangle_D\langle\theta\rangle_D \tag{2.11}$$

The averaged expansion rate may be written in terms of the scale factor,

$$\langle\theta\rangle_D = \frac{\dot{V}_D}{V_D} = 3\frac{\dot{a_D}}{a_D} \tag{2.12}$$

We will also use the notation $H_D \equiv \dot{a_D}/a_D$.

Using this averaging procedure (Eq. 2.10) with the scalar equations (Eq. 2.4

- Eq. 2.6) and commuting the time derivatives as shown in (Eq. 2.11), we get evolution equations satisfied by the scale factor (Eq. 2.9) and first derived by Buchert,

$$3\frac{\ddot{a_D}}{a_D} = -4\pi G\langle\rho\rangle_D + Q_D + \Lambda \tag{2.13}$$

$$3H_D^2 = 8\pi G\langle\rho\rangle_D - \frac{1}{2}\langle{}^{(3)}R\rangle_D - \frac{1}{2}Q_D + \Lambda \tag{2.14}$$

$$0 = \partial_t\langle\rho\rangle_D + 3H_D\langle\rho\rangle_D \tag{2.15}$$

where $\langle\rho\rangle_D$, $\langle{}^{(3)}R\rangle_D$ and H_D are the averaged matter density, averaged spatial Ricci scalar and the Hubble parameter ($H_D := \dot{a_D}/a_D$) of the domain D, respectively. The necessary condition of integrability connecting (Eq. 2.13) and (Eq. 2.14) is given by,

$$\frac{1}{a_D^2}\partial_t(a_D^2\langle{}^{(3)}R\rangle_D) + \frac{1}{a_D^6}\partial_t(a_D^6 Q_D) = 0. \tag{2.16}$$

Q_D is called the kinematical backreaction, which is a new term compared to the FRW equations, containing the effect of inhomogeneity and anisotropy, and is defined as

$$Q_D := \frac{2}{3}(\langle\theta^2\rangle_D - \langle\theta\rangle_D^2) - 2\langle\sigma^2\rangle_D, \tag{2.17}$$

where θ is the local expansion rate and $\sigma^2 := 1/2\sigma_{ij}\sigma^{ij}$ is the squared rate of shear. The Hubble parameter, denoted as H_D, is linked to $\langle\theta\rangle_D$ through the equation $H_D = \frac{1}{3}\langle\theta\rangle_D$. (Eq. 2.17) comprises the variance in local expansion rates, expressed as $\langle\theta^2\rangle_D - \langle\theta\rangle_D^2$, along with the averaged shear scalar $\langle\sigma^2\rangle_D$ across the specified domain. For a homogeneous domain, this value is zero. Hence, it characterizes deviations from homogeneity and is supposed to hold significance, especially during the late, inhomogeneous phases of the universe leading up to structure formation.

(Eq. 2.16) highlights a key aspect of the averaged equations by coupling the evolution of the average intrinsic curvature ($\langle R\rangle_D$) with the kinematical backreaction term (Q_D). This term reflects the impact of matter inhomogeneities within the analysis. The connection between $\langle R\rangle_D$ and Q_D, alongside the Q_D term, signifies the departure from uniformity. Unlike the typical Friedmannian model, here the curvature term does not adhere to an a_D^{-2} scaling constraint; rather, it remains variable as it can be an arbitrary function of a_D. It is crucial to note that the significant influence of backreaction models stems not from the large size of Q_D, but from the dynamic interplay of a non-zero Q_D with the averaged scalar curvature, altering its temporal dynamics.

The Buchert equations (Eq. 2.13 - Eq. 2.15) provide an exact description of the

averages when matter manifests as irrotational dust. The backreaction variable, Q_D, consists of two elements: the expansion rate's variance and shear. Shear is also found in the local equation (Eq. 2.4), where it contributes to slowing down the expansion. On the other hand, the variance appears solely in the averaged equations due to the non-commutation of averaging and time derivative operations as demonstrated in (Eq. 2.11), and it tends to accelerate the expansion rate. Consequently, the Buchert equations suggest that the FRW equations are not applicable in the presence of significant inhomogeneities. Notably, the average acceleration (Eq. 2.13) can turn positive if the expansion rate's variance is substantial ([16]).

We can also define cosmological parameters on the domain investigated. Similar to the Friedmannian case, they are derived from the Hamilton constraint (Eq. 2.14) by a division by $3H_D^2$. For different spatial domains, the global domain, and the individual subdomains, we generically formulate the cosmological parameters by taking $\mathcal{F}$ to denote one of the domains - the global domain or one of the subdomains. The definitions are

$$\begin{aligned} \Omega_m^{\mathcal{F}} &:= \frac{8\pi G}{3H_D^2}\langle\rho\rangle_D; & \Omega_\Lambda^{\mathcal{F}} &:= \frac{\Lambda}{3H_D^2} \\ \Omega_R^{\mathcal{F}} &:= -\frac{\langle R\rangle_{\mathcal{F}}}{6H_D^2}; & \Omega_Q^{\mathcal{F}} &:= -\frac{Q}{6H_D^2} \end{aligned} \tag{2.18}$$

Using these definitions, the Hamiltonian constraint (Eq. 2.14) for a domain $\mathcal{F}$ reads,

$$\Omega_m^{\mathcal{F}} + \Omega_\Lambda^{\mathcal{F}} + \Omega_R^{\mathcal{F}} + \Omega_Q^{\mathcal{F}} = \frac{H_{\mathcal{F}}^2}{H_D^2} \tag{2.19}$$

which implies that within the domain D, the dimensionless parameters Ω sum to 1. However, outside of this domain, their sum could be any positive value, largely influenced by whether the corresponding region $\mathcal{F}$ is expanding faster or slower relative to the region D.

Recovering the FRW equations

As with the system comprising equations (Eq. 2.4 - Eq. 2.7), the set of equations (Eq. 2.13 - Eq. 2.16) includes only three independent equations for four independent functions: a, ρ, Q, and $\langle {}^{(3)}R\rangle$. This implies that various inhomogeneous or anisotropic spacetimes may undergo distinct evolution even if they start with the same average initial conditions. Although solving equations (Eq. 2.13 - Eq. 2.16) is not feasible, they can be used to verify if a specific scale factor might be a consequence of backreaction [55].

Designating an additional function (or defining a relationship among the four functions) results in a solvable system. Particularly, in the case where the shear and the expansion rate's variance are minimal relative to the energy density's influence, the Buchert equations simplify to the FRW equations. Conversely, if either the shear or the variance of the expansion rate plays a major role compared to the energy density in a substantial portion of space, then the FRW equations no longer provide an accurate approximation for average behavior. This method derives the FRW equations and also determines their range of applicability.

When shear and expansion rate variance negate each other, the average behavior aligns with the FRW equations, even if these factors are significant. Notably, the expansion depicted by the Buchert equations (Eq. 2.13 - Eq. 2.16) won't conform to FRW behavior when the spatial scale of inhomogeneities and anisotropies is small. If shear or expansion rate variance matches the contribution of energy density in a substantial space region, the resultant behavior will deviate from the FRW model, regardless of the limited size of individual inhomogeneous or anisotropic areas. The expansion rate's variance is inherently non-negative, only disappearing in a uniformly homogeneous expansion: contributions from various inhomogeneous regions can't nullify each other completely. This principle also applies to shear. (Shear and variance from diverse regions can potentially cancel each other out.) The Buchert equations (Eq. 2.13 - Eq. 2.16) concretely depict and measure the initial assertion of this chapter, that large-scale statistical homogeneity and isotropy don't guarantee the scale factor's dynamics conform to the FRW equations.

Acceleration without acceleration

The averaged Raychaudhuri equation (Eq. 2.13) reveals that when the variance of the expansion rate is much larger than that of shear and energy density, the overall expansion can undergo acceleration, even though the local expansion rate is decelerating at every point, as described by the local Raychaudhuri equation (Eq. 2.4). This potential for acceleration is a characteristic of the averaged system and does not manifest in the local behavior. It emerges from the non-commutativity of averaging and time evolution.

Since $\mathcal{Q}$ positively affects acceleration (Eq. 2.13) yet negatively influences the Hubble rate (Eq. 2.14), it might appear that negative curvature is required to counterbalance $\mathcal{Q}$'s negative effect on the Hubble rate, as suggested in [55]. However, acceleration can occur even with a positive spatial curvature, as the key condition is that the sum $-\langle {}^{(3)}R\rangle - \mathcal{Q}$ increases (meaning it becomes less negative). This implies that $\langle {}^{(3)}R\rangle$ must decrease (i.e., $-\langle {}^{(3)}R\rangle$ should increase) more rapidly than $\mathcal{Q}$ grows. According to (Eq. 2.16), acceleration inherently involves

non-FRW spatial curvature: if $\langle {}^{(3)}R\rangle \propto a^{-2}$, then $Q \propto a^{-6}$, resulting in no acceleration.

2.1.1 Separation formulas for arbitrary partitions

We now adopt a particular method within the Buchert formalism, in which ensembles of disjoint regions represent the global domain [27, 29, 30, 35, 36, 39–52]. Here, the global domain D is partitioned into subregions F_l consisting of elementary space entities $F_l^{(\alpha)}$. Therefore, mathematically, we have $D = \cup_l F_l$, where $F_l := \cup_\alpha F_l^{(\alpha)}$ and $F_l^{(\alpha)} \cap F_m^{(\beta)} = \emptyset$ for all $\alpha \neq \beta$ and $l \neq m$.

Average of a scalar-valued function f on the domain D is given by,

$$\begin{aligned}\langle f\rangle :&= |D|_g^{-1}\int_D f d\mu_g = \sum_l |D|_g^{-1}\sum_\alpha \int_{F_l^{(\alpha)}} f d\mu_g \\ &= \sum_l \frac{|F_l|_g}{|D|_g}\langle f\rangle_{F_l} = \sum_l \lambda_l \langle f\rangle_{F_l}\end{aligned} \tag{2.20}$$

where

$$\lambda_l := \frac{|F_l|_g}{|D|_g} \tag{2.21}$$

is the volume fraction of the subregion F_l such that $\sum_l \lambda_l = 1$ and $\langle f\rangle_{F_l}$ is the average of f on subregion F_l. The scalar quantities ρ, R and H_D are governed by (Eq. 2.20) but Q_D due to the presence of $\langle\theta\rangle_D^2$ - term, do not adhere to the above equation and instead follow,

$$Q_D = \sum_l \lambda_l Q_l + 3\sum_{l\neq m}\lambda_l\lambda_m(H_l - H_m)^2 \tag{2.22}$$

where Q_l and H_l are defined in subregion F_l in the same way as Q_D and H_D are defined in the domain D.

We can also define the scale factor a_l for a subregion F_l. By definition, the different subregions are disjoint; therefore it follows that $|D|_g = \sum_l |F_l|_g$ and hence, using (Eq. 2.9), we have

$$a_D^3 = \sum_l \lambda_{l_i} a_l^3 \tag{2.23}$$

where $\lambda_{l_i} = \frac{|F_{l_i}|_g}{|D_i|_g}$ is the initial volume fraction, which can also be taken as the volume fraction at present and can be represented as λ_{l_0}, where the subscript 0 stands for quantities calculated at the present time. Differentiating this relation twice with respect to the foliation time results in,

$$\frac{\ddot{a}_D}{a_D} = \sum_l \lambda_l \frac{\ddot{a}_l(t)}{a_l(t)} + \sum_{l\neq m} \lambda_l \lambda_m (H_l - H_m)^2 \,. \tag{2.24}$$

As a direct result, it's evident that even when the subregions slow down, the second term in (Eq. 2.24) can balance the first term, resulting in global accelerated expansion.

So, now to calculate the scale factor for the global domain, a_D, the second-order differential equation (Eq. 2.24) needs to be solved. To solve this equation, expressions for λ_l, the volume fractions for subregions, $a_l(t)$, the scale factors for the subregions, and H_l, the Hubble parameter for the subregions, are required.

We need to formulate specific spacetime models with inhomogeneous matter distribution to use with the averaging procedure. These models will give us the required expressions to solve (Eq. 2.24). Our models in this thesis span from comparatively more straightforward two-subdomains to sophisticated multi-subdomains. The following chapters provide details of the various models with inhomogeneous matter distributions, along with the specific astrophysical and cosmological processes which have been analyzed using these models.

2.2 Covariant Scheme

Generally, cosmic backreaction is analyzed through the use of spatial averages. However, as frequently highlighted in the literature (see, for instance, [21, 60, 72–74]), one potential problem with this method is that most observations occur on the light cone. Thus, spatially averaged quantities (including the backreaction terms) become relevant only when they can be effectively connected to observables. After obtaining the averaged scalar quantities via Buchert's method, the goal is to associate these theoretically calculated quantities with observational quantities. There have been many attempts/schemes for relating spatial averages with observations. A distance-redshift relation in an inhomogeneous Universe was derived by Futamase and Sasaki by considering an approximate metric [20]. There is also the template scheme [75, 76]. The covariant scheme outlined in [33, 34] has been utilized in this thesis as it is a more advanced approach based on the procedure of averaging. The covariant scheme is given by a set of two equations -

$$1 + z = \frac{1}{a_{\mathcal{D}}} \,, \tag{2.25}$$

$$H_{\mathcal{D}} \frac{d}{dz}\Big((1+z)^2 H_{\mathcal{D}} \frac{dD_A}{dz}\Big) = -4\pi G \langle \rho_{\mathcal{D}} \rangle D_A \,. \tag{2.26}$$

(Eq. 2.26) describes the relationship between the average angular diameter

distance and the average redshift, based on the average rate of expansion. These averages are calculated over a hypersurface having a constant proper time. However, our actual observations of redshift and distance occur at just one specific location. Nevertheless, for practical purposes, the averages $\langle D_A \rangle$ and $\langle z \rangle$ do correspond to directly observable quantities. If the variations in D_A and z remain smaller compared to the observational errors, it is reasonable to assert that the averages correspond to the observed quantities.

The derivation of the covariant scheme requires spatial averages to be computed on hypersurfaces that display statistical homogeneity and isotropy. Importantly, it assumes that the evolution of structures occurs at a significantly slower pace than the time it takes for a light ray to traverse the homogeneity scale. Thus, any spacetime model with an inhomogeneous matter distribution applied in this thesis must adhere to these conditions. These assumptions allow for the description of distances using the average dust geometry. In this geometry, only the term for average expansion rate and the current matter density are needed. Notably, spatial curvature impacts solely through its influence on the expansion rate, unlike the case in FRW models with arbitrary matter content.

2.3 Gravitational Wave Amplitude

The existence of gravitational waves (GWs) was predicted by Albert Einstein in 1916 [77, 78] within the framework of linearized Einstein theory. Einstein field equations are given as,

$$R_{\mu\nu} - \frac{1}{2} R g_{\mu\nu} = \frac{8\pi G}{c^4} T_{\mu\nu}. \tag{2.27}$$

To begin understanding gravitational waves (GWs), we aim to examine how the Einstein equations expand when considering the flat-space metric. This involves assuming that the metric $g_{\mu\nu}$, which characterizes the gravitational field, is a Minkowski metric $\eta_{\mu\nu}$ with minor perturbations. Consequently, we express this as

$$g_{\mu\nu} = \eta_{\mu\nu} + h_{\mu\nu}, \qquad |h_{\mu\nu}| \ll 1, \tag{2.28}$$

and we expand the equations of motion to linear order in $h_{\mu\nu}$. The resulting theory is called *linearized theory.*

The linearized equations of motion are written more compactly, defining

$$h = \eta^{\mu\nu} h_{\mu\nu}, \tag{2.29}$$

and

$$\bar{h}_{\mu\nu} = h_{\mu\nu} - \frac{1}{2}\eta_{\mu\nu}h. \tag{2.30}$$

Making use of the gauge freedom, the linearized Einstein equations are given as,

$$\Box\bar{h}_{\mu\nu} = -\frac{16\pi G}{c^4}T_{\mu\nu} \tag{2.31}$$

where in the context of linearized theory, $\Box$ is defined as the flat space d'Alembertian, $\Box = \eta_{\mu\nu}\partial^\mu\partial^\nu = \partial_\mu\partial^\nu$.

2.3.1 The transverse-traceless gauge

Equation (Eq. 2.31) serves as a foundational result in the linearized theory for calculating the generation of gravitational waves (GWs). However, to examine their propagation and their interaction with test masses (such as in a GW detector), we focus on this equation in regions outside the source where $T_{\mu\nu} = 0$

$$\Box\bar{h}_{\mu\nu} = 0 \qquad \text{(outside the source)} \tag{2.32}$$

Since $\Box = -(1/c^2)\partial_0^2 + \nabla^2$, (Eq. 2.32) implies that the GWs travel at the speed of light. By making use of the residual gauge freedom, we can set [79]

$$h^{0\mu} = 0, \quad h^i_i = 0, \quad \partial^i h_{ij} = 0. \tag{2.33}$$

This defines the *tranverse-traceless gauge*, or TT gauge. This results in total degrees of freedom reducing to just two degrees of freedom. The metric in the TT gauge will be denoted by h^{TT}_{ij}.

(Eq. 2.32) has plane wave solutions, $h^{TT}_{ij} = e_{ij}(\mathbf{k})e^{ikx}$, with $k^\mu = (\omega/c, \mathbf{k})$ and $\omega/c = |\mathbf{k}|$ (and the usual convention that the real part is taken at the end of the computation). The tensor $e_{ij}(\mathbf{k})$ is called the polarization tensor. For a single plane wave with a given wave-vector $\mathbf{k}$ (or for a superposition of plane waves with different frequencies but all with the same direction of propagation $\hat{\mathbf{n}} = \mathbf{k}/|\mathbf{k}|$), we see from (Eq. 2.33) that the non-zero components of h^{TT}_{ij} are in the plane transverse to $\hat{\mathbf{n}}$ since, on a plane wave, the condition $\partial^j h_{ij} = 0$ becomes $n^i h_{ij} = 0$ [79]. Choosing for definiteness $\hat{\mathbf{n}}$ along the z axis, and imposing that h_{ij} be symmetric and traceless, we have [79]

$$h^{TT}_{ij}(t,z) = \begin{pmatrix} h_+ & h_\times & 0 \\ h_\times & -h_+ & 0 \\ 0 & 0 & 0 \end{pmatrix}_{ij} \cos\left[\omega(t - z/c)\right], \tag{2.34}$$

or, more simply,

$$h_{ab}^{TT}(t,z) = \begin{pmatrix} h_+ & h_\times \\ h_\times & -h_+ \end{pmatrix}_{ab} \cos\left[\omega(t - z/c)\right], \tag{2.35}$$

where $a, b = 1, 2$ are indices in the transverse (x, y) plane; h_+ and $h_\times$ are called the amplitudes of the "plus" and "cross" polarization of the wave [79].

2.3.2 Weak field sources and low-velocity expansion

Assuming the gravitational field from the GW source is sufficiently weak, we can justifiably expand around a flat spacetime. A weak gravitational field implies that $v \ll c$, meaning that in self-gravitating systems, weak fields correspond to low velocities. The radiation generation equations simplify significantly if the source's typical velocities are much lower than the speed of light. Given that ω_s characterizes the frequency of motion within the source and d is its size, typical source velocities can be expressed as $v \sim \omega_s d$. Consequently, the radiation frequency ω will be of the same order as ω_s, leading to $\omega \sim \omega_s \sim v/d$ [79]. In terms of $\lambda\!\!\!^{-} = c/\omega$,

$$\lambda\!\!\!^{-} \sim \frac{c}{v} d. \tag{2.36}$$

In a non-relativistic system, $v \ll c$ and the reduced wavelength of the radiation generated is much bigger than the size of the system:

$$\text{non-relativistic sources} \implies \lambda\!\!\!^{-} \gg d.$$

In cases where the reduced wavelength significantly exceeds the size of the system, it is evident that understanding the detailed internal motions of the source is unnecessary; only the key features are significant. Consequently, radiation emission is dominated by the lowest multipole moments. The objective here is, thus, to carry out a multipole expansion for gravitational radiation [79].

Using retarded Green's function and tensor algebra, expression of h_{ij}^{TT} at spatial infinity can be written as [79]

$$h_{ij}^{TT}(t,x) = \frac{1}{r}\frac{4G}{c^4}\Lambda_{ij,kl}(\hat{\mathbf{n}}) \int d^3x' T_{kl}\left(t - \frac{r}{c} + \frac{\mathbf{x}'.\hat{\mathbf{n}}}{c}, \mathbf{x}'\right) \tag{2.37}$$

We define the momenta of T^{00}/c^2 by

$$M = \frac{1}{c^2}\int d^3x T^{00}(t,x), \tag{2.38}$$

$$M^i = \frac{1}{c^2}\int d^3x T^{00}(t,x)x^i, \tag{2.39}$$

$$M^{ij} = \frac{1}{c^2}\int d^3x T^{00}(t,x)x^i x^j, \tag{2.40}$$

$$M^{ijk} = \frac{1}{c^2}\int d^3x T^{00}(t,x)x^i x^j x^k, \tag{2.41}$$

and so on. Fourier transforming T_{kl} of (Eq. 2.37) and using equations (Eq. 2.38 - Eq. 2.41), the leading term of the expansion (Eq. 2.37) is [79]

$$\left[h_{ij}^{TT}(t,x)\right]_{quad} = \frac{1}{r}\frac{2G}{c^4}\Lambda_{ij,kl}(\hat{\mathbf{n}})\ddot{M}^{kl}(t-r/c). \tag{2.42}$$

2.3.3 Mass quadrupole radiation

Here, we use the notation

$$\rho = \frac{1}{c^2}T^{00} \tag{2.43}$$

To lowest order in v/c, ρ becomes the mass density. We also introduce the quadrupole moment

$$Q_{ij} \equiv M^{ij} - \frac{1}{3}\delta^{ij}M_{kk} = \int d^3x\rho(t,\mathbf{x})(x^i x^j - \frac{1}{3}r^2\delta^{ij}) \tag{2.44}$$

and (Eq. 2.42) becomes [79]

$$\left[h_{ij}^{TT}(t,x)\right]_{quad} = \frac{1}{r}\frac{2G}{c^4}\Lambda_{ij,kl}(\hat{\mathbf{n}})\ddot{Q}_{kl}(t-r/c) \tag{2.45}$$

$$\equiv \frac{1}{r}\frac{2G}{c^4}\ddot{Q}_{ij}^{TT}(t-r/c). \tag{2.46}$$

It can be shown that for a GW in a frame with axes (x,y,z), propagating in a generic direction $\hat{\mathbf{n}}$, h_+ and $h_\times$ are given by [79],

$$\begin{aligned} h_+(t;\theta,\phi) = \frac{1}{r}\frac{G}{c^4}[&\ddot{M}_{11}(\cos^2\phi - \sin^2\phi\cos^2\theta) + \ddot{M}_{22}(\sin^2\phi - \cos^2\phi\cos^2\theta) \\ &- \ddot{M}_{33}\sin^2\theta - \ddot{M}_{12}\sin 2\phi(1+\cos^2\theta) \\ &+ \ddot{M}_{13}\sin\phi\sin 2\theta + \ddot{M}_{23}\cos\phi\sin 2\theta] \\ h_\times(t;\theta,\phi) = \frac{1}{r}\frac{G}{c^4}[&(\ddot{M}_{11} - \ddot{M}_{22})\sin 2\phi\cos\theta + 2\ddot{M}_{12}\cos 2\phi\cos\theta \\ &- 2\ddot{M}_{13}\cos\phi\sin\theta + 2\ddot{M}_{23}\sin\phi\sin\theta] \end{aligned} \tag{2.47}$$

This equation allows us to compute the angular distribution of the quadrupole radiation, once M_{ij} is given.

2.3.4 Quadrupole radiation from a mass in circular orbit

Here, we examine a binary system consisting of masses m_1 and m_2, assuming the relative coordinate undergoes circular motion. For now, we presuppose the characteristics of the orbital motion are defined.

So, for the moment, we rather assign ourselves the trajectory. We choose the (x, y, z) frame so that the orbit lies in the (x, y) plane, and is given by

$$\begin{aligned} x_0(t) &= R\cos(\omega_s t + \frac{\pi}{2}), \\ y_0(t) &= R\sin(\omega_s t + \frac{\pi}{2}), \\ z_0(t) &= 0. \end{aligned} \tag{2.48}$$

We denote by $\mu = m_1 m_2/(m_1 + m_2)$ the reduced mass of the system. In the center-of-mass (CM) frame, the second mass moment is $M^{ij} = \mu x_0^i(t) x_0^j(t)$, so

$$M_{11} = \mu R^2 \tfrac{1-\cos 2\omega_s t}{2}, \tag{2.49}$$

$$M_{22} = \mu R^2 \tfrac{1+\cos 2\omega_s t}{2}, \tag{2.50}$$

$$M_{12} = -\tfrac{1}{2}\mu R^2 \sin 2\omega_s t, \tag{2.51}$$

while the other components vanish. Therefore, we have

$$\ddot{M}_{11} = 2\mu R^2 \omega_s^2 \cos 2\omega_s t, \tag{2.52}$$

$$\ddot{M}_{12} = 2\mu R^2 \omega_s^2 \sin 2\omega_s t, \tag{2.53}$$

and $\ddot{M}_{22} = \ddot{M}_{11}$. Plugging these expressions into (Eq. 2.47), we get [79]

$$h_+(t;\theta,\phi) = \tfrac{1}{r}\tfrac{4G\mu\omega_s^2 R^2}{c^4}\left(\tfrac{1+\cos^2\theta}{2}\right)\cos(2\omega_s t_{ret} + 2\phi) \tag{2.54}$$

$$h_\times(t;\theta,\phi) = \tfrac{1}{r}\tfrac{4G\mu\omega_s^2 R^2}{c^4}\cos\theta\sin(2\omega_s t_{ret} + 2\phi) \tag{2.55}$$

2.3.5 Inspiral of compact binaries

We now examine a binary system comprised of two compact objects, such as neutron stars or black holes, considering them as point masses with masses m_1, m_2 and positions $\mathbf{r}_1$ and $\mathbf{r}_2$. Under the Newtonian approximation and in the center-of-mass (CM) frame, this setup simplifies to a single-body problem characterized

by a mass equal to the reduced mass $\mu = m_1 m_2/(m_1 + m_2)$. The equation of motion is given by $\ddot{\mathbf{r}} = -(Gm/r^3)\mathbf{r}$, where $m = m_1 + m_2$ is the combined mass and $\mathbf{r} = \mathbf{r}_2 - \mathbf{r}_1$ represents the relative coordinate. Focusing on circular orbits, the orbital frequency ω_s and the orbital radius R are connected through the condition $v^2/R = Gm/R^2$, where $v = \omega_s R$, so we have Kepler's law,

$$\omega_s^2 = \frac{Gm}{R^3}. \tag{2.56}$$

The corresponding GW amplitude for such a system is given in (Eq. 2.54) and (Eq. 2.55). In these expressions, we eliminate R in favour of ω_s using (Eq. 2.56), and we introduce the *chirp mass*

$$M_c = \mu^{3/5} m^{2/5} = \frac{(m_1 m_2)^{3/5}}{(m_1 + m_2)^{1/5}}. \tag{2.57}$$

Then, (Eq. 2.54) and (Eq. 2.55) become [79]

$$\begin{aligned} h_+(t) &= \frac{4}{r}\left(\frac{GM_c}{c^2}\right)^{5/3}\left(\frac{\omega_s}{c}\right)^{2/3}\frac{1+\cos^2\theta}{2}\cos(2\omega_s t_{ret} + 2\phi) \\ h_\times(t) &= \frac{4}{r}\left(\frac{GM_c}{c^2}\right)^{5/3}\left(\frac{\omega_s}{c}\right)^{2/3}\cos\theta\sin(2\omega_s t_{ret} + 2\phi), \end{aligned} \tag{2.58}$$

Here, ω_s is the orbital frequency at the point of emission. The observed frequency will be redshifted by an amount $\omega_o = \omega_s/(1+z)$, where z is the redshift at the point of emission. Also, r here is the comoving distance; it is related to the luminosity distance, D_L, by the relation $D_L = (1+z)r$. Therefore, (Eq. 2.58) becomes,

$$\begin{aligned} h_+(t) &= \frac{4(1+z)^{5/3}}{D_L}\left(\frac{GM_c}{c^2}\right)^{5/3}\left(\frac{\omega_o}{c}\right)^{2/3}\frac{1+\cos^2\theta}{2}\cos(2\omega_s t_{ret} + 2\phi) \\ h_\times(t) &= \frac{4(1+z)^{5/3}}{D_L}\left(\frac{GM_c}{c^2}\right)^{5/3}\left(\frac{\omega_o}{c}\right)^{2/3}\cos\theta\sin(2\omega_s t_{ret} + 2\phi), \end{aligned} \tag{2.59}$$

The quantity of interest for our analysis in (Chap. 3) and (Chap. 4) is the redshift-dependent part of the GW amplitude in (Eq. 2.59) given by,

$$\frac{(1+z)^{5/3}}{D_L}$$

2.4 Observational Dataset

The models of spacetime with inhomogeneous matter distributions that we have employed for various analyses in this thesis have some parameters. We would like to constrain these model parameters using observational data. Covariant

scheme (Sec. 2.2) allows us to calculate cosmological distances from theoretically calculated quantities from our models. Therefore, observational datasets of cosmological distances are ideal for our analysis.

In principle, cosmic distances can be readily determined by using any identifiable class of astronomical objects with a known intrinsic brightness as a "standard candle." By comparing the object's apparent brightness to that of a nearby object of the same class, its distance from Earth can be calculated.

Starting in 1938, Walter Baade, in collaboration with Fritz Zwicky, identified supernovae as highly potential standard candles. Their maximum luminosity appeared relatively consistent, and they were sufficiently luminous to be observable from great distances [80, 81]. In fact, for several weeks, a supernova can shine as brightly as a whole galaxy. Nevertheless, as the number of observed supernovae grew over the years, it was increasingly evident that they constituted a diverse group with a significant variability in intrinsic peak brightness.

During the early 1980s, a new method for categorizing supernovae was developed. Previously, supernovae without hydrogen lines in their spectra had all been grouped under type I. However, this category was further divided into types Ia and Ib based on whether a silicon absorption line was present or absent at $6150\,\text{Å}$ in the supernova's spectrum [82, 83]. This refinement in classification revealed a remarkable uniformity among type Ia supernovae. Not only did their spectra align feature by feature, but their light curves- graphs showing changes in brightness over the weeks after a supernova explosion- also corresponded closely [84–87].

In astronomy, the brightness of a celestial object is quantified in terms of its magnitude. The magnitude scale is essentially a logarithmic scale. There are two primary types of magnitudes - apparent and absolute magnitude. The apparent magnitude depends on observed energy fluxes, and the absolute magnitude represents the intrinsic luminosity of the object. The relation between absolute magnitude, apparent magnitude, and distance modulus is given by,

$$m = M + 5\log_{10}(d_L/10\text{ pc}), \tag{2.60}$$

where m is the apparent magnitude of the celestial object at a luminosity distance d_L and M is the absolute magnitude of the object. The quantity $5\log_{10}(d_L/10\text{ pc})$, which is equal to $(m - M)$, is called the distance modulus of the object. Here, 10 pc is the chosen standard distance of 10 parsecs.

SNe Ia serve as an excellent "standard candle" because they precisely determine the magnitude-redshift relationship across a broad spectrum of redshifts, from $z = 0$ up to $z \sim 1.5$, and potentially beyond this range.

The study in [88] developed an organized strategy for integrating the extensive collections of SNe Ia datasets into a cohesive set known as the "Union" compi-

lation. The principles underpinning the Union analysis offer several advantages. It treats all SN Ia datasets equally, with the same light-curve fitting, cuts, and outlier rejections. Systematic error estimates are incorporated into a covariance matrix, which is applicable for fitting any cosmological model. The decisions on analysis execution and specific cuts to implement are determined with the cosmological results hidden, following a"blind" approach, which helps reduce potential biases from over-examining some datasets more than others. This methodology was applied by the authors in [89] to formulate the Union2 compilation. The paper also made several significant revisions and enhancements to the Union analysis. Union2 was later updated to Union2.1, with the primary modification being an adjustment to the host-mass-SN Ia-luminosity relation. Additionally, the HST calibration and its related errors were also updated.

We have used Union2.1 Type Ia supernova distance modulus vs redshift data to constrain our model parameters in (Chap. 5) and (Chap. 6).

2.5 Markov Chain Monte Carlo Analysis

In this thesis, we have constrained the parameters of our theoretical models of spacetime with inhomogeneous matter distribution using Union2.1 Type Ia supernova redshift versus distance modulus observational data by performing the Markov Chain Monte Carlo (MCMC) analysis in (Chap. 5) and (Chap. 6).

MCMC is a computer-driven sampling technique [90]. It enables the analysis of a distribution without a complete understanding of its mathematical details by randomly extracting values from it. A notable advantage of MCMC is its capability to generate samples from distributions by relying solely on the method for calculating their densities. The term MCMC stands for two features: Monte-Carlo and Markov chain. Monte-Carlo refers to the method of estimating distribution properties by analyzing random samples. For instance, instead of computing the mean of a normal distribution using its formulae, one could apply a Monte–Carlo approach by drawing numerous random samples from the normal distribution and determining their mean. This approach is particularly advantageous because calculating the mean from a large number of samples can be simpler than computing it directly from the distribution's equations, especially when it is straightforward to draw random samples but difficult to work with the distribution's equations otherwise. The Markov chain aspect of MCMC involves generating random samples through a specific sequential process. Each sample acts as a foundation for creating the subsequent sample, forming a chain. A key characteristic of this chain is its adherence to the Markov property, where each new sample depends solely on its immediate predecessor, without influence from earlier samples (this is the "Markov" property).

MCMC is particularly useful in Bayesian inference because it focuses on posterior distributions, which are often difficult to address using analytical approaches. In these scenarios, MCMC facilitates the estimation of various aspects of posterior distributions that cannot be directly calculated, such as drawing random samples or evaluating posterior means. Bayesian inference applies data obtained from observations, referred to as the likelihood, to update prior beliefs about one or more parameters into a posterior state of beliefs about these parameters. Formally, Bayes' rule is defined as

$$p(\mu|D) \propto p(D|\mu) \cdot p(\mu) \tag{2.61}$$

where μ represents the parameter(s) we are examining and D represents the dataset. The term $p(\mu|D)$ denotes the posterior, reflecting the probability of μ given D. The likelihood, $p(D|\mu)$, expresses the probability of the data when considering μ, while $p(\mu)$ stands for the prior, which is the initial probability of μ. The symbol $\propto$ signifies "is proportional to".

The main focus of this discussion is that updating previous beliefs with new information necessitates evaluating how likely the data is for particular values of parameters of interest. Ideally, this evaluation would cover all possible combinations of parameter values. If an analytical expression for this likelihood exists, it can be combined with the prior analytically to derive the posterior. However, such expressions are frequently not available. In Bayesian inference, this challenge is often addressed through MCMC methods, which involve drawing a series of samples from the posterior to analyze their mean, range, and other characteristics.

MCMC initiates with an initial guess, representing a potential value from the distribution. The method utilizes this point to produce a sequence of new samples. Generating each new sample involves two simple steps: initially, a proposal is created by adding a slight random perturbation to the latest sample; subsequently, this proposal is either accepted as the new sample or rejected, in which case the previous sample is kept. There are numerous techniques for making proposals with random noise, as well as for devising acceptance and rejection methods. Among the various MCMC sampling strategies, the Metropolis algorithm stands out for its popularity. In this approach, a new proposal is crafted by modifying the previous sample with random noise, sourced from a proposal distribution that should be symmetric and zero-centered. The validity of the proposal in relation to the target distribution is assessed by comparing the posterior at the proposal to that at the current sample. If the proposal's posterior is higher, it is accepted. If lower, it is accepted at a probability proportional to the ratio of their posterior values. For example, with a proposal's posterior at one-fifth of the current sample, it has a 20% chance of being accepted. If accepted, the proposal becomes the

next sample in the MCMC chain; otherwise, the chain continues with the prior sample. This concludes one MCMC cycle, which is followed by creating a new proposal from the latest sample with added random noise. The sampling process terminates once a sufficient number of samples has been gathered.

This MCMC algorithm is a reliable method for drawing samples from a distribution, particularly when the calculation of its likelihood function is the sole known aspect. The effectiveness of the technique lies in its ability to ensure that the sampling distribution matches the target distribution under certain conditions. First, the proposal acceptance or rejection must be based on likelihoods that accurately reflect the proposal's density within the target distribution. In Bayesian inference, this translates to the requirement that calculated values are posterior likelihoods or proportional thereto—that is, the ratio between likelihoods must be accurate. Second, the proposal distribution should ideally be symmetric; if not, and in the case of asymmetry, the 'Metropolis-Hastings' algorithm, with an altered acceptance/rejection criterion, should be utilized. Lastly, due to the potential inaccuracy of initial estimates, the Markov chain's first phase should be discarded since these initial samples may not be representative of the target distribution.

The effectiveness of the sampler is significantly affected by the selection of the proposal distribution. A large standard deviation in the proposal distribution may result in numerous proposals falling outside the target distribution, causing a high rejection rate. Conversely, a very small standard deviation might require many iterations for the sampler to reach the target distribution from the initial value. Additionally, there is a risk of becoming trapped in local maxima, where a particular value has a higher likelihood compared to its nearby values, yet possesses a lower likelihood relative to values that are more distant.

The proposal distribution's width is often referred to as a tuning parameter within the Metropolis algorithm. The practical efficiency of the sampler can be influenced by the tuning parameter's value, which is a notable shortcoming of the standard Metropolis–Hastings sampling algorithm. However, there are numerous enhanced techniques available to address this issue.

The third condition underscores the necessity of eliminating initial samples to rectify inaccuracies related to convergence and burn-in. To address this, one can choose starting points closer to the posterior distribution's mode, promoting a faster burn-in and mitigating convergence difficulties. Although finding such starting points can be tricky, techniques like maximum-likelihood estimation can help identify suitable options. Alternatively, running multiple chains by sampling several times with different initial values (possibly from the prior distribution) can be effective. Any variation in sample distributions across chains might indicate burn-in and convergence issues. A practical tactic is to remove early samples

from the chain's non-stationary segments. Essentially, samples collected before achieving convergence fail to represent the intended distribution and should be disregarded.

For our analysis in (Chap. 5) and (Chap. 6), we have used the `MCMCSTAT` package [91, 92]. We have employed the Metropolis-Hastings algorithm for our analysis. We have taken Gaussian distributions as prior distributions for our model parameters. This toolkit offers capabilities for creating and examining Metropolis-Hastings MCMC chains utilizing a multivariate Gaussian proposal distribution. More information about the analysis is provided in the relevant sections of (Chap. 5) and (Chap. 6).

Chapter 3

Effect of inhomogeneities on the propagation of gravitational waves from binaries of compact objects

3.1 Introduction

Gravitational waves (GWs) have been an integral part of Einstein's General Relativity since 1916 [77, 78]. These waves represent ripples in spacetime, caused by any mass (or energy) in motion such that the concerned second mass-moment (or quadrupole moment in the transverse-traceless gauge) exhibits a non-zero second-order time derivative. The field of GW has recently gained attention due to multiple detections of gravitational waves originating from compact binary mergers, first announced by LIGO and VIRGO collaborations [93–97]. The parameters measured from these gravitational waves provide crucial insights into the properties of their sources, including their mass range and merger rates. In gravitational wave data analysis, it is typically assumed that the waves traverse a homogeneous and isotropic FLRW-Universe from the source to the detector.

As discussed in (Chap. 1), observations have shown significant inhomogeneities in matter distribution. These inhomogeneities due to structures may have important effects on length scales even as large as 500 h^{-1} Mpc [9]. The present observations of gravitational waves [93–97] pertain to sources which lie well within the scale at which there exists overall homogeneity in the Universe. Hence, examining the impact of these inhomogeneities on the propagation of gravitational waves could be crucial for precise measurements in the emerging field of gravitational wave astronomy.

Consideration of the effect of local inhomogeneities leads to certain interesting

effects on the propagation of electromagnetic waves in the averaged Universe. Studies investigating the motion of photons in an averaged geometry have been performed [33, 34, 64], with some employing a gauge-invariant approach for averaging on the past null cone [21, 59, 60]. Furthermore, light propagation in inhomogeneous Swiss-Cheese models has been examined by simulating the Hubble diagram [65–67]. An averaged form of the null geodesic equation has been developed [58], revealing that the light propagation equation incorporates an effective Hubble parameter for averaged spacetime, distinct from the homogeneous version. This leads to modified cosmological-distance versus redshift relations when averaging over inhomogeneities [49, 51, 98]. These modifications suggest interesting possibilities for detecting inhomogeneity signals using cosmic expansion rate probes [42, 50].

Gravitational waves act as complementary messengers to electromagnetic waves, opening up a new window to the physics of the Universe and have led to the emergence of the field of multi-messenger astronomy. Both electromagnetic and gravitational waves can be used together to study the expansion history of the Universe, which is essential for the understanding of current cosmic acceleration and the nature of gravity itself. Moreover, gravitational waves hold particular importance for sources that do not produce electromagnetic signals. The scientific discoveries arising from gravitational wave detection are vital for advancing our knowledge across multiple fields, including physics, astrophysics, and cosmology. In this study, our aim is to examine how local inhomogeneities within the Universe affect the propagation of gravitational waves.

As discussed in (Chap. 1) and (Chap. 2), in order to investigate the effects of local inhomogeneities on the dynamics at larger scales, an averaging procedure is necessary. In this thesis, we have employed Buchert's averaging procedure [25, 26]. In the context of Buchert's averaging procedure, here in this analysis, we employ a simplistic model of a two-partitioned Universe *viz.*, all inhomogeneities are clubbed into overdense (wall) and underdense (void) regions. Our motivation is to investigate the change in observed amplitude of the gravitational wave signal due to averaging over various combinations of the fractions of these two types of partitions in comparison to the case where the gravitational wave is assumed to traverse through a completely homogeneous and isotropic spacetime described by the ΛCDM model. In the above framework, we consider gravitational waves from binaries of compact objects like black holes and neutron stars in their early inspiral stage. Our analysis demonstrates that there could be a significant deviation in the gravitational wave amplitude as a result of backreaction due to inhomogeneities present in the intervening spacetime between the source and detector.

This chapter is organized as follows. A brief description of our two-partitioned model and ansatz in the context of Buchert's backreaction formalism is presented

in (Sec. 3.2). In (Sec. 3.3), the modification of the redshift-distance relation due to the averaging procedure is presented. The modification of the redshift dependent part of gravitational wave amplitude from a binary of compact objects in our model is analyzed and compared to the case in the ΛCDM model in (Sec. 3.4). Finally, we present some concluding remarks in (Sec. 3.5).

3.2 A model of backreaction in Buchert's formalism

Using Buchert's averaging procedure, as discussed in (Chap. 2), the average of scalar quantities over a mass-preserving domain $\boldsymbol{D}$ can be calculated (Eq. 2.10).

In the context of the framework employed in this thesis (Subsec. 2.1.1), we consider a simplified scenario where the domain $\boldsymbol{D}$, which contains the path traversed by the gravitational wave from the source to observer, can be broadly classified into two types of regions or sub-domains [17, 35]: (i) the overdense region or 'Wall' and (ii) the underdense region or 'Void'. Note that in the present work, we will not consider any possible attenuation of the gravitational wave amplitude due to shear effects.

We aim to investigate the difference in the observed amplitude of gravitational waves in the two different cases, *viz.* (a) when the gravitational wave is assumed to propagate through a homogeneous and isotropic spacetime, described by the FLRW metric in the ΛCDM model, and (b) when the gravitational wave propagates through an inhomogeneous spacetime, described by our model within the Buchert framework. The luminosity distance of compact binaries from which gravitational waves have been detected has a massive variation from the order of 50 Mpc to 5000 Mpc [99, 100]. The length scales of the cosmic voids, which are vast spaces between large-scale structures in the Universe containing no or a negligible number of galaxies, are typically 10 to 100 Mpc [101]. So, it is pretty clear that for the typical sources responsible for the detection of gravitational wave events by aLIGO and VIRGO, the gravitational waves might have to traverse through one or more of these voids while reaching the Earth. Hence, the physical interpretation of our model is that all the cosmic voids in the path of propagation of the gravitational wave constitute the underdense region, and the rest of the regions rich in galaxies and other stellar matter constitute the overdense region.

Then, according to the definitions of average quantities as given in the equations (Eq. 2.9) and (Eq. 2.10), the average volume scale-factor a_D and the average Hubble parameter for our two-partitioned model are given by respectively :

$$a_D = \Big(\frac{a_u^3 + a_o^3}{a_{u,0}^3 + a_{o,0}^3}\Big)^{1/3}, \tag{3.1}$$

and,

$$H_D = H_u \frac{a_u^3}{a_u^3 + a_o^3} + H_o \frac{a_o^3}{a_u^3 + a_o^3}\,, \tag{3.2}$$

where the a_u and a_o denote the volume scale-factors of the underdense region and overdense region, respectively. The suffix '0' stands for the present time, *i.e.*, $a_{u,0}$ and $a_{o,0}$ denote the present values of these scale-factors. H_u and H_o denote, respectively, the Hubble parameters of the underdense and overdense regions. (Eq. 3.1) shows the particular scaling of scale factors we have used for this analysis.

In our model, we consider that the overdense region or 'Wall' is described by a closed and dust-only FLRW-region and the underdense region or 'Void' is an empty (or, having negligible matter-density) FLRW-region. The backreaction term $\mathcal{Q}_D$ for our 2-domain model is given by [27],

$$\mathcal{Q}_D = f_o \mathcal{Q}_o + (1 - f_o)\mathcal{Q}_u + 6 f_o (1 - f_o)(H_o - H_u)^2, \tag{3.3}$$

where f_o denotes the volume fraction of the overdense region. For our model, we have taken the sub-domains to be described by FLRW-regions to neglect back-reaction on the sub-domains for simplification, i.e., $\mathcal{Q}_o = 0$ and $\mathcal{Q}_u = 0$. This stipulation to FLRW is an approximate assumption governing our toy model (in the more general case the sub-domains may not necessarily be FLRW-regions). From (Eq. 3.3), it can be seen that control over global backreaction can be achieved only if the individual backreaction terms are not set to zero.

The time-evolution of the scale-factors a_u and a_o, of the underdense region and overdense region in our model, can be described parametrically in terms of a development-angle ϕ. We choose the following ansatz which is a generalization of earlier formulations [35, 36, 46]:

$$t = t_0 \Big(\frac{\phi - \sin\phi}{\phi_0 - \sin\phi_0} \Big), \tag{3.4}$$

$$a_o = \frac{f_o^{1/3}}{2}(1 - \cos\phi)\,, \tag{3.5}$$

$$a_u = \frac{f_u^{1/3}(\phi_0 - \sin\phi_0)}{\pi t_0} t^\beta\,. \tag{3.6}$$

In the above set of equations (Eq. 3.4) - (Eq. 3.6), f_u and $f_o = 1 - f_u$ are the fractions of volume of the underdense region and overdense region respectively at $\phi = \pi$. ϕ_0 is the development-angle parameter at the present time and $\phi_0 = 3\pi/2$ [35]. We set the present age of the Universe $t_0 \approx 13.8\,Gy$. a_u can be expressed in terms of ϕ, by substituting the expression of the time t from (Eq. 3.4) on the RHS of (Eq. 3.6). Here, the parameter β is chosen between 2/3 to 1, to denote any behaviour ranging from a matter-dominated region, *viz.*, $\beta = 2/3$, up to a

dark energy dominated region *viz.*, $\beta > 1$.

3.3 Modification of redshift and distance calculation in the backreaction framework

As Buchert's backreaction formalism is based on spatially averaged quantities over the concerned domain, it is necessary to relate these spatially averaged quantities to observables in cosmology. As discussed in (Sec. 2.2), we have utilized the covariant scheme for this purpose (Eq. 2.25 and Eq. 2.26).

The covariant scheme can be applied provided that the spatial averages are calculated on the hypersurfaces of statistical homogeneity and isotropy, and the evolution of structure in the Universe is sufficiently slow in the time interval of propagation of the wave from source to observer. It has been shown [35, 37] that for a model like ours, the covariant scheme is suitable for describing the relation between the effective redshift and cosmological angular diameter distance.

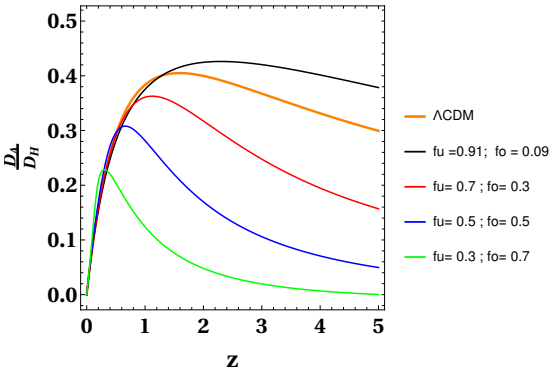

Figure 3.1: Plot of the ratio of angular diameter distance D_A to the present Hubble length-scale D_H w.r.t. redshift, for the ΛCDM case with different combinations of the fractions f_u and f_o for $\beta = 1$.

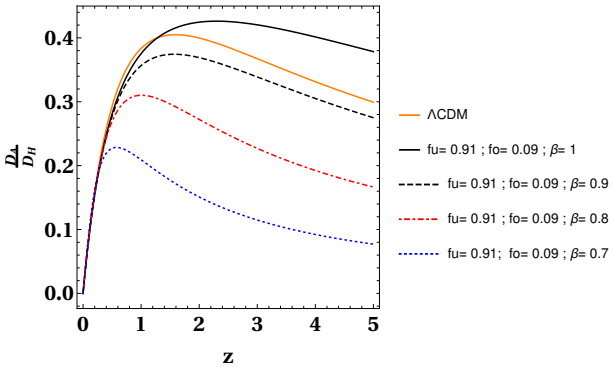

Figure 3.2: Plot of the ratio of angular diameter distance D_A to the present Hubble length-scale D_H w.r.t. redshift, for the ΛCDM case with different values of the parameter β, with the combination of the fractions $f_u = 0.91$ and $f_o = 0.09$.

In the present context, the domain D on which we take the averages encompasses the path of propagation of the gravitational wave from the source to the observer, and could arise from an arbitrary combination of the fractions f_u and f_o. We study the redshift-distance relation for different combinations of these fractions. In (Fig. 3.1) we plot the ratio of the angular diameter distance D_A, given by equation (Eq. 2.26), to the present Hubble-length scale ($D_H = cH_0^{-1}$) with the redshift for five different combinations of the fractions fu and fo in our model along with the plot of D_A/D_H for the ΛCDM model.

It can be seen from (Fig. 3.1) that up to redshift of around 1, almost all the curves are very close to that of the ΛCDM case, while after a certain redshift,

each of these curves starts deviating from the ΛCDM curve. It can be ascertained that for a certain combination of f_u and f_o, this redshift-distance relation almost coincides with that of the ΛCDM case. By numerical calculations using *Mathematica*, we find that for the combination $f_u = 0.845$ and $f_o = 0.155$, with $\beta = 1$, the variation of the quantity D_A/D_H is almost identical to that of the ΛCDM model. As expected, departure from the ΛCDM model increases for greater inhomogeneity, denoted by larger variation from the value of volume fractions $(f_u, f_o) = (0.845, 0.155)$.

Next, in (Fig. 3.2) we plot the ratio of angular diameter distance D_A to the present Hubble length-scale D_H w.r.t. redshift by varying the parameter β for the combination of fractions $f_u = 0.91$ and $f_o = 0.09$. We chose this value of combination (f_u, f_o) as this is the combination that has been indicated by N-body simulations of structure formations for a two-partitioned Universe at the present time [27]. It is seen that conformity with the homogeneous (ΛCDM) model can be achieved for intermediate values of the void expansion parameter $\beta(\sim 0.92)$, whereas, the limiting cases of matter domination ($\beta \sim 0.7$) and dark energy ($\beta \sim 1$) lead to greater deviation from the ΛCDM case.

The change in the observed redshift of a comoving source in the time interval of its observation is known as the redshift-drift. It can be given by $\delta z = \left[\frac{dz}{dt}\right]_{t=t_0} \delta t_0$, where $[dz/dt]_{t=t_0}$ is the time-rate of change of redshift and the suffix $t = t_0$ indicates its value at the observation time which has been taken as the present time t_0. As the time scale of observation is generally much lesser than the time scale of cosmological evolution, the expression of the redshift-drift δz can be further simplified by applying the Taylor-series expansion, followed by neglecting the higher-order terms, as given below [35]:

$$\delta z = \delta t_0 \{(1+z)H_0 - H_e\} = \delta t_0 (1+z) \left\{ \left[\frac{\partial a}{\partial t}\right]_{t_0} - \left[\frac{\partial a}{\partial t}\right]_{t_e} \right\}, \tag{3.7}$$

where H_0 is the Hubble parameter at the time of observation, which has been taken as the present time, and H_e is the Hubble parameter at the time of emission of the signal.

The redshift-drift has been discussed in several works [35, 36, 42, 49, 102]. The analysis appears to be the same for the electromagnetic wave and gravitational wave sources, and the redshift-drift is directly proportional to the observation time δt_0. However, the redshift drift is minimal for gravitational wave sources; specifically, the binaries of compact objects, *viz.*, black holes and neutron stars, which have been observed by aLIGO or VIRGO (δt_0 is of the order of fractions of seconds to few minutes). Hence, the magnitude of the redshift-drift would be of very low order in these cases. However, for binaries of supermassive black holes, from which the gravitational wave signal is expected to be detectable by

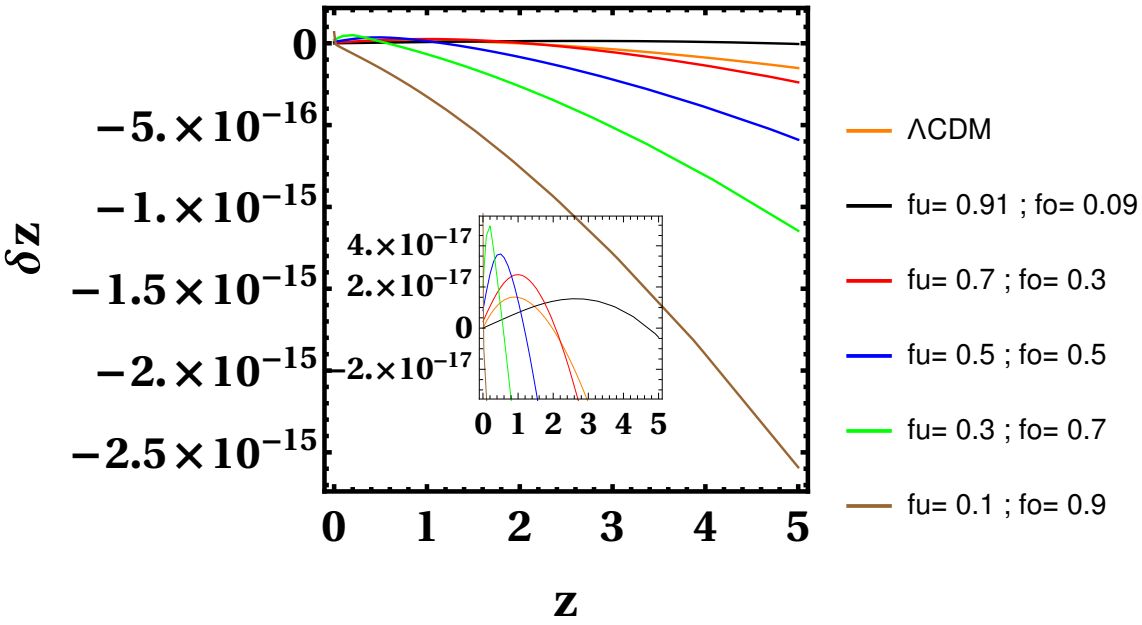

Figure 3.3: Plot of drift of averaged redshift δz w.r.t. the redshift z, for the ΛCDM model and for our model with different combinations of fu and fo with $\beta = 1$. The magnified region of the curves, for range of δz between 5×10^{-17} to -3×10^{-17} is shown in inset in order to ascertain the transition of δz from positive to negative value.

the future gravitational wave detectors like LISA, the time of observation δt_0 can be of much higher order and hence, the redshift-drift's magnitude should increase significantly for these type of binaries, especially at higher redshifts.

The sign of the redshift-drift indicates whether the Universe is accelerating or decelerating in the time interval of emission and observation of the signal, while its magnitude indicates the extent of the acceleration or deceleration. The expression of redshift-drift given in the (Eq. 3.7) implies that for an accelerating Universe between the emission and observation times, the redshift-drift is positive. For a decelerating Universe between those times, it is negative. For the ΛCDM model, we get acceleration from a certain time in the late Universe, from which Λ starts dominating over the matter till the present. So, for the ΛCDM model, we can get a positive redshift-drift only after a certain redshift. For an inhomogeneous Universe described by Buchert's backreaction formalism, the drift of the averaged redshift can be effectively described by replacing the Hubble parameters' values with the averaged Hubble parameters [35]. However, as pointed out in Ref. [35], the exact calculation of redshift-drift is obtained through a more elaborate process, and the drift of the averaged redshift may not represent the exact redshift-drift correctly.

The main motivation of our present analysis is to study the effect of inhomogeneities on parameters of gravitational wave sources, as discussed in detail in the next section. For the present, we will provide a calculation of the drift of the averaged redshift. This is to reemphasize the role of inhomogeneities on the prop-

agation of various signals (electromagnetic and gravitational) in the Universe, as computed through the backreaction formalism. In (Fig. 3.3), we plot the drift of the averaged redshift with respect to the redshift for the ΛCDM model and our model with different combinations of the volume fractions f_u and f_o. By numerical calculations using *Mathematica*, we find that for the combination $f_u = 0.768$ and $f_o = 0.232$, with $\beta = 1$, variation of the drift of averaged redshift is almost identical to that of the ΛCDM model. [1]

It may be noted from (Fig. 3.3) that the drifts of the averaged redshift are positive only up to a certain redshift for all the curves. The redshift at which the value of the drift of averaged redshift transits from positive to negative is different for each curve. This redshift of transition gradually decreases with an increase in f_o or a decrease in f_u.

3.4 Change in gravitational wave observables in the backreaction framework

The gravitational wave amplitude from a binary of compact objects of masses m_1 and m_2, in the early inspiral stage where Keplerian approximations are well valid, is given by (for cross(×)-polarization) [79]

$$h_\times = \frac{G^{5/3}(1+z)^{5/3}}{D_L c^4} \frac{m_1 m_2}{(m_1+m_2)^{1/3}} (-4\omega^{2/3}) \sin 2\omega t\,, \tag{3.8}$$

where ω is the observed angular frequency of the binary of compact objects and D_L is the luminosity distance of the binary from the observer. For the plus(+)-polarization, the peak of the amplitude remains identical. The amplitude of the gravitational wave at the detector depends on the redshift at which it was generated. For a constant observed frequency, the redshift-dependent part in the gravitational wave amplitude is $(1+z)^{5/3}/D_L$. It can also be expressed as $(1+z)^{2/3}/D$, since $D_L = (1+z)D$, where D is the cosmological-radial distance of the source. We study the variation of the quantity $(1+z)^{5/3}/D_L$ for the two cases: (i) a homogeneous and isotropic spacetime described by a flat FLRW metric in the ΛCDM model, and (ii) an inhomogeneous region described by the backreaction formalism, keeping in view that in these two cases the variations of redshift are different.

To depict the change of variation of this quantity $(1+z)^{5/3}/D_L$ in the ΛCDM model of the Universe and in the inhomogeneous Universe described by our two-partitioned model based on the Buchert's backreaction formalism, we plot it w.r.t. redshift z, in (Fig. 3.4) for these two cases. For the ΛCDM model, we have taken

[1] We choose a time-interval of observation $\delta t_0 = 30$ seconds, as for the typical binaries of compact objects, from which gravitational wave signals are detectable by aLIGO and VIRGO, the signal is observed within a time-duration of the order of fractions of seconds to minutes at most.

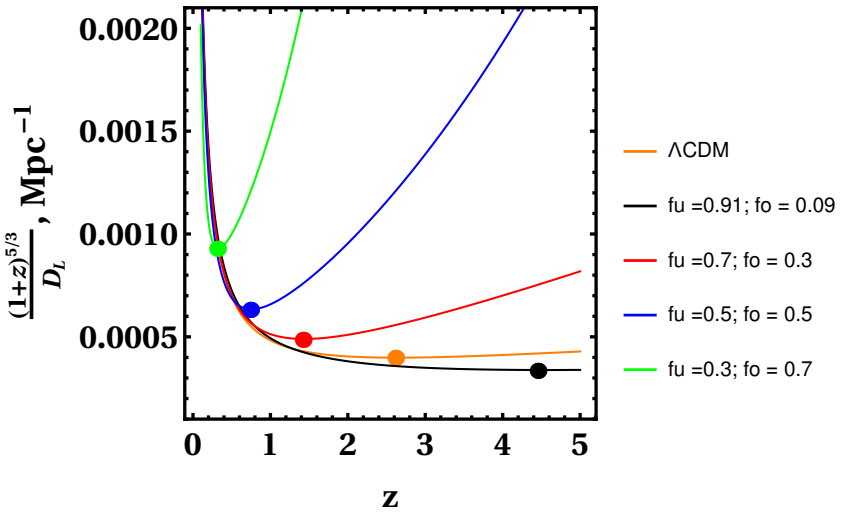

Figure 3.4: Plot of the redshift dependent part of the gravitational wave amplitude for various combinations of the volume fractions fo and fu, with $\beta = 1$. Position of the minima in curves have been denoted by dots. The shifting of the minima points is clearly visualized.

the values of $\Omega_M = 0.31$ and $\Omega_\Lambda = 0.69$, with negligible Ω_R, as is supported by most of the cosmological observations.

For the inhomogeneous Universe, we use a set of different values of the fractions f_o and f_u, as was defined earlier for our two-partitioned model.

We see from (Fig. 3.4) that as the source redshift is increased, the deviation in the $(1+z)^{5/3}/D_L$ increases among different cases considered here. By numerical calculations using *Mathematica*, we find that for the combination $f_u = 0.845$ and $f_o = 0.155$, with $\beta = 1$, variation of the quantity $(1+z)^{5/3}/D_L$ is almost identical to that of the ΛCDM model. The deviation of this term for our two-partitioned model compared to that of the ΛCDM-model increases immensely as we vary the values of fu and fo from the previously mentioned value. We also note that the values of the model parameters, at which the variation of the redshift dependent part of the gravitational wave amplitude with respect to redshift in our model becomes almost identical to the ΛCDM-case, are different from the case for the drift of averaged redshift.

Now, we study the the variation of $(1+z)^{5/3}/D_L$ w.r.t. z for different values of the parameter β, for the combination of fractions $f_u = 0.91$ and $f_o = 0.09$. We see from the (Fig. 3.5) that as the source-redshift is increased, the deviation in the term $(1+z)^{5/3}/D_L$ increases for different curves shown in this graph. Again, as β is gradually decreased from the value 1, the deviation in the term $(1+z)^{5/3}/D_L$ increases for different curves. Using *Mathematica*, we find that for the value of the parameter $\beta = 0.92$, with the combination $f_u = 0.91$ and $f_o = 0.09$, the variation of the quantity $(1+z)^{5/3}/D_L$ in our model is almost identical to that of the ΛCDM model.

Therefore, it is evident that the observed gravitational wave amplitude is sub-

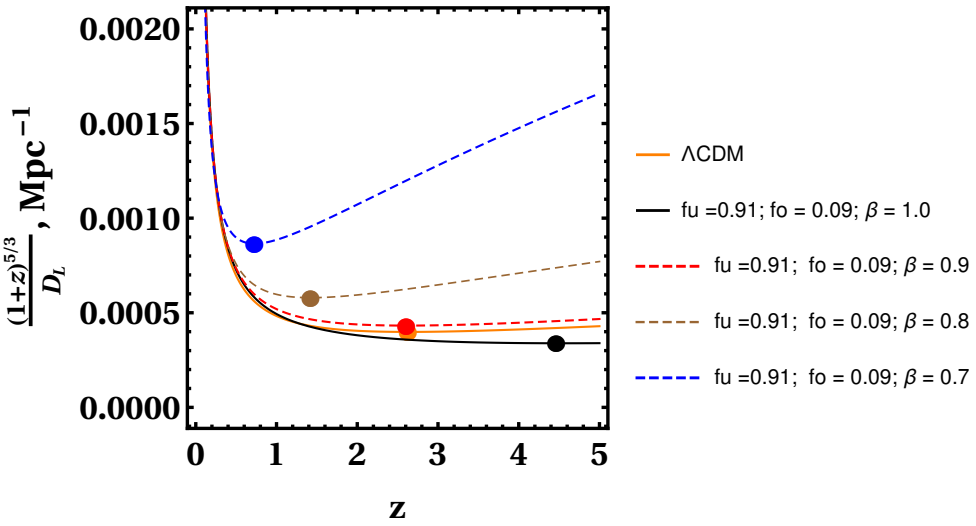

Figure 3.5: Plot of redshift dependent part of the gravitational wave amplitude w.r.t. redshift z, for the ΛCDM model and for our model for different values of the parameter β, for the combination of fractions $f_u = 0.91$ and $f_o = 0.09$. Position of the minima in curves has been denoted by dots. The shifting of the minima points is clearly visualized.

ject to change in our model, in comparison to that of the ΛCDM model, while the amount of change depends on the effect of inhomogeneities in the domain consisting of the path of propagation of the gravitational wave signified by the model parameters f_u, f_o, and β.

An interesting consequence of the changing variation of the redshift-dependent part of gravitational wave amplitude for our model in comparison with the ΛCDM model follows from noting the fact [103] that the quantity $(1+z)^{5/3}/D_L$ has a minimum at z_{min} given by

$$(1+z_{min})\left[\frac{d}{dz}ln[D_L]\right]_{z=z_{min}} = \frac{5}{3} \tag{3.9}$$

We note from the (Fig. 3.4) and (Fig. 3.5), that the quantity $(1+z)^{5/3}/D_L$ has different minima from that of the ΛCDM-model with variation of the model parameters f_u, f_o and β. It has been argued in Ref. [103] that the (Eq. 3.9) is independent of the gravitational wave detector, the model of cosmology under consideration, as well as the binary's characteristics, provided its rest-frame frequency is in the inspiral phase. However, our study clearly indicates that although the (Eq. 3.9) remains the same, the solution it gives for z_{min} varies in the case of our backreaction model. For the ΛCDM model, the value of this minimum is $z_{min} \approx 2.63$. We note from (Fig. 3.4) that z_{min} decreases gradually with the increase in f_o or decrease in f_u for fixed β. Besides this shifting of the z_{min}, the minimum values of the quantity $(1+z_{min})^{5/3}/D_L(z_{min})$ increases with increase in f_o or decrease in f_u. Again, we note from (Fig. 3.5) that for the fixed combination $f_u = 0.91$ and $f_o = 0.09$, z_{min} decreases and the minimum value of the quantity $(1+z_{min})^{5/3}/D_L(z_{min})$ increases if we decrease the parameter β. This shifting can

be said to be an effect of the local inhomogeneities that have been considered in our model.

3.5 Conclusions

In this chapter, we have studied the propagation of gravitational waves from compact binary sources through a background spacetime, which, due to the presence of structures in the late-time Universe, may not be correctly described by the flat FLRW metric at the relevant scales. In order to take into account the effect of inhomogeneities, we have employed Buchert's backreaction formalism [25, 27] in the framework of which we consider a two-partitioned toy model. Evolution under this model is shown to lead to a modification in the redshift versus distance relation as well as in the drift of the averaged redshift in comparison with the ΛCDM model, in agreement with similar earlier results [35] within the backreaction framework.

Our analysis exhibits a substantial deviation in the variation of the redshift dependent part of the amplitude of gravitational waves generated from binaries of compact objects in their early inspiral stages, in the two cases, *viz.*, (i) the ΛCDM model, and (ii) our model based on Buchert's backreaction formalism. We have investigated the latter model for various combinations of the model parameters, such as the volume fractions of overdense and underdense regions, as well as the rate of expansion of the underdense region. We find that only for very specific combinations of the above parameters, the variation of the redshift-dependent part of the amplitude of gravitational wave matches with that of the ΛCDM case. The deviation of the variation increases with the increasing effect of inhomogeneities, quantified by the volume fractions and the void expansion rate. Our results further display an interesting shift in the minima of the redshift-dependent part of the gravitational wave amplitude, which is a clear consequence of the backreaction from inhomogeneities.

Before concluding this chapter, we would like to make the following comments. In the present era of precision cosmology with several upcoming probes, the determination of properties of distant sources of gravitational waves will play an important role in several domains of astrophysics and cosmology. The significance of precise determination of gravitational wave observables has spurred many recent works on ascertaining the role of effects such as primordial black hole accretion [104, 105], and various phase transitions and inflationary scenarios [106]. On the other hand, our present work investigates the role of observed structure in the Universe on gravitational wave propagation, using the backreaction framework [25, 27] without invoking non-standard physics. Through our analysis, we have found a clear signature of backreaction in the shift of the gravitational

wave amplitude minima in the context of our simplified two-domain model. Our present analysis should inspire further detailed calculations using more sophisticated backreaction scenarios, such as multi-domain models, in order to provide more accurate predictions of the quantitative deviation of gravitational wave observables from those obtained in ΛCDM cosmology.

Chapter 4

Viscous attenuation of gravitational waves propagating through an inhomogeneous background

4.1 Introduction

The century-old prediction of the possible existence of Gravitational waves (GWs) in Einstein's theory of General Relativity [77, 78] has recently found confirmation from the Laser Interferometer Gravitational-Wave Observatory (LIGO), and Virgo scientific collaborations [93–97, 107], which has opened a new window to decipher the mysteries of Universe. With more and more GW data pouring in, one expects that the GWs will provide more insight into diverse phenomena, such as the origins of black holes, the extreme conditions inside neutron stars, the chronicle of how the Universe structured itself into galaxies, the physics of the first few moments in the aftermath of the Big-bang and the standard picture of Universe itself.

Since gravitational wave observations are used to infer various fundamental properties related to the source of emission, it is important to have a complete understanding of the physics of their propagation from the source to us through the intervening background which in the present Universe is dominated by the dark components, *viz.*, dark matter and dark energy. Properties of the cosmic fluid could be a cause for significant attenuation of the amplitude of GWs propagating through it. It may be noted that though electromagnetic (EM) waves are not affected by the viscosity of matter, GWs are indeed affected by viscosity [108–114]. GWs have to work against the viscous matter while passing through it, resulting in a loss of their energy, which is manifested in attenuation of am-

plitude or damping of the GWs. [1] Studies [115] have been done analyzing the interaction between a viscous fluid (the primordial plasma in this case) and the primordial gravitational waves using a relativistic hydrodynamic theory. There also exist studies [116, 117] describing the damping of GWs due to non-collisional media during propagation in alternative gravitational theories. For example, it is possible for the longitudinal scalar modes of the GWs from Horndeski theories to be damped by the non-collisional ensemble of massive particles.

Cosmologists have used viscosity in wide-ranging studies over the years. The initial singularity at the Big Bang can be avoided by invoking shear and bulk viscosity [118, 119]. Viscosity has been used to explain dark energy [120–122], and it has been shown that the Universe's accelerated expansion can be due to the effect of viscosity [118, 121–126]. In certain other schemes, the neutrino mass [127] and the 21-cm emission temperature [128] can also be constrained using viscous cosmology. The viscous matter in the path of propagation of GWs could be most likely in the form of certain types of dark matter [123, 129–132], though even some of the visible stellar matter may also have some amount of viscosity. Such dark matter with dissipative dynamics induced by viscosity can possibly settle the strain between Planck Cosmic Microwave Background (CMB) and Large Scale Structure (LSS) observations [133]. GWs in the presence of viscosity have been suggested as probes of such viscous cosmological models [113].

As highlighted in (Chap. 1), cosmological observations have revealed that there is significant inhomogeneity in matter distribution in the Universe on scales as large as 500 h^{-1} Mpc [9].

As argued in (Chap. 2), these local inhomogeneities may impact the overall evolution of the Universe, through the backreaction arising from the process of averaging [12, 13, 19, 22, 23, 25, 27]. Recently, the Hubble tension [6, 7] arising from a discrepancy in the inferred value of the Hubble parameter from local measurements compared to that from early Universe physics has attracted a lot of attention. It may be noted that backreaction-induced curvature may possibly explain the larger values of the Hubble parameter obtained locally [134].

Generally, GW analysis is done by deeming that GW propagates through a homogeneous and isotropic spacetime, described by an FLRW metric. However, GW sources which are the subject of the present observations [93–97, 107] lie well within the scale of 500 h^{-1} Mpc. The analysis of the effect of inhomogeneities on the propagation of GWs may be of significance for precision measurements in the emerging field of GW astronomy.

The motivation of the present analysis is to study the propagation of GWs through a background containing viscous dark matter in the presence of inhomogeneities. It has been shown earlier that the inclusion of the effect of local

[1] It may be mentioned that similar damping occurs in EM waves when they traverse through any matter having sufficiently high conductivity.

inhomogeneities leads to a non-trivial impact on the propagation of EM waves in averaged spacetime [21, 58, 64–67, 135]. The cosmological-distance versus redshift relations get modified due to averaging over inhomogeneities [20, 35, 36], leading to interesting prospects for the detection of signatures of inhomogeneities through observations of Hubble expansion [42]. GWs act as fellow carriers of information to EM waves, and analysis pertaining to the former opens up a new avenue to the physics of the evolution of the Universe starting from early times, offering insight into the nature of gravity itself, and ranging to the current cosmic acceleration.

GWs have particular relevance for those sources which do not emit any EM signals. Here we consider compact objects in binary formations, e.g., black hole - black hole (BH-BH) binaries, from which emitted GWs can be detected after traversing through the background viscous fluid. We consider the background dynamics arising from the backreaction of inhomogeneities due to structure formation. Specifically, we employ the Buchert formalism discussed in (Chap. 2) to quantify the effect of backreaction. In (Chap. 3), it was shown using the Buchert framework that the amplitude of GWs produced from binaries could deviate substantially from that in the case of a homogeneous spacetime described by the ΛCDM model [47].

In this chapter, we show that the local *viscous-inhomogeneities* in the path of propagation of GWs may have a considerable impact on the GW observables. The inclusion of viscosity affects the GW observables in ways different from the case of its absence [47]. In the context of a simplified two-partitioned model of inhomogeneities within the context of the Buchert framework, here we evaluate the attenuation of GWs resulting from our model in comparison with the standard analysis of the ΛCDM model. Our approach clearly brings out the quantitative differences in the GW signal due to the inclusion of effects of viscosity and inhomogeneities, in combined as well as separate ways.

The chapter is organized as follows. A brief description of the background dynamics is provided in (Sec. 4.2). Here we first discuss a viscous ΛCDM model and next describe our inhomogeneous two-partitioned model (for both viscous and non-viscous cases) within Buchert's averaging formalism. In (Sec. 4.3), the modification of the redshift-distance relation due to the averaging procedure is presented. In (Sec. 4.4), the effect of local viscous inhomogeneities on the redshift-dependent part of the GW amplitude is demonstrated. Finally, we present concluding remarks in (Sec. 4.5).

4.2 Background dynamics

For the ΛCDM model (without viscosity), the Hubble parameter is given by the Friedmann equation

$$H^2(a) = H_0^2\left(\frac{\Omega_{m0}}{a^3} + \frac{\Omega_{r0}}{a^4} + \frac{\Omega_k}{a^2} + \Omega_\Lambda\right) \tag{4.1}$$

where a is the scale factor, H_0 is the present value for the Hubble parameter, Ω_{m0} denotes the fractional matter density components (assumed pressure less) of the Universe, Ω_{r0} is the fractional radiation density term, Ω_k is the term related to the curvature, and Ω_Λ denotes the cosmological constant component. In practice, the contribution of the radiation at late times (i.e., at the time of structure formation) is negligible compared to the matter and cosmological constant terms. Also, observations indicate that the geometry of the Universe is almost flat, *viz.*, $\Omega_k \approx 0$.

4.2.1 Viscous ΛCDM model (vΛCDM)

GW may propagate through dark matter in its path from its source to the observer. There are various theoretical models of dark matter. One of these is the Self-Interacting Dark Matter (SIDM) model [129–132]. In this model, self-interaction is introduced between the dark matter particles, which results in dissipation in the dark matter fluid. The outcome of this dissipation is the introduction of coefficients of shear and bulk viscosities [123]. In our approach, the dark matter behaves as a viscous/dissipative component. The general structure of this model is given by the field equation [136]

$$R_{\mu\nu} - \frac{1}{2}g_{\mu\nu}R + \Lambda g_{\mu\nu} = 8\pi G T_{\mu\nu} \tag{4.2}$$

where $R_{\mu\nu}$ represents the Ricci tensor, R represents the Ricci scalar, $g_{\mu\nu}$ is the metric tensor, Λ is the cosmological constant and $T_{\mu\nu}$ stands for the energy-momentum tensor of the viscous matter. This tensor possesses both the perfect fluid structure as well as the possible dissipative effects, such that [136, 137]

$$T^{\mu\nu} = pg^{\mu\nu} + (p+\rho)u^\mu u^\nu + \Delta T^{\mu\nu} \tag{4.3}$$

where ρ is the density, p is the pressure and the component $\Delta T^{\mu\nu}$ is the viscous contribution to the fluid,

$$\Delta T^{\mu\nu} = -2\eta\sigma^{\mu\nu} - \xi\Theta(g^{\mu\nu} + u^\mu u^\nu) \tag{4.4}$$

Here ξ is the bulk viscosity, η is the shear viscosity, $\Theta = u^\mu_{;\mu}$ is the expansion,

u^μ is the 4 - velocity and ";" represents the covariant derivative. For simplicity, we set the pressure, $p = 0$. Then, our dark matter possesses only the viscous pressure given by [138]

$$p_v = -\xi u^\mu_{;\mu} \tag{4.5}$$

In the FLRW metric, the bulk viscous pressure reduces to

$$p_v = -3H\xi \tag{4.6}$$

Dark matter physics can incorporate some possible dissipative mechanisms [123, 129–133]. Only the bulk viscosity remains compatible with the assumption of large-scale homogeneity and isotropy. The other processes, like shear and heat conduction, are directional mechanisms that decay as the Universe expands. Shear viscosity has mostly been neglected in these studies on the grounds of not contributing to a homogeneous and isotropic universe, which is undoubtedly true at the large-scale background level [138, 139]. Hence, for our purpose, for this viscous ΛCDM model, shear viscosity does not contribute to the dynamics of an isotropic and homogeneous background. However, shear viscosity does indeed play a role in the attenuation of gravitational waves, as we will see later in (Sec. 4.4).

Now, for a viscous ΛCDM model, using the FLRW metric, the Friedmann equation reads,

$$H^2 \equiv \left(\frac{\dot{a}}{a}\right)^2 = \frac{8\pi G}{3}\rho_v + \frac{\Lambda}{3}. \tag{4.7}$$

Here, ρ_v stands for the density of viscous matter and denotes all the matter components. We have assumed that all the matter components are endowed with viscous properties. For our purpose here, a proper separation between baryons and dark matter is unnecessary. One should also recall that baryons contribute about $1/6^{th}$ of the present total matter distribution; thus, this is not expected to lead to appreciable changes in our analysis, as baryonic matter is a subdominant component in comparison to dark matter. By defining the fractional densities $\Omega_v = 8\pi G\rho_v/(3H_0^2)$ and $\Omega_\Lambda = \Lambda/(3H_0^2)$, where H_0 is the present value for the Hubble parameter, the Friedmann equation (Eq. 4.7) becomes

$$H^2 = H_0^2(\Omega_v + \Omega_\Lambda) \tag{4.8}$$

Using now the fluid equation for ρ_v, one gets

$$\dot{\rho}_v + 3H(\rho_v + p_v) = 0. \tag{4.9}$$

(Eq. 4.9) can be recast as an equation for the fractional density Ω_v as

$$a\frac{d\Omega_v}{da} + 3\Omega_v(1+\omega_v) = 0 \tag{4.10}$$

where we have defined the fluid equation of state parameter for the viscous dark matter fluid, ω_v, as

$$\omega_v \equiv \frac{p_v}{\rho_v} = -\frac{3H\xi}{\rho_v} \tag{4.11}$$

Using this formalism, Ω_v as a function of the red-shift z is calculated. The corresponding quantity in the ΛCDM case is $\Omega_{m0}(1+z)^3$ (Eq. 4.1).

4.2.2 A model of backreaction in Buchert's formalism

In this work, we investigate the simultaneous impact of inhomogeneities and viscosity of the matter contained in the overdense region on the amplitude of GWs for the same type of sources. For incorporating the effect of matter distribution inhomogeneities, we have employed Buchert's averaging procedure outlined in (Chap. 2).

We consider two cases - (a) when the GW is assumed to propagate through a homogeneous and isotropic spacetime (with and without viscosity of associated matter), described by the FLRW metric, in the ΛCDM model, and (b) when the GW propagates through an inhomogeneous spacetime (both viscous and non-viscous cases), described by our model specified above. The physical interpretation of the underdense region in our model is that it represents the cosmic voids in the path of propagation of the GWs, and the overdense region represents all the matter content in that path. In this work, we have considered both scenarios (viscous and non-viscous) for the matter present in the overdense region of our model. A point to note here is that we are not considering viscous matter in addition to non-viscous matter. The total matter content in both the non-viscous case and the viscous case is the same. It's just that in the viscous case, the matter content has viscous properties too. The overdense viscous region in our model portrays a viscous dark matter fluid.

4.2.2.1 Non-viscous case (no bulk and shear viscosity)

Expressions for the scale factors for the two types of regions, overdense (non-viscous in this case) and underdense, for this model, are given as [44, 45],

$$a_o = c_o t^{\alpha}, \tag{4.12}$$

$$a_u = c_u t^{\beta}. \tag{4.13}$$

Here, o represents the overdense region, and u represents the underdense re-

gion. In this model, the scale factors of the two regions are proportional to cosmic time raised to some powers α and β for over- and under-dense regions, respectively. α varies from 1/2 to 2/3 since the evolution of a_u is expected to be faster than that for the radiation-dominated case (1/2) and limited by the maximum value for the matter-dominated case (2/3). β varies from 2/3 to 1 to denote any behaviour ranging from a matter-dominated region ($\beta = 2/3$) up to a dark energy-dominated region ($\beta > 1$). c_u and c_o are constants of proportionality and are given respectively as:

$$c_o = \frac{a_{D_0}}{t_0^\alpha},$$
$$c_u = \frac{a_{D_0}}{t_0^\beta},$$

where a_{D_0} is the scale factor at the present time for the domain D. For present time $t_0 \approx 13.8\,Gy$, $a_{D_0} = 1$ and $H_0 = 100\ h$ km $sec^{-1}\ Mpc^{-1}$. Therefore,

$$c_o = \frac{1}{t_0^\alpha}, \tag{4.14}$$
$$c_u = \frac{1}{t_0^\beta}, \tag{4.15}$$

Using (Eq. 2.24) for our model we get,

$$\frac{\ddot{a}_D}{a_D} = \lambda_o \frac{\ddot{a}_o}{a_o} + \lambda_u \frac{\ddot{a}_u}{a_u} + 2\lambda_o\lambda_u(H_o - H_u)^2. \tag{4.16}$$

Here $\lambda_o = V_o/V_D$ is the volume fraction for the overdense region, V_o is the volume of the overdense region and λ_u is the volume fraction of underdense region such that $\lambda_u + \lambda_o = 1$. Now, using (Eq. 2.9), V_o can be written in terms of scale factor and initial volume fraction, $\lambda_o = \frac{a_o^3 V_{o_0}}{a_D^3 V_{D_0}}$, where V_{o_0} is the volume of the overdense region at some reference time t_0. This, in turn, gives us,

$$\lambda_o = k_1 \frac{t^{3\alpha}}{a_D^3}. \tag{4.17}$$

where $k_1 = \frac{\lambda_{o_0} a_{D_0}^3}{t_0^{3\alpha}}$ is a constant and λ_{o_0} , a_{D_0} , t_0 are the present volume fraction of overdense region, the present global scale factor and the present time, respectively. (Eq. 4.17) shows that the volume fraction of the overdense region is a function of α and β (through a_D as a_D is a function of both α and β). Similarly, it can be shown that the volume fraction of the underdense region is a function of α and β. This implies that (α, β) governs the volume fractions of the 2 subregions in our 2-domain model. The present values of volume fractions of the 2 region are taken as $(\lambda_{o_0}, \lambda_{u_0}) = (0.09, 0.91)$ [27]. Solving (Eq. 4.16) gives us an expression

for a_D, and using that expression in (Eq. 2.13) gives us an expression of $\langle\rho\rangle_D$ for our model.

4.2.2.2 Viscous case

The sub-regions in our backreaction model are essentially FLRW regions. Hence, their dynamics are also governed by the standard Friedmann equations (Eq. 4.1, Eq. 4.7). Only our overdense region has viscous matter contained in it. So, for our overdense region, the Friedmann equation reads (we have taken $\Lambda = 0$),

$$H_{v_o}^2 \equiv \left(\frac{\dot{a_{v_o}}}{a_{v_o}}\right)^2 = \frac{8\pi G}{3}\rho_{v_o}. \tag{4.18}$$

Here, a_{v_o} is the scale factor for our viscous overdense region, H_{v_o} is the Hubble parameter for our viscous overdense region, and ρ_{v_o} stands for the density of viscous matter in our overdense region and denotes all the matter components. We have assumed that all the matter components of our overdense region are endowed with viscous properties similar to the ΛCDM model with viscosity. Also, since our overdense region is an FLRW region (homogeneously and isotropically overdense), here too the shear viscosity with coefficient η doesn't have any effect on the dynamics of the background. The fluid equation for ρ_{v_o} is given by,

$$\dot{\rho_{v_o}} + 3H_{v_o}(\rho_{v_o} + p_{v_o}) = 0. \tag{4.19}$$

where p_{v_o} is the bulk viscous pressure given by

$$p_{v_o} = -3H_{v_o}\xi \tag{4.20}$$

By defining the fractional densities $\Omega_{v_o} = 8\pi G\rho_{v_o}/(3H_0^2)$, equation for the fractional density Ω_{v_o} is given as,

$$a_o\frac{d\Omega_{v_o}}{da_o} + 3\Omega_{v_o}(1 + \omega_{v_o}) = 0 \tag{4.21}$$

where we have defined the fluid equation of state parameter for the viscous dark matter fluid for our overdense region, ω_{v_o}, as

$$\omega_{v_o} \equiv \frac{p_{v_o}}{\rho_{v_o}} = -\frac{3H_{v_o}\xi}{\rho_{v_o}} \tag{4.22}$$

Since (Eq. 4.21) is a first-order differential equation, we require one boundary condition to solve it. We take this boundary condition from our non-viscous backreaction model, given by

$$\Omega_{v_o}(z = 0) = \Omega_o(z = 0) \tag{4.23}$$

where Ω_o is the fractional density of the overdense region from the non-viscous case.

The scale factor for our overdense region in our viscous backreaction model is calculated using (Eq. 4.22, Eq. 4.21, and Eq. 4.18). The boundary condition used for solving (Eq. 4.21) is (Eq. 4.23). The a_{vo} that we get from the above-mentioned analysis is a function of (α, β). The scale factor for the underdense region, a_u, is still given by (Eq. 4.13). The scale factor for domain D in this case a_{vD} is given by,

$$\frac{\ddot{a}_{vD}}{a_{vD}} = \lambda_o \frac{\ddot{a}_{vo}}{a_{vo}} + \lambda_u \frac{\ddot{a}_u}{a_u} + 2\lambda_o\lambda_u(H_{vo} - H_u)^2 \tag{4.24}$$

The equation for the backreaction term in this case, Q_{vD} is given by ($Q_u = 0; Q_o = 0$),

$$Q_{vD} = 6\lambda_o(1 - \lambda_o)(H_{vo} - H_u)^2, \tag{4.25}$$

Solving (Eq. 4.24) gives us an expression for a_{vD}. (Eq. 4.25) leads to an expression for Q_{vD}. Using these expressions in (Eq. 2.13), we get an expression of $\langle\rho\rangle_{vD}$ for our viscous backreaction model. The present value of the bulk viscosity parameter has been estimated in the literature based on various theoretical considerations and observations [114, 126, 140, 141]. By solving the energy conservation equation for bulk viscous flat Friedmann universes, the coefficient of bulk viscosity at the present time ξ has been estimated to be $\sim 10^6$ Pa sec in [141]. Other analyses based on comparing the theoretical curves for $H = H(z)$ with observations [142], and by studying the asymptotic behaviour in the equivalent phase space in a Friedmann model of the Universe with bulk viscous matter [143] have also been performed. In [144], a value of $\sim 10^7$ Pa sec for ξ has been suggested. Considering all the above studies, a reasonable range for ξ may be taken as 10^5 Pa sec $< \xi_0 < 10^7$ Pa sec. For our present work, we have used the mid-range value of 10^6 Pa sec in the red-shift range $0 \leq z \leq 5$.

In (Fig. 4.1) we provide a plot of the Hubble parameter versus the redshift for ΛCDM, viscous ΛCDM, and for our viscous backreaction model for various values of the backreaction model parameters. The underdense region in our model represents the cosmic voids in the path of propagation of the GWs, and the overdense region represents all the matter content in that path, where the effect of viscosity is directly evident. In (Fig. 4.1), for the plots of our viscous backreaction model, we fix the value of β at 0.8 (representing a mid-range value in the range of values of β - (2/3, 1)), and we vary the values of α. As expected, for a fixed β, curves with larger values of α lead to larger values of the Hubble parameter. It can be seen that backreaction from inhomogeneities may lead to a departure from the background Hubble evolution that may get accentuated for higher redshifts.

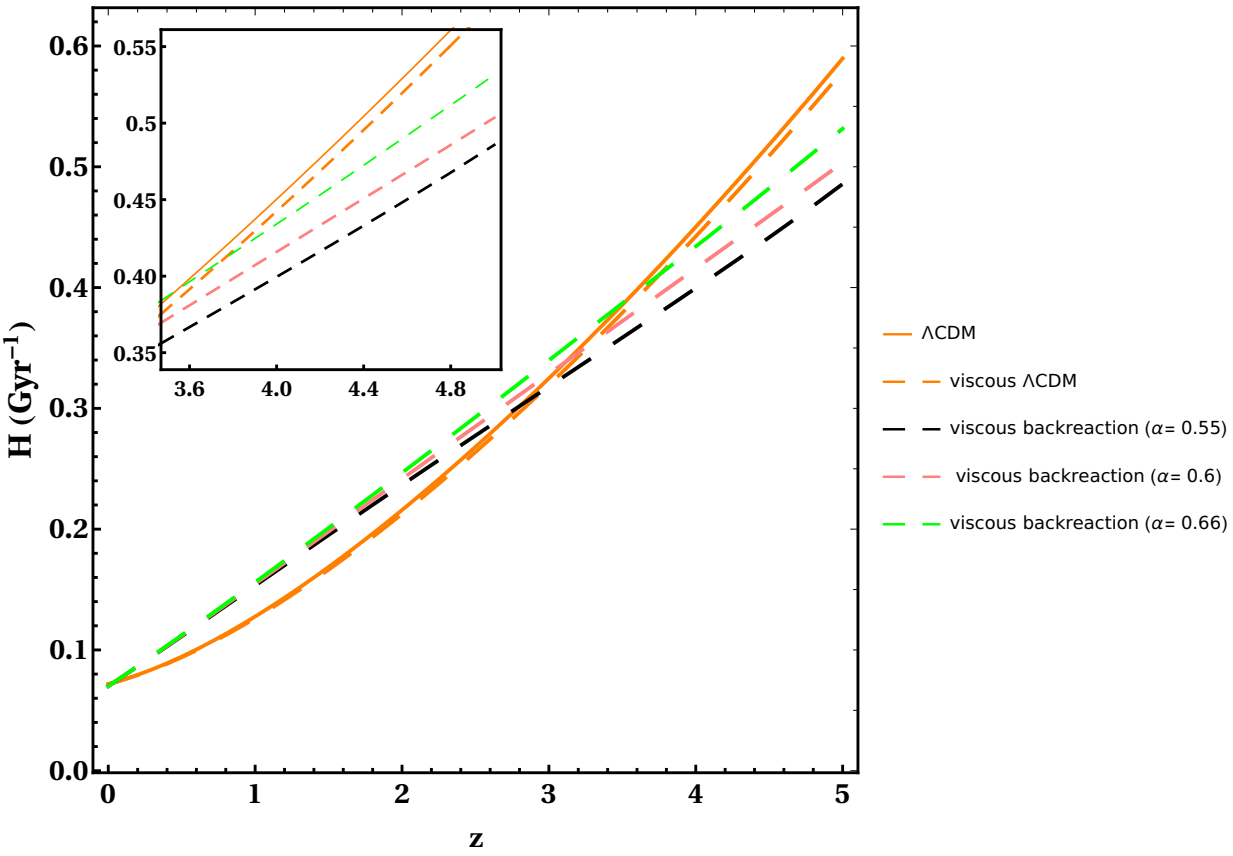

Figure 4.1: Plot of Hubble parameter vs redshift z for the ΛCDM model, viscous ΛCDM model and our viscous backreaction model. Plots for our viscous backreaction model are for varying values of α with a fixed value of $\beta = 0.8$. The value of ξ used is 10^6 Pa sec. The value of H_0 used is 100 h km s^{-1} $Mpc^{-1} \simeq 0.07$ Gyr^{-1}, with h = 0.7. Parameters used for ΛCDM are $\Omega_m = 0.31$, $\Omega_\Lambda = 0.69$. The inset shows the magnified portion of the plots at higher redshift values.

4.3 Redshift and distance relation

Buchert's averaging scheme provides us with a method of spatially averaging scalar quantities in the backreaction framework. Such quantities need to be related to cosmological observables. We have employed the covariant scheme discussed in detail in (Sec. 2.2) for this purpose.

Certain conditions must be satisfied to apply the covariant scheme. These are: (i) spatial averages are determined on hypersurfaces of statistical homogeneity and isotropy, and (ii) structure evolution is slow compared to the travel time of GW from the source to the observer.

For our model, domain D is the region of spacetime through which the GW travels while propagating from the source to the observer. Domain D could have any combination of fractions of underdense and overdense regions, i.e. any combination of (λ_u, λ_o) as long as $\lambda_u + \lambda_o = 1$ is satisfied. (λ_u, λ_o) in turn are governed by (α, β). In this work, we take various combinations of allowed values of (α, β) in our analysis. Using the expressions for H_D and $\langle \rho_D \rangle$ that we calculated from our model for the two cases - viscous (with only ξ, but no η since η doesn't

affect the background) and non-viscous, and using the covariant scheme (Eq. 2.25, Eq. 2.26), we can calculate D_A for our model.

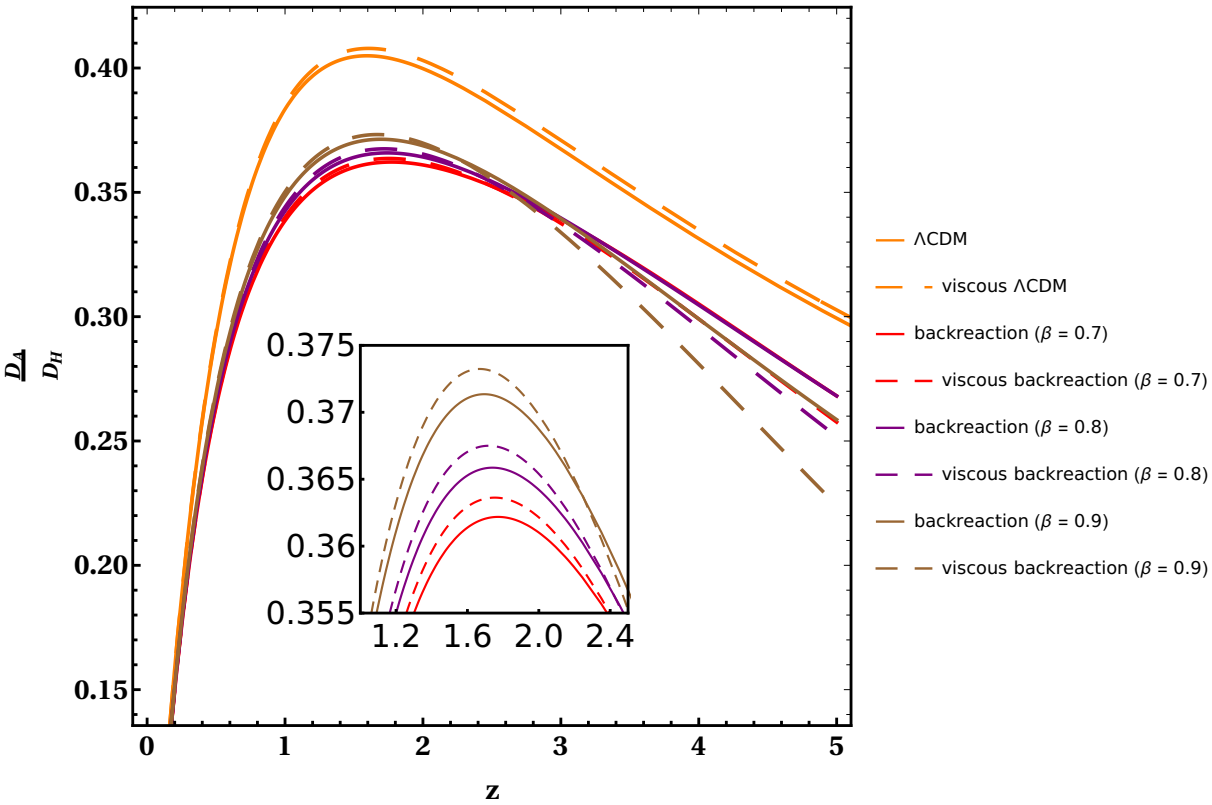

Figure 4.2: Plot of the ratio of angular diameter distance D_A to the present Hubble length D_H w.r.t. redshift, for the ΛCDM case and for our backreaction model with different combinations of β and fixed value of $\alpha = 0.5$ for both viscous and non-viscous cases. Value of ξ used is 10^6 Pa sec. Parameters used for ΛCDM are $\Omega_m = 0.31$, $\Omega_\Lambda = 0.69$. The inset shows a magnified portion of the plots for our backreaction model.

In (Fig. 4.2), we plot the ratio of angular diameter distance for our model to the present Hubble-length ($D_H = cH_0^{-1}$, value of H_0 (present value of H) used is 100 h km s^{-1} $Mpc^{-1} \simeq 0.07$ Gyr^{-1}, with h = 0.7) as a function of effective redshift with different combinations of (α, β). We have studied earlier the effect of varying α on the dynamics (Fig. 4.1). Here in (Fig. 4.2) we explore the effect of varying β on the angular diameter distance, choosing a fixed value of $\alpha = 0.5$. The value of ξ used is 10^6 Pa sec in the range $0 \leq z \leq 5$ [114]. From this figure, one can see that for low redshifts (z < 0.5), curves for our model overlap with each other and with the ΛCDM curve, but as we increase the redshift, curves start deviating from the ΛCDM curve. Inclusion of viscosity in the analysis results in deviation in the plots for both the ΛCDM model and our model. For the ΛCDM case, the plot of the viscous case (dashed) has a higher magnitude than the non-viscous case (solid). It is observed that for lower values of z ($z \lessapprox 2$), plots of viscous cases (dashed curves) for our backreaction model have a higher magnitude of D_A for the same value of z in comparison to corresponding non-viscous cases (solid curves) and for $z \gtrapprox 2$, the magnitude of D_A for viscous cases (dashed curves) are

smaller than those for the non-viscous cases (solid curves) for our model.

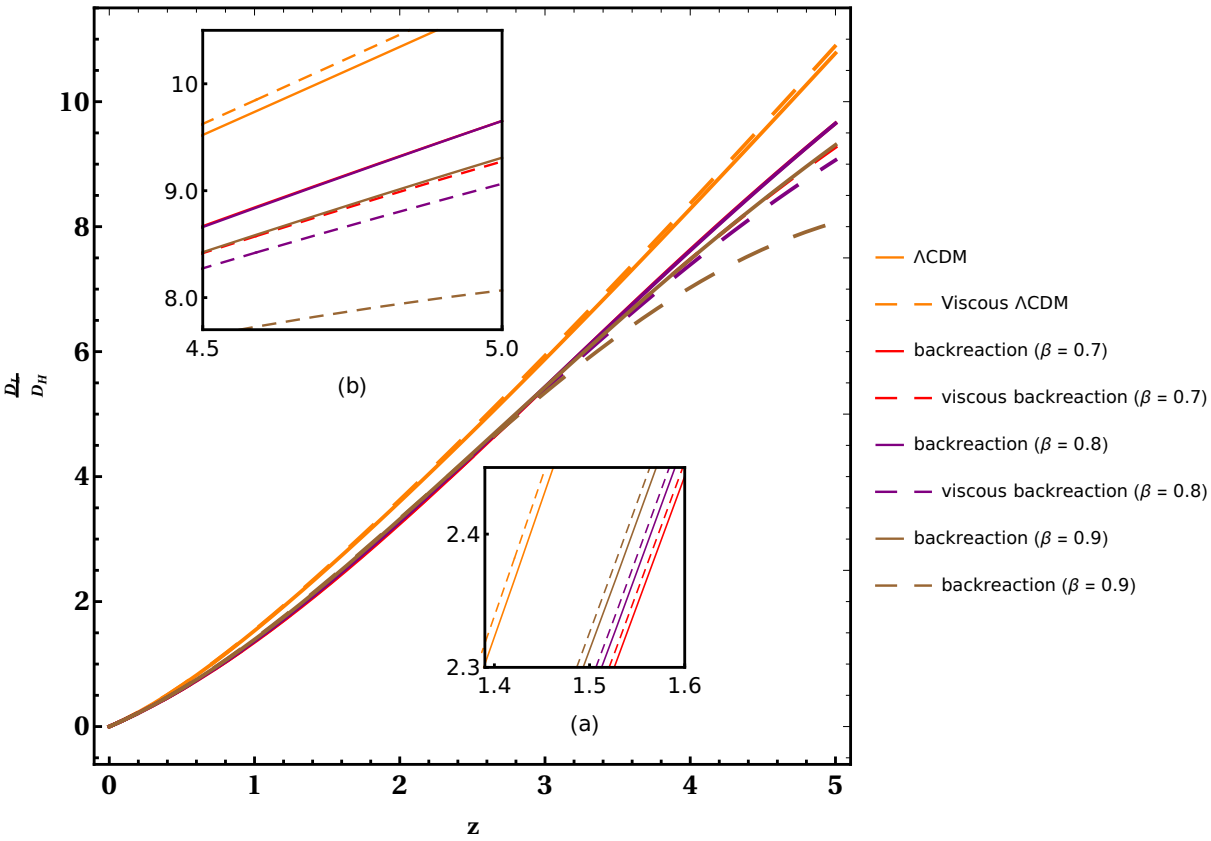

Figure 4.3: Plot of the ratio of luminosity distance D_L to the present Hubble length D_H w.r.t. redshift, for the ΛCDM case and for our backreaction model with different combinations of β and fixed value of $\alpha = 0.5$ for both viscous and non-viscous cases. The value of ξ used is 10^6 Pa sec. Parameters used for ΛCDM are $\Omega_m = 0.31$, $\Omega_\Lambda = 0.69$. There are two insets in the figure. Inset (a) shows the magnified portion of the plots at lower values of redshift, from $z = 1.4$ to $z = 1.6$. Inset (b) shows the magnified portion of the plots at higher values of redshift, from $z = 4.5$ to $z = 5$.

In (Fig. 4.3), the ratio of luminosity distance D_L to the present Hubble length D_H is plotted with respect to redshift z for both viscous and non-viscous cases of ΛCDM and our backreaction model. D_L is calculated from D_A (Fig. 4.2) using the relation $D_L = (1+z)^2 D_A$. There are two insets in the figure. It can be seen here too that for low redshifts (z < 0.5), the curves for our model overlap with each other and with the ΛCDM curve, but as we increase the redshift, the curves start deviating from the ΛCDM curve. Inset (a) shows the magnified portion of the plots at lower values of redshift, particularly around the value of z for which the plots of D_A/D_H turn around in (Fig. 4.2). As in (Fig. 4.2), plots for the viscous backreaction model (dashed curves) have a larger magnitude than the non-viscous case (solid curves) for about $z \lessapprox 2$. For $z \gtrapprox 2.5$, plots for the viscous case have a smaller magnitude than the non-viscous case, similar to plots in (Fig. 4.2). This behaviour is shown in the inset (b). A point to note is that this behaviour is not observed for the ΛCDM case, where viscous case plots have a larger magnitude throughout the range of z of our interest. In inset (b), purple

(backreaction ($\beta = 0.8$)) and red (backreaction ($\beta = 0.7$)) plot lines overlap, which is similar to the case of (Fig. 4.2) at this value of z. Another feature of the plots for our backreaction model can be observed at higher redshift z. It can be seen that the difference between the solid and dashed lines (representing the non-viscous and viscous cases, respectively) increases with larger values of β. Specifically, the difference between the red lines is smallest for the lowest values of β, while the difference between the brown lines is largest for the highest values of β.

4.4 Gravitational wave amplitude

The amplitude of GW from a binary of compact objects of masses m_1 and m_2 in the early inspiral stage, where Keplerian approximations are well valid, is given by (for the cross(×)-polarization) [79]

$$h_\times = \frac{G^{5/3}(1+z)^{5/3}}{D_L c^4} * \frac{m_1 m_2}{(m_1+m_2)^{1/3}}(-4\omega^{2/3}) Sin\, 2\omega t\,, \tag{4.26}$$

where ω is the observed angular frequency of the binary of compact objects and D_L is the luminosity distance of the binary from the observer. For the plus (+)-polarization, the peak of the amplitude remains identical. For a constant observed frequency, the redshift-dependent part in the GW amplitude is $(1+z)^{5/3}/D_L$.

The amplitude of GW given in (Eq. 4.26) is derived without considering the effect of viscosity on the propagation of the GW. In Ref. [113], the authors have studied the effect of the viscosity of the cosmic fluid, particularly dark matter, on the GW amplitude and have estimated its effect on the GW amplitude. Assessing the impact of viscosity, after traveling a proper distance $L = ar$, the GW gets attenuated by the factor (see Appendix A)[113]

$$\mathscr{A} = L_* e^{-\frac{\gamma}{2}L}/L, \tag{4.27}$$

where L_* is the proper source distance for zero shear viscosity and $\gamma = 16\pi G\eta$, where η is the coefficient of shear viscosity for the region through which GW is propagating. The attenuation factor in terms of luminosity distance D_L is given by :

$$\mathscr{A} = \frac{D_{L_*}}{D_L} e^{-\frac{\gamma}{2(1+z)^2}D_L}, \tag{4.28}$$

where $D_L = (1+z)^2 L$. D_{L_*} is the luminosity distance of the source, for zero shear viscosity. Therefore, the total redshift-dependent part of the attenuated GW amplitude (let's represent this quantity by $F(z)$) is given by

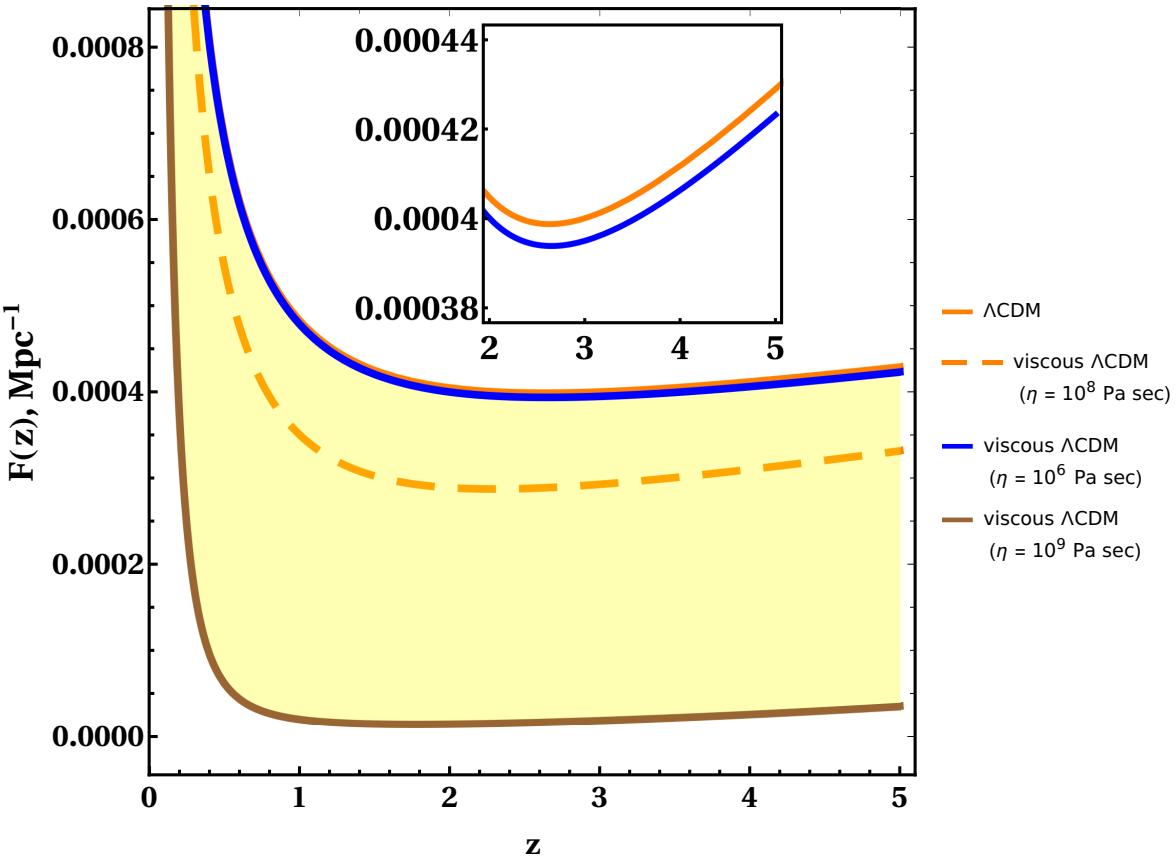

Figure 4.4: Plot of $F(z)$ for the ΛCDM model for both viscous and non-viscous cases. The value of ξ used is 10^6 Pa sec. Plots for viscous cases are for the applicable range of values of η between $\sim 10^6$ Pa sec and $\sim 10^9$ Pa sec. The dashed orange plot represents the favored value of η. Parameters used for ΛCDM are $\Omega_m = 0.31$, $\Omega_\Lambda = 0.69$. The inset shows the magnified portion of the plot for the ΛCDM model and for our backreaction model ($\eta = 10^6$ Pa sec).

$$F(z) = \frac{(1+z)^{5/3}}{D_{L_*}}\mathscr{A} = \frac{(1+z)^{5/3}}{D_{L_*}}\frac{D_{L_*}}{D_L}e^{-\frac{\gamma}{2(1+z)^2}D_L} = \frac{(1+z)^{5/3}}{D_L}e^{-\frac{\gamma}{2(1+z)^2}D_L}. \tag{4.29}$$

For non viscous case ($\eta = 0$),

$$F(z,\eta=0) = \frac{(1+z)^{5/3}}{D_L} \tag{4.30}$$

The luminosity distance D_L is calculated from angular diameter distance, D_A as $D_L = (1+z)^2 D_A$. Since, $D_L = (1+z)^2 L$, for the flat FLRW spacetime, D_A gives a good measure of the proper distance L. D_A for flat spacetime is given by

$$D_A = \frac{D_C}{(1+z)} = \frac{D_H}{(1+z)}\int_0^z \frac{dz'}{E(z')} \tag{4.31}$$

where D_C is the comoving distance which is given as $D_H \int_0^z \frac{dz'}{E(z')}$ where D_H is the Hubble distance ($= \frac{c}{H_0}$, where $H_0 = 100\ h$ km s^{-1} $Mpc^{-1} \simeq 0.07\ Gyr^{-1}$, with h = 0.7.) and $E(z)_{\Lambda CDM} \equiv \sqrt{\Omega_M(1+z)^3 + \Omega_\Lambda}$ for the ΛCDM model (non-viscous

case) (throughout this work, parameters used for ΛCDM are $\Omega_m = 0.31$, $\Omega_\Lambda = 0.69$.) and $E(z)_{v\Lambda CDM} \equiv \sqrt{\Omega_v + \Omega_\Lambda}$ for the viscous ΛCDM model, where Ω_v is the fractional density for viscous matter which has a contribution from the bulk viscosity ξ (Subsec. 4.2.1). Hence, now, for viscous ΛCDM case ($v\Lambda CDM$),

$$F(z)_{v\Lambda CDM} = \frac{(1+z)^{5/3}}{D_{L_v}} e^{-\frac{\gamma}{2(1+z)^2} D_{L_v}} . \tag{4.32}$$

where D_{L_v} is the luminosity distance in the presence of viscosity, i.e., it is calculated using $E(z)_{v\Lambda CDM}$. For non viscous ΛCDM case,

$$F(z)_{\Lambda CDM} = \frac{(1+z)^{5/3}}{D_{L_*}} \tag{4.33}$$

where D_{L_*} is the source luminosity distance in the absence of viscosity, i.e., it is calculated using $E(z)_{\Lambda CDM}$.

The value of the shear viscosity parameter η has been estimated in earlier works to lie within the range $\sim 10^6$ Pa sec and $\sim 10^9$ Pa sec [113, 114, 145]. Gravitational wave observation data from LIGO has been used to put constraints on the value of η [113]. Ref. [145] used the relativistic Boltzmann equation to examine the theory of viscosities at the time of neutrino decoupling. The analysis of [145] to calculate the present-day value of η was subsequently employed in [114], to relate the value of η at the time of neutrino decoupling with the present value using a scaling relation, leading to the value of 10^8 Pa sec. Our present analysis uses the above value of 10^8 Pa sec as the most favored one.

In (Fig. 4.4), we plot the overall redshift-dependent part, $F(z)$ (both $F(z)_{v\Lambda CDM}$ & $F(z)_{\Lambda CDM}$), given in (Eq. 4.32 and Eq. 4.33) with respect to redshift z, for the range of values of η between $\sim 10^6$ Pa sec and $\sim 10^9$ Pa sec. The plots for viscous cases in (Fig. 4.4) have contributions from both bulk viscosity ξ (through D_{L_v}) and shear viscosity η. It was argued in Ref. [113] that since ξ only couples to scalar perturbations, it doesn't play a role in the attenuation of GWs, and only η affects the GW amplitude. However, from our analysis, it is clear that both ξ and η affect the GW amplitude, with the role of the former entering through the modified background dynamics due to bulk viscosity.

The expressions given in (Eq. 4.32 and Eq. 4.33) are valid for a space with homogeneous mass distribution. To examine the variation of the redshift-dependent part of GW amplitude for our model, we have to modify the expressions accordingly. For our backreaction model, the relation $D_L = (1+z)^2 D_A$ is valid too, but in this case D_A is calculated using the covariant scheme (Eq. 2.25, Eq. 2.26). Our model represents a space with an inhomogeneous mass distribution, where there are two types of regions, viz., over-dense and under-dense, and viscosity is only associated with the over-dense region, as the under-dense region is assumed to be empty.

Hence, in the exponential term of the $F(z)$ in (Eq. 4.29), $e^{-\frac{\gamma}{2(1+z)^2}D_L}$, for our model, D_{L_o} would replace D_L, where D_{L_o} is the luminosity distance traversed by the GW through the over-dense region only. So, the exponential term of the $F(z)$ in (Eq. 4.29) for our model is now given by $e^{-\frac{\gamma}{2(1+z)^2}D_{L_o}}$. In the ΛCDM model, incorporating viscosity results in an attenuation factor with D_L in the exponential factor, where D_L is the total luminosity distance traversed by the GW. Viscosity is not distributed through the entire path of the GW but is concentrated only in some regions. Using D_L in the ΛCDM model results in a larger deviation between the attenuated and unattenuated cases in the ΛCDM model, compared to our model.

An important consideration for the propagation of EM waves for a model like ours (inhomogeneous 2-domain model) is that the ratio of distances traveled by EM waves through the two regions is equal to the ratio of proper volumes of the two regions [35]. It is clear that this also holds for GWs. This condition gives,

$$\frac{D_{L_o}}{D_{L_u}} = \left(\frac{a_o}{a_u}\right)^3 , \tag{4.34}$$

where D_{L_o} and D_{L_u} are the luminosity distances traversed by the GW through the over-dense and under-dense regions, respectively. If the total luminosity distance traveled by the GW in our model is $D_{L_{v2d}}$ (v2d stands for viscous 2-domain inhomogeneous model, this $D_{L_{v2d}}$ is calculated for the viscous case of our model (subsubsection 4.2.2.2) using D_A calculated from the covariant scheme (Eq. 2.25, Eq. 2.26)), then $D_{L_{v2d}} = D_{L_o} + D_{L_u}$, which gives,

$$D_{L_o}\left(1 + \frac{D_{L_u}}{D_{L_o}}\right) = D_{L_o}\left(1 + \left(\frac{a_u}{a_o}\right)^3\right) = D_{L_{v2d}} ,$$

or,

$$D_{L_o} = \frac{D_{L_{v2d}}}{\left(1 + \left(\frac{a_u}{a_o}\right)^3\right)} . \tag{4.35}$$

Therefore, the exponential term in the total redshift-dependent part of the attenuated GW amplitude for our model now becomes,

$$\mathcal{E} = e^{-\frac{\gamma}{2(1+z)^2}\frac{D_{L_{v2d}}}{\left(1+\left(\frac{a_u}{a_o}\right)^3\right)}}, \tag{4.36}$$

and the total redshift-dependent part of the attenuated GW amplitude for our viscous model is given by,

$$F(z)_{v2d} = \frac{(1+z)^{5/3}}{D_{L_{v2d}}}\mathcal{E} = \frac{(1+z)^{5/3}}{D_{L_{v2d}}} e^{-\frac{\gamma}{2(1+z)^2}\frac{D_{L_{v2d}}}{\left(1+\left(\frac{a_u}{a_o}\right)^3\right)}} . \tag{4.37}$$

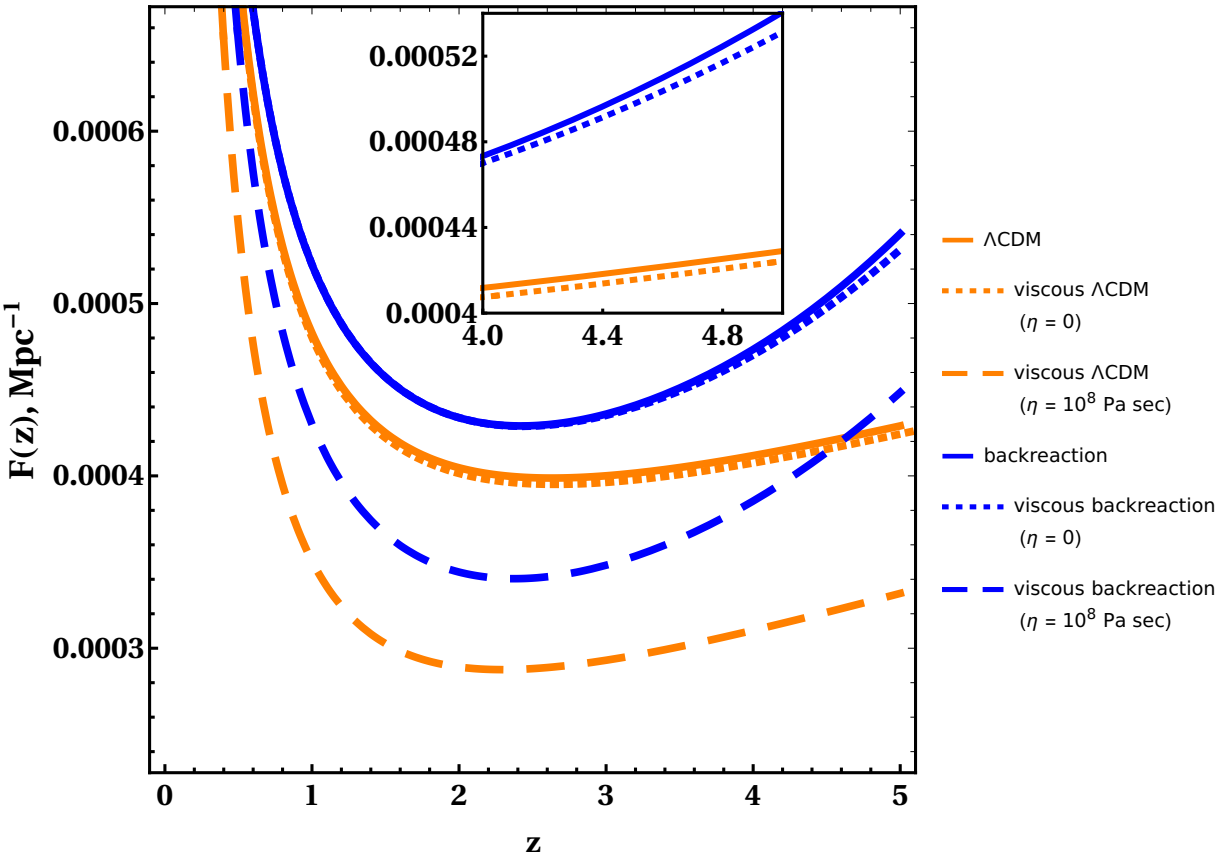

Figure 4.5: Plot of $F(z)$ vs z for ΛCDM model and for our model for $(\alpha,\beta) = (0.67,1)$. The solid curves are for non-viscous cases. The dotted curves are for those cases in which only ξ has been included. The dashed curves have contributions from both ξ and η. The value of ξ used is 10^6 Pa sec. Parameters used for ΛCDM are $\Omega_m = 0.31$, $\Omega_\Lambda = 0.69$. The inset shows the magnified portion of the solid curve and the dotted curve for the two models to illustrate the difference between these two curves.

The redshift-dependent part of the GW amplitude for our non-viscous model (subsubsection 4.2.2.1) is given by,

$$F(z,\xi=0,\eta=0)_{2d} = \frac{(1+z)^{5/3}}{D_{L_{*2d}}}\,. \tag{4.38}$$

where 2d stands for non-viscous 2-domain inhomogeneous model and $D_{L_{*2d}}$ is the source luminosity distance for the case of our non-viscous 2-domain inhomogeneous model. Therefore, for our model, the deviation of the redshift-dependent part of GW amplitude due to viscous attenuation can be written as,

$$F(z,\xi=0,\eta=0)_{2d} - F(z)_{v2d} = (1+z)^{5/3}\left\{\frac{1}{D_{L_{2d}}} - \frac{e^{-\frac{\gamma}{2(1+z)^2}\frac{D_{L_{v2d}}}{\left(1+\left(\frac{a_u}{a_o}\right)^3\right)}}}{D_{L_{v2d}}}\right\}. \tag{4.39}$$

To summarize, the redshift-dependent part of GW for a homogeneous and non-viscous spacetime (ΛCDM model) is given by (Eq. 4.33). Now, if we introduce

matter distribution inhomogeneities, then $F(z)$ gets modified due to modification of the redshift-distance relations, and is now given by (Eq. 4.38). It can be seen that,

$$F(z,\xi=0,\eta=0)_{2d} = F(z)_{\Lambda CDM} \times \frac{D_{L_*}}{D_{L_{*2d}}} \tag{4.40}$$

Therefore, the effect of inclusion of matter distribution inhomogeneities on the redshift-dependent part of the GW amplitude is equivalent to multiplication by the factor $\frac{D_{L_*}}{D_{L_{*2d}}}$.

On further introduction of viscosity in the analysis, GW in our backreaction model gets attenuated by the attenuation factor (using (Eq. 4.36)),

$$\mathfrak{A} = \frac{D_{L_{*2d}}}{D_{L_{v2d}}}\mathcal{E} = \frac{D_{L_{*2d}}}{D_{L_{v2d}}} e^{-\frac{\gamma}{2(1+z)^2}\frac{D_{L_{v2d}}}{\left(1+\left(\frac{a_u}{a_o}\right)^3\right)}} \tag{4.41}$$

where $D_{L_{*2d}}$ is the luminosity distance for the case of our non-viscous 2-domain inhomogeneous model, calculated using the covariant scheme.

Thus, the total redshift dependent part of GW in the presence of viscous inhomogeneities becomes (using (Eq. 4.37),(Eq. 4.38), (Eq. 4.40) & (Eq. 4.41)),

$$\begin{aligned} F(z)_{v2d} &= F(z)_{\Lambda CDM} \times \frac{D_{L_*}}{D_{L_{*2d}}} \times \mathfrak{A} = F(z,\xi=0,\eta=0)_{2d} \times \mathfrak{A} \\ &= \frac{(1+z)^{5/3}}{D_{L_{*2d}}} \times \frac{D_{L_{*2d}}}{D_{L_{v2d}}}\mathcal{E} = \frac{(1+z)^{5/3}}{D_{L_{v2d}}}\mathcal{E} = \frac{(1+z)^{5/3}}{D_{L_{v2d}}} e^{-\frac{\gamma}{2(1+z)^2}\frac{D_{L_{v2d}}}{\left(1+\left(\frac{a_u}{a_o}\right)^3\right)}} \end{aligned} \tag{4.42}$$

In (Fig. 4.5), we plot the redshift-dependent part of the GW amplitude, $F(z)$ vs z for the ΛCDM model and for our model for model parameter $(\alpha,\beta) = (0.67, 1)$. There are 3 curves for each model. The solid curve represents the non-viscous case; the dotted curve represents the case in which only the bulk viscosity has been included in the analysis, and the dashed curve represents the case with both bulk viscosity and shear viscosity in the analysis. As can be seen from (Fig. 4.5), even if we just consider bulk viscosity, there is also a deviation of the redshift-dependent part of the GW amplitude (dotted curve) with respect to the non-viscous case (solid curve). This is because the redshift-dependent part of the GW amplitude consists of D_L and ξ, which affects this D_L via the quantity $E(z)$ (Eq. 4.31). On further inclusion of η in the analysis, the redshift-dependent part of the GW amplitude gets attenuated (dashed curve). In this case, $F(z)$ for viscous ΛCDM model is given by (Eq. 4.32), for non viscous ΛCDM model by (Eq. 4.33), for our non viscous model with inhomogeneities by (Eq. 4.38) and for our viscous model with inhomogeneities, it is given by (Eq. 4.37).

In (Fig. 4.6), we plot the redshift-dependent part of the GW amplitude, $F(z)$ vs z for the ΛCDM model and for our model for different combinations of model

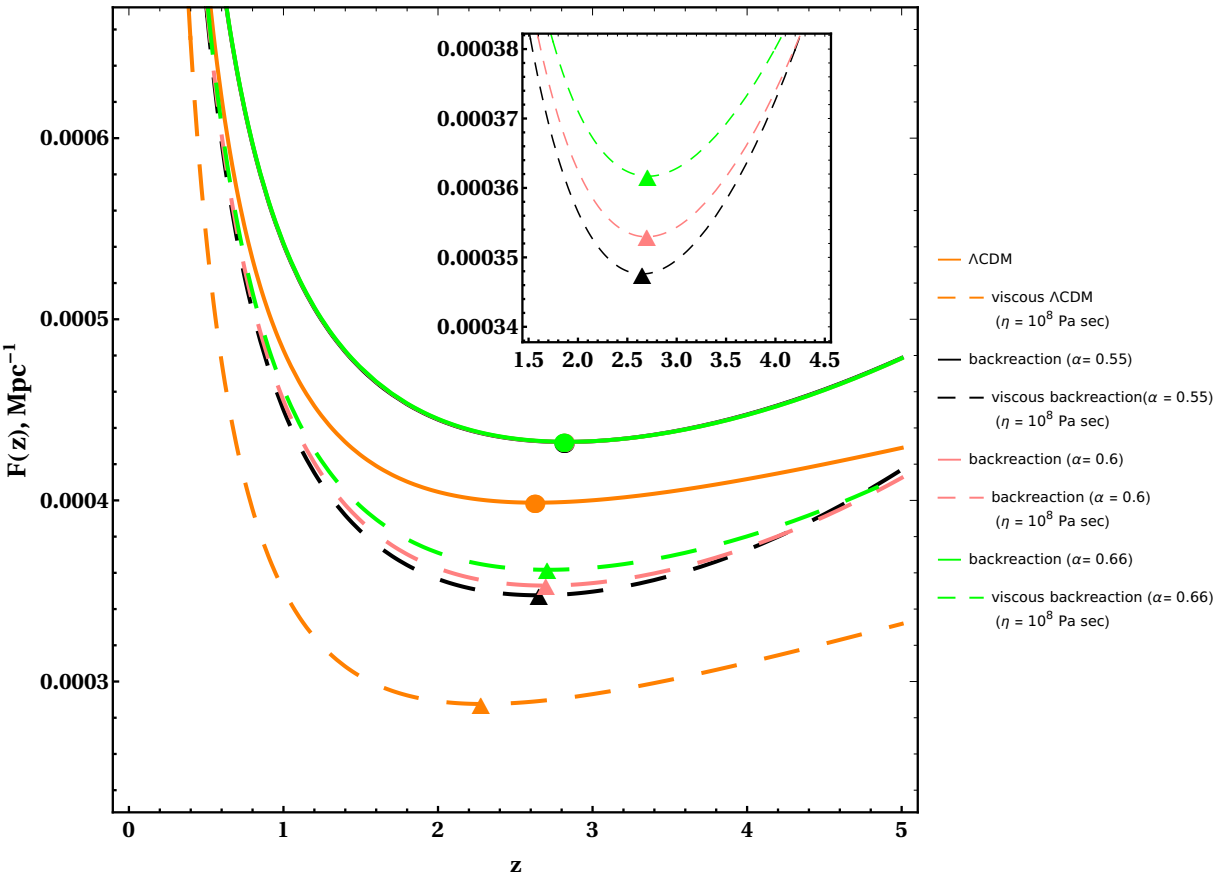

Figure 4.6: Plot of $F(z)$ vs z for ΛCDM model and for our model for different combinations of (α,β) while keeping $\beta = 0.8$ as constant. The solid curves are for non-viscous cases. The viscous cases represented by dashed curves have contributions from both ξ and η. The value of ξ used is 10^6 Pa sec. Parameters used for ΛCDM are $\Omega_m = 0.31$, $\Omega_\Lambda = 0.69$. Circular points represent the minima for the solid (non-viscous)curves, while triangular points represent the minima positions for the dashed (viscous) curves. The inset shows the magnified portion of the three dashed curves of our backreaction model to illustrate the difference between these curves.

parameters (α,β). Here, we have kept β constant = 0.8, and we vary the value of α. The solid curves represent the non-viscous cases, and the dashed curves represent the viscous case with contributions from both ξ and η. The redshift-dependent part of the GW amplitude, i.e., the quantity $(1+z)^{5/3}/D_L$ in the case of ΛCDM, has a minimum at $z_{min} \simeq 2.63$ [146]. In (Fig. 4.6) we display the minima points of the various curves. Circular points represent the minima for the solid (non-viscous) curves, while triangular points represent the minima positions for the dashed (viscous) curves. We observe that the minima for the vΛCDM curve deviate significantly from the ΛCDM case. For our backreaction model (both viscous and non-viscous), minima points deviate significantly from the ΛCDM case. It can be seen from the figure that for the non-viscous cases of our model, all three plot lines and their minima points for different values of α overlap. $F(z)$ for the non-viscous cases is given by (Eq. 4.38). Since the value of $(1+z)^{5/3}$ is the same for all (α,β), the only quantity varying with changing (α,β) is D_L. The volume fraction of the overdense region at the present time is taken as 0.09, and the range of variation of α, which governs the evolution of the overdense region, is from $0.5-0.67$. Since the overdense volume fraction is so small, the variation of α over this small range (0.5 - 0.67) doesn't have much effect, and hence, the plot lines for the non-viscous cases overlap in (Fig. 4.6).

From (Fig. 4.6), it can be seen that there is substantial attenuation of the redshift-dependent part of the GW amplitude due to viscosity. $F(z)$ for viscous cases is given by (Eq. 4.37). As compared to the non-viscous case (Eq. 4.38), there are now additional terms. From (Eq. 4.12) and (Eq. 4.14), the scale factor of the overdense region is given by,

$$a_o = \left(\frac{t}{t_0}\right)^{\alpha} = \left(\frac{t}{13.8}\right)^{\alpha} \tag{4.43}$$

where t_0 = 13.8 Gyr. For a given value of t ($t < t_0$), as we increase α, a_o decreases. It can be seen in (Fig. 4.6), as we increase the value of α keeping β constant, the redshift-dependent part of GW, $F(z)$, for the viscous case, gets smaller in magnitude. Physically, this can be explained from the fact that from (Eq. 2.9) for an overdense region, a_o can be defined as

$$a_o(t) := \left(\frac{V_o(t)}{V_{o_0}}\right)^{1/3} , \tag{4.44}$$

where V_{o_0} is the volume of the overdense region at the present time, which we have fixed for all values of (α,β) to be 0.09 by fraction of the total volume. As a_o decreases, the volume of the overdense domain decreases. Hence, the distance traveled by the GW through the overdense region will be less, leading to less attenuation suffered by the GW. GW, which travels the largest distance through

the overdense region, will suffer the most attenuation. This distance traveled by the GW is directly proportional to the scale factor of the overdense region. In (Fig. 4.6), the green dashed curve has the largest value of α (hence the smallest value of a_o), corresponding to the largest amplitude among the viscous cases since it has suffered the least attenuation. In contrast, the black dashed curve has the smallest value of α (hence the largest value of a_o), corresponding to the smallest amplitude among the viscous cases since it has suffered the most attenuation. The above feature is not observed for the non-viscous cases (solid curves) as the overdense region is non-viscous; hence, there is no viscous attenuation.

4.5 Conclusions

In this chapter, we have studied the propagation of GWs from compact binary sources through a viscous inhomogeneous Universe governed by a model based on the averaging procedure for scalars in Buchert's backreaction framework [25, 27]. Dynamics under this model lead to a modification of the redshift-versus-distance relation from that for the ΛCDM model. The extent of variation depends on the combination of the model parameters. In the present work, we have considered viscosity to be present in the matter content within the overdense regions of inhomogeneous spacetime described by our model, which causes the attenuation of the GW amplitude when the GW passes through those regions of spacetime. We have incorporated the viscous attenuation of GW amplitude within our model of inhomogeneous spacetime and have derived an expression for the resultant redshift-dependent part of the GW amplitude.

In the ΛCDM model, incorporating viscosity results in a GW attenuation factor with D_L in the exponent, where D_L is the total luminosity distance traversed by the GW. It is worth noting that in the real Universe, viscosity resulting from dark matter interactions is not distributed uniformly through the entire path of the GW but is concentrated only in some regions. Therefore, in our model, we have used D_{L_o} (luminosity distance of the overdense region) instead of D_L. Using D_L results in a more significant deviation between the attenuated and unattenuated cases for the ΛCDM model, compared to using D_{L_o} for our model. It has been argued earlier [113] that since bulk viscosity couples only to scalar perturbations, it doesn't play a role in the attenuation of GWs. However, as shown here, bulk viscosity indirectly impacts the GW amplitude through its effect on the luminosity distance. Moreover, the effect of shear viscosity on GW attenuation is clearly demonstrated in the backreaction model due to inhomogeneities.

Our analysis demonstrates a substantial deviation in the redshift-dependent part of the GW amplitude due to the inclusion of viscous attenuation, compared to the case when viscosity is considered negligible or absent within the model of

inhomogeneous spacetime. We have further shown that the rate of expansion of the overdense region (characterized by the parameter α, which governs the time evolution of the scale factor of the overdense region) plays a vital role in the magnitude of attenuation. It may be emphasized that consideration of the effect of viscosity on GW observables for compact binary sources is significant in the context of local inhomogeneities in the Universe.

To summarize, we would again like to highlight the importance of considering realistic background effects in the study of GW propagation, since using incorrect background dynamics for analyzing GW data from detectors could result in incorrect inferences about GW sources. Towards this end, we have taken into account these two aspects of inhomogeneities and attenuation of GW due to viscosity together in our present work. Our analysis leads to several interesting features in the red-shift dependent part of the gravitational wave amplitude. Additionally, the role of bulk viscosity is a new feature that is also brought out in the form of its indirect contribution towards GW attenuation through modification of the background dynamics. Our analysis paves the way for obtaining more precise estimations of GW observables and bounds on the viscosity parameters of dark matter in future work involving more realistic backreaction models and data-analysis techniques in GW astronomy.

Chapter 5

Future deceleration due to backreaction in a Universe with multiple inhomogeneous domains

5.1 Introduction

The concordance model of cosmology, *viz.*, the ΛCDM model, is based on the Cosmological Principle, which states that the Universe is homogeneous and isotropic and interprets the Universe as an FLRW spacetime. Cosmological observations like Sloan Digital Sky Survey (SDSS) [8] indicate that matter inhomogeneities exist at the scales of super-clusters of galaxies. Studies analyzing large-scale fluctuations in the luminous red galaxy samples [9] have found substantial (more than three sigmas) divergence from the ΛCDM mock catalogues on samples as large as $500h^{-1}Mpc$. Thus, though the Universe is homogeneous and isotropic at extremely large length scales, the Cosmological Principle doesn't hold at smaller scales, and matter inhomogeneities may have significant consequences up to a length scale of $500h^{-1}Mpc$.

We have used Buchert's averaging procedure outlined in detail in (Sec. 2.1) in order to study the effect of inhomogeneities on the Universe's evolution.

Although the overall significance of cosmic backreaction on the overall evolution of the real Universe is still debated [31], it is at least possible, in principle, for the backreaction to influence the evolution of the universe [39]. In this work, we employ Buchert's backreaction formalism to examine the fate of the currently accelerating phase of the Universe in the presence of observed matter inhomogeneities at considerably large scales.

Observational evidence establishes the Universe's current acceleration [147–150]. However, the ΛCDM model is afflicted by certain observational discrepancies, such as the Hubble tension [6, 7] which has attracted a lot of attention recently. The Hubble tension arises from a discrepancy in the inferred value

of the Hubble parameter from local measurements compared to that from early Universe physics. It is possible for the backreaction-induced curvature to explain the larger values of the Hubble parameter obtained locally [134]. The ΛCDM Universe may end in a future big freeze, or even in a big rip [151–153] in the presence of phantom dark energy ($\omega_{de} < -1$). It has been shown that the Buchert formalism in dust universes predicts the dwindling of the present acceleration [154], and the extrapolation of Buchert's procedure in the context of a two-scale void-wall toy model of the Universe leads to the possibility of avoiding the future big freeze or a possible future big rip in a phantom dark energy model [44–46].

The motivation for the present study is to re-examine the late-time evolution of the presently accelerating Universe by employing the Buchert backreaction formalism in the context of a more realistic model mimicking our actual Universe with observed inhomogeneities extending up to considerably large scales. In this work, we consider a multiple subregion model of the spacetime with each subregion having a distinct set of parameters characterizing its evolution. We apply the Buchert averaging procedure against the backdrop of such a model in order to investigate the global evolution during the present era, extended to the future. It is important to analyze the future evolution ensuing from such a study, as a transition from present acceleration to deceleration in the near future may have immediate consequences for our present Universe. We confront this scenario against observational results by performing Markov Chain Monte Carlo analysis using the Union2.1 supernova Ia data [155] to determine our model parameters' best fit and optimum values.

This chapter is organized as follows. In (Sec. 5.2), we introduce our model of inhomogeneities in multiple subregions. In (Sec. 5.3), we present our multi-domain model's theoretical analysis leading to the Universe's predicted late-time evolution. In (Sec. 5.4) we use the Union2.1 supernova Ia data to constrain our model parameters. We summarize our main results in (Sec. 5.5).

5.2 Our multiple subregions model

Several recent analyses have been carried out within the Buchert formalism with one under-dense and one over-dense subdomain [36, 42, 44–47]. The assumption of just two different density domains represents an oversimplification in the context of the real Universe, as the actual density profile varies across a spectrum from regions of very low density to those of high density. Hence, to construct a more realistic cosmological model, one needs to consider a larger number of sub-domains with distinct evolution profiles. Since some earlier studies based on two-domain models have predicted a future deceleration of the universe [44–46], it is interesting to study the future evolution of the universe in the context of a more

realistic model having a large number of subdomains with distinct parameters.

In the context of the backreaction framework employed in this work, we consider a model of the Universe in which the domain $\mathcal{D}$ of interest comprises multiple subregions. The multiple subregions in our model can be categorized into two types of regions - (i) overdense regions which are closed dust-only FLRW regions with positive curvature and a deceleration parameter $q_o = -\ddot{a}_o/a_o H_o^2 > 0.5$, and (ii) underdense regions which are flat (zero intrinsic curvature) FLRW regions and having smaller density (as compared to the overdense regions). So, there are in total n subregions in our model, i of them are overdense and $(n-i)$ of them are underdense.

The scale factor and time of the i^{th} overdense region evolve with development angle ϕ of the overdense region as [46, 136],

$$a_{o_i} = \frac{q_{o_i}}{2q_{o_i}-1}(1-\cos\phi), \tag{5.1}$$

$$t_i = \frac{q_{o_i}}{2q_{o_i}-1}(\phi-\sin\phi), \tag{5.2}$$

where q_{o_i} is the deceleration parameter of the i^{th} overdense region. The scale factor of the i^{th} under-dense region is taken to evolve as a function of time t given by

$$a_{u_i} = c_{u_i} t^{\beta_i} \tag{5.3}$$

In the above expression, c_{u_i} and β_i are constant, which determines the time evolution of the i^{th} under-dense subregion. β_i varies from 2/3 to 1 to denote any behaviour ranging from a matter-dominated region ($\beta_i = 2/3$) up to an accelerating region ($\beta_i > 1$).

Now, applying (Eq. 5.1 - Eq. 5.3) in (Eq. 2.24), the expression of the global acceleration takes the form

$$\frac{\ddot{a}_{\mathcal{D}}}{a_{\mathcal{D}}} = \left(\sum_i -\lambda_{o_i} q_{o_i} H_{o_i}^2\right) + \left(\sum_j \lambda_{u_j} \frac{\beta(\beta-1)}{t^2}\right) + \left(\sum_k \sum_l \lambda_k \lambda_l (H_l - H_k)^2\right). \tag{5.4}$$

Here λ_{o_i} is the volume fraction of the i^{th} overdense region, λ_{u_j} is the volume fraction of the j^{th} overdense region, H_{o_i} is the Hubble parameter of the i^{th} overdense region, λ is the set of all λ_{o_i} and λ_{u_i} and H is the set of all H_{o_i} and H_{u_i}. The total volume fraction of all the under-dense regions, i.e. $\sum_i \lambda_{u_i}$ is given by λ_u. Similarly, λ_o is the total volume fraction of all the over-dense regions. Clearly, $\lambda_o + \lambda_u = 1$.

The volume fraction of the i^{th} under-dense subregion can be written as,

$$\begin{aligned}\lambda_{u_i} &= \frac{V_{u_i}}{V_{\mathcal{D}}} = \frac{a_{u_i}^3 V_{u_i,0}}{a_{\mathcal{D}}^3 V_{\mathcal{D},0}} = \lambda_{u_i,0}\frac{a_{u_i}^3}{a_{\mathcal{D}}^3} \\ &= \lambda_{u_i,0}\frac{c_{u_i}^3 t^{3\beta_i}}{a_{\mathcal{D}}^3} = \lambda_{u_i,0}\left(\frac{t}{t_0}\right)^{3\beta_i}\left(\frac{a_{\mathcal{D},0}}{a_{\mathcal{D}}}\right)^3, \end{aligned} \tag{5.5}$$

where t_0 is a reference time generally taken to be present time, $V_{u_i,0}$ is the volume of the i^{th} under-dense subregion at the present time, $\lambda_{u_i,0}$ is the volume fraction of the i^{th} under-dense subregion at the present time, $V_{\mathcal{D},0}$ is the present time value of the volume and $a_{\mathcal{D},0}$ is the present time value of the scale factor of the domain D of interest. The present time value of (λ_o, λ_u) is given by $(\lambda_{o,0}, \lambda_{u,0})$ which may be taken to be $(0.09, 0.91)$ [27]. In the present analysis, we assume the distribution of $\lambda_{u_i,0}$ across the i underdense subregions to follow a Gaussian profile within the allowed range of β_i, given by

$$\lambda_{u_i,0} = \frac{N_u}{\sigma_u\sqrt{2\pi}} e^{-(\beta_i-\mu_u)^2/2\sigma_u^2}, \tag{5.6}$$

where N_u is a normalization constant, such that, $\lambda_{u,0}$ which is the total volume fraction at the present time of all the under-dense regions summed over, $\sum_i \lambda_{u_i,0} = 0.91$, μ_u is the mean value of β_i and σ_u is the standard deviation of β_i. The present time volume fractions of the over-dense regions are considered to follow Gaussian distributions within the allowed range of q_o, given by

$$\lambda_{o_i,0} = \frac{N_o}{\sigma_o\sqrt{2\pi}} e^{-(q_{o_i}-\mu_o)^2/2\sigma_o^2}. \tag{5.7}$$

where N_o is a normalization constant, such that, $\lambda_{o,0}$ which is the total volume fraction at the present time of all the over-dense regions summed over, $\sum_i \lambda_{o_i,0} = 0.09$, μ_o is the mean value of q_{o_i} and σ_o is the standard deviation of q_{o_i}. As mentioned earlier, q_{o_i} ranges from 0.51 to 1. λ_{o_i} which is the volume fraction of the i^{th} over-dense subregion at a time t is related to $\lambda_{o_i,0}$ by the relation

$$\lambda_{o_i} = \lambda_{o_i,0}\left(\frac{1-\sum_i \lambda_{u_i}}{1-\sum_i \lambda_{u_i,0}}\right), \tag{5.8}$$

5.3 Late time evolution of the Universe

In our analysis, there are a total of n subregions. In (Eq. 5.7), for a given value of μ_o and σ_o, q_{o_i} can take i number of values in the allowed range, where i is the no. of overdense subregions. For each value of q_{o_i}, there is a corresponding value of $\lambda_{o_i,0}$, such that $\sum_i \lambda_{o_i,0} = 0.09$, and (Eq. 5.8) gives us λ_{o_i} for each i^{th} overdense subregion. (Eq. 5.1) and (Eq. 5.2) give us the scale factor a_{o_i} and time t for each

i^{th} overdense subregion, corresponding to the value of q_{o_i}, and from these, H_{o_i} can be calculated. Similarly, in the case of underdense subregions, in (Eq. 5.6), for a given value of μ_u and σ_u, β_i can take i number of values in the allowed range, where i is the no. of underdense subregions. For each value of β_i, there is a corresponding value of $\lambda_{u_i,0}$, such that $\sum_i \lambda_{u_i,0} = 0.91$. Once we have $\lambda_{u_i,0}$, we can use (Eq. 5.5) to get λ_{u_i}. For each i^{th} underdense subregion, (Eq. 5.3) gives us the value of scale factor a_{u_i} for the corresponding value of β_i, and from this, H_{u_i} can be calculated. We can then use (Eq. 2.24) to calculate the scale factor a_D (as a function of time) of the domain of interest D and from it the Hubble parameter H_D of D.

For our multiple subregions model, (Eq. 2.22) effectively becomes,

$$Q_D = \sum_i Q_{o_i} + \sum_j Q_{u_j} + 3 \sum_{l \neq m} \lambda_l \lambda_m (H_l - H_m)^2 \,, \tag{5.9}$$

where λ is the set of all λ_{o_i} and λ_{u_i} and H is the set of all H_{o_i} and H_{u_i}. Since (Eq. 2.16) couples the time evolution of the backreaction term Q_D with the time evolution of the averaged 3-Ricci scalar curvature, it is also applicable for our subregions. Thus, the time evolution of Q_{o_i} and Q_{u_j} is coupled to the evolution of the averaged 3-Ricci scalar curvature of the respective subregions. However, one can choose the curvatures of the individual sub-regions in such a way that the Q_{o_i} and Q_{u_j} terms for these sub-regions become effectively zero [27, 156]. This is done by taking the curvature of our underdense region to be zero, i.e., our underdense region is flat. On the other hand, we have assumed our overdense region to have a Friedmann-like a_u^{-2} constant curvature term. These assumptions along with (Eq. 2.16) results in, $Q_{o_i} = 0$ and $Q_{u_j} = 0$. The stipulation to FLRW is an approximate assumption governing our present model (in the more general case, the sub-domains may not necessarily be FLRW regions). As seen from (Eq. 5.9), the global backreaction is the sum of three terms. In our approach, we have assumed the underdense region to have zero curvature, and the overdense region to have constant curvature, thereby making the first two terms in (Eq. 5.9) vanish. Hence, in this case, the global backreaction is governed by only the interplay of the sub-domain Hubble evolutions and volume fractions (third term of (Eq. 5.9). On the other hand, if the sub-domains are endowed with dynamical curvature, there could be other intricate effects arising through backreaction.

In our calculations, we consider one hundred under-dense and one hundred over-dense sub-domains. These sub-domains are characterized by the respective volume fractions, λ_{o_i} and λ_{u_i}, distributed using a Gaussian profile among these sub-domains (Eq. 5.6 and Eq. 5.7). μ_o and σ_o are the mean and standard deviation, respectively, for the Gaussian profile of overdense regions. In a Gaussian distribution, the mean is also the most frequent observation. Therefore, this

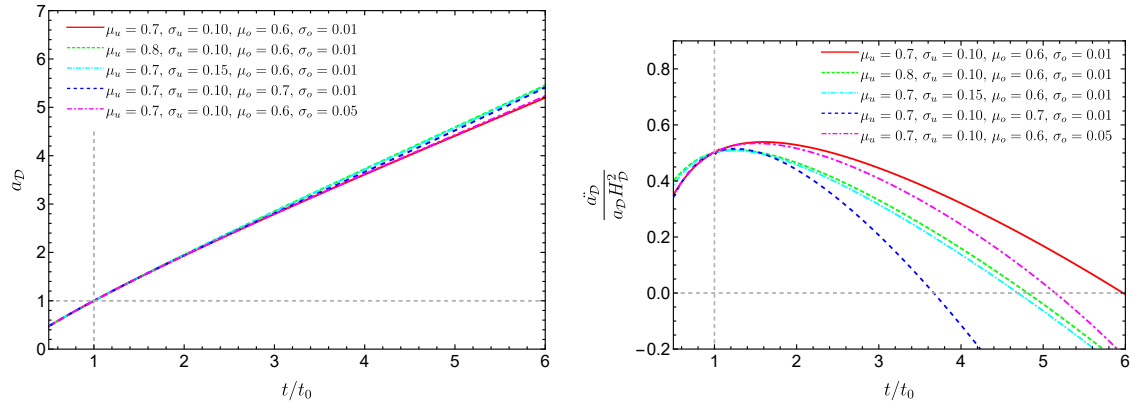

(a) (b)

Figure 5.1: Evolution of (a) the global scale factor $a_{\mathcal{D}}$, (b) the global acceleration parameter $\frac{\ddot{a_{\mathcal{D}}}}{a_{\mathcal{D}}H_{\mathcal{D}}^2}$, for different sets of model parameters namely, μ_o, σ_o, μ_u and σ_o.

means that out of the 100 overdense sub-domains, μ_o is the most frequent value of q_{o_i}. σ_o is the distribution's standard deviation, which governs the distribution's width about the mean value. Similarly, μ_u and σ_u are the mean and standard deviation for the underdense regions' Gaussian profile. Our underdense regions are characterized by parameters β_i, and these vary from $2/3 < \beta_i < 1$. This range for β_i has been taken to ensure a wide range of underdense subregions is present in our model to mimic a variety of underdense regions that may be present in the Universe. μ_u is the most frequent value of β_i among the 100 underdense regions. Here, σ_u governs the width of the distribution about a given μ_u.

In (Fig. 5.1)(a) and (Fig. 5.1)(b), the scale factor $a_{\mathcal{D}}$ and the acceleration of the Universe $\frac{\ddot{a_{\mathcal{D}}}}{a_{\mathcal{D}}H_{\mathcal{D}}^2}$ are plotted respectively, for different sets of model parameters *viz.*, μ_o, σ_o, μ_u and σ_o. (Fig. 5.1)(a) is plotted by fixing the present value (i.e., value at $t = t_0$) of the scale factor $a_{\mathcal{D}}$ to be 1. (Fig. 5.1)(b) is plotted using the present value (i.e., value at $t = t_0$) of global acceleration parameter $\frac{\ddot{a_{\mathcal{D}}}}{a_{\mathcal{D}}H_{\mathcal{D}}^2}$ to be 0.55 which is obtained using the values of cosmological parameters from Planck 2018 results [157]. From (Fig. 5.1)(b) it can be seen that the acceleration parameter begins to fall off beyond the present era ($t = t_0$), and the Universe transits to a decelerating phase ($\frac{\ddot{a_{\mathcal{D}}}}{a_{\mathcal{D}}H_{\mathcal{D}}^2} < 0$) at a subsequent time. This result is in agreement with observations made in [154], where, in the context of a dust Universe, it was shown that accelerated expansion from backreaction cannot go on forever. It may be note,d however, that the main focus of the work [154] is to understand whether backreaction could provide a viable means of the current acceleration of the Universe. On the other hand, the focus of our present work is to understand how the Universe evolves in the future, given that it is currently accelerating.

From our results, it can be seen that for higher values of the model parameters, namely, μ_o, σ_o, μ_u or σ_o, the acceleration parameter $\frac{\ddot{a_{\mathcal{D}}}}{a_{\mathcal{D}}H_{\mathcal{D}}^2}$ falls more rapidly with time in comparison to lower values of parameters. Such behaviour is observed

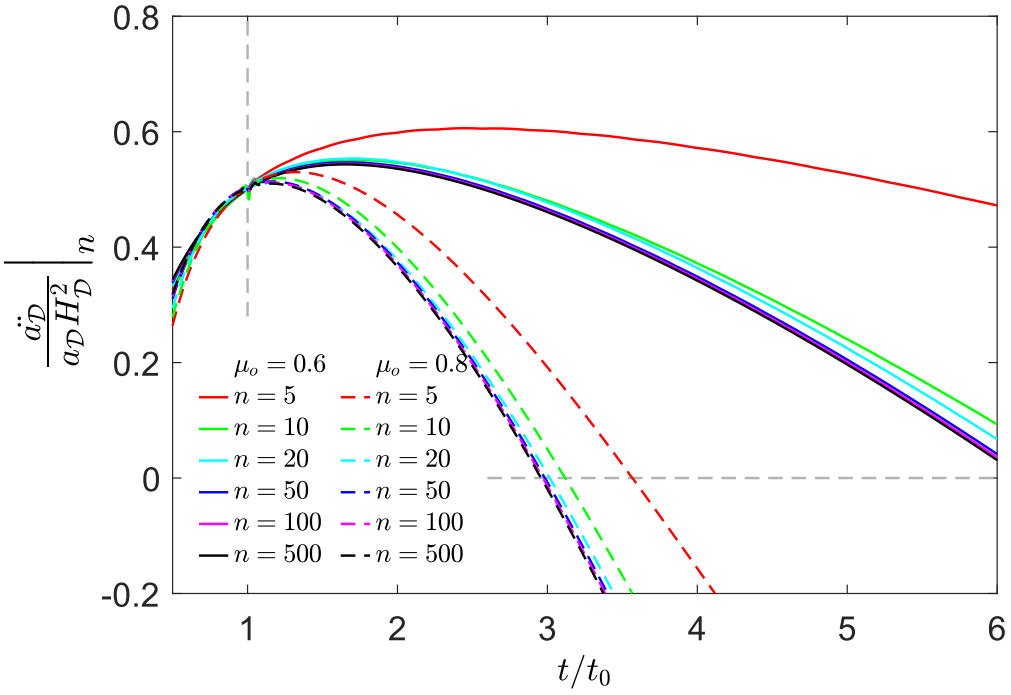

Figure 5.2: Variation of the evolution of global acceleration $\frac{\ddot{a_{\mathcal{D}}}}{a_{\mathcal{D}}H_{\mathcal{D}}^2}$ for different values of n with $\mu_o = 0.6$ (solid lines) and $\mu_o = 0.8$ (dashed lines). The other parameters are kept fixed at $\mu_u = 0.67$, $\sigma_u = 0.1$ and $\sigma_o = 0.01$

since the most frequent value of β_i and q_{o_i} in the respective distribution increases for higher values of μ (μ_u and μ_o). Therefore, there are now more underdense and overdense subdomains in the distribution with these higher values of β_i and q_{o_i}, respectively. Further, increasing the values of σ (σ_u and σ_o) results in the distribution of underdense and overdense sub-regions becoming wider around the mean values μ_u and μ_o respectively (see Eq. 5.6 and Eq. 5.7). As a consequence, the effect of subregions having higher values of β (for underdense regions) and q_o (for overdense regions) become prominent in the global dynamic of the Universe, which leads to rapid fall of the acceleration parameter $\frac{\ddot{a_{\mathcal{D}}}}{a_{\mathcal{D}}H_{\mathcal{D}}^2}$. Note further that higher values of β produce a larger acceleration in the early evolution (compare the green dashed line and the red solid line of (Fig. 5.1)). The green dashed line has a larger value of μ_u and hence, the most frequent value of β_i in the distribution is larger. However, the future acceleration falls off more rapidly due to such higher values of β.

In (Fig. 5.2), the evolution of the acceleration parameter $\left(i.e.\, \frac{\ddot{a_{\mathcal{D}}}}{a_{\mathcal{D}}H_{\mathcal{D}}^2}\right)$ is plotted for different values of n with $\mu_o = 0.6$ (solid lines) and $\mu_o = 0.8$ (dashed lines).

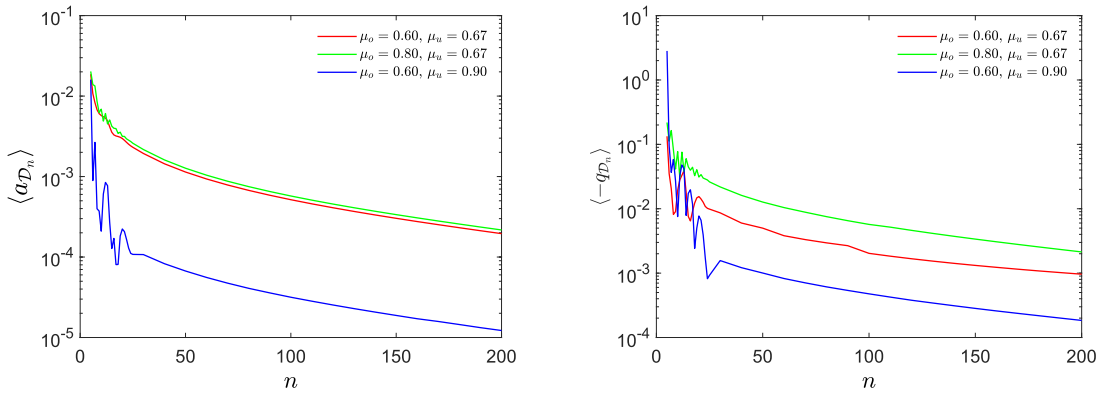

Figure 5.3: Variation of the time averaged (a) scale factor $\langle a_{\mathcal{D}_n} \rangle$ and (b) acceleration parameter $\langle -q_{\mathcal{D}_n} \rangle$ with n for different values of μ_u and μ_o, where the other two parameters are kept fixed at $\sigma_u = 0.1$ and $\sigma_o = 0.01$.

Here, other parameters are kept fixed at $\mu_u = 0.67$, $\sigma_u = 0.1$, and $\sigma_o = 0.01$. From this figure, it can be observed that the future acceleration falls off more rapidly with the increasing number of sub-regions. However, if one raises the number of sub-domains further, the evolution of the acceleration parameter tends toward a limiting profile depicted here for the case of $n = 500$.

For a deeper investigation into the variation of the global evolution versus the number of sub-domains, we introduce two parameters defined as,

$$\langle a_{\mathcal{D}_n} \rangle = \frac{1}{\sum i} \sum_i \left| \frac{a_{\mathcal{D}}|_{500} - a_{\mathcal{D}}|_n}{a_{\mathcal{D}}|_{500}} \right|_{t=t_i}, \tag{5.10}$$

$$\langle -q_{\mathcal{D}_n} \rangle = \frac{1}{\sum i} \sum_i \left| \left(\frac{\ddot{a_{\mathcal{D}}}}{a_{\mathcal{D}} H_{\mathcal{D}}^2} \Big|_{500} - \frac{\ddot{a_{\mathcal{D}}}}{a_{\mathcal{D}} H_{\mathcal{D}}^2} \Big|_n \right) \right|_{t=t_i}. \tag{5.11}$$

The terms $\langle a_{\mathcal{D}_n} \rangle$ and $\langle -q_{\mathcal{D}_n} \rangle$ denote the time-averaged variation of $a_{\mathcal{D}_n}$ and $\frac{\ddot{a_{\mathcal{D}}}}{a_{\mathcal{D}} H_{\mathcal{D}}^2}\Big|_n$ respectively, from the limiting case of $n = 500$. In this analysis, we split the entire time range (*i.e.* $0 \leq t/t_0 \leq 6$) into 1000 bins. In (Eq. 5.10) and (Eq. 5.11), i is the index number of such bins. The variation of $\langle a_{\mathcal{D}_n} \rangle$ and $\langle -q_{\mathcal{D}_n} \rangle$ with n are plotted in (Fig. 5.3)(a) and (Fig. 5.3)(b) respectively. In these two figures, the plots are for different chosen sets of μ_o and μ_u, while the other two parameters are kept at $\sigma_u = 0.1$ and $\sigma_o = 0.01$. It is clearly seen that for $n \geq 100$, the average fluctuation is less than ~ 0.01. For higher values of μ_u, the fluctuations reduce further for even smaller values of n. In view of the above results, we chose $n = 100$ for our remaining calculations.

In the present analysis, we essentially look into the late-time dynamics of the Universe. As in (Fig. 5.1)(b) and (Fig. 5.2), one can see that, although the Universe is expanding at the current epoch, the rate of acceleration $\left(\frac{\ddot{a_{\mathcal{D}}}}{a_{\mathcal{D}} H_{\mathcal{D}}^2} \right)$ will

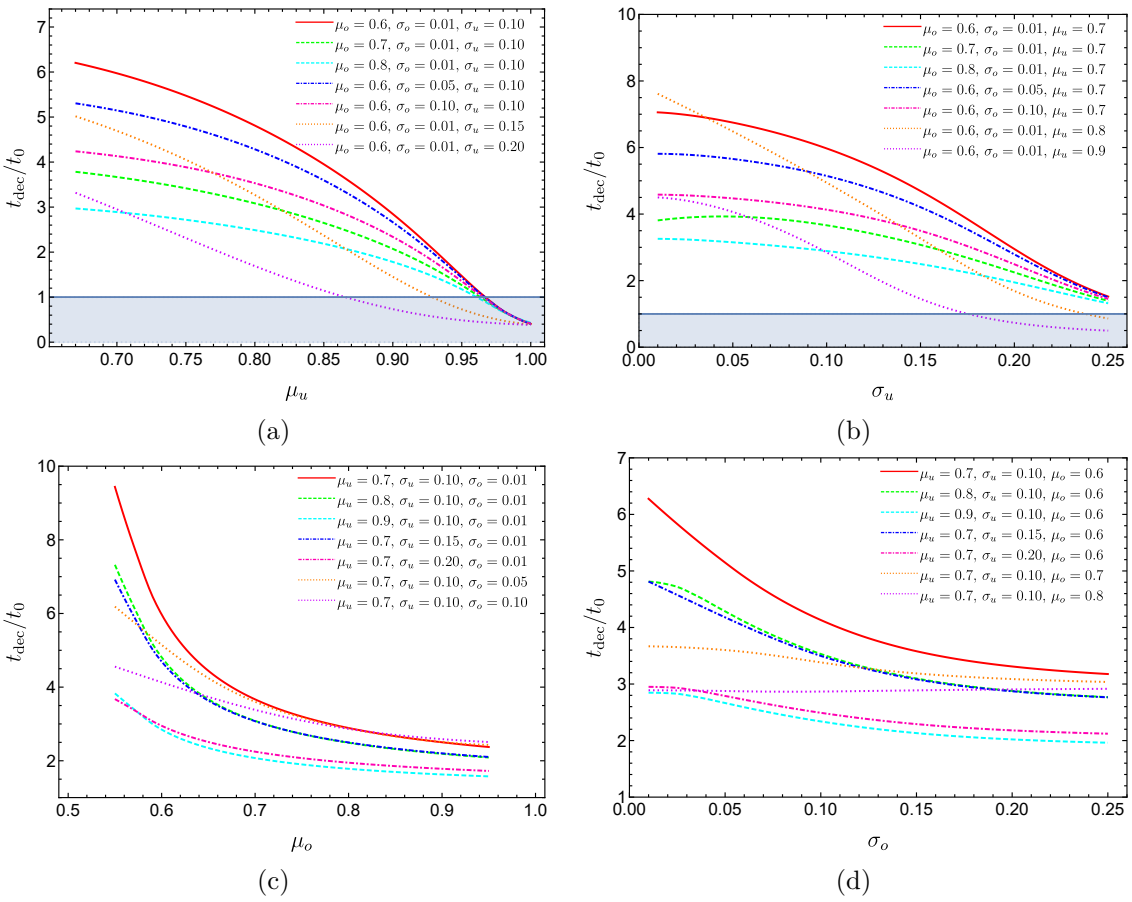

Figure 5.4: Variation of t_{dec} with (a) μ_u for different chosen values of μ_o, σ_o and σ_u, (b) σ_u for different chosen values of μ_o, σ_o and μ_u, (c) μ_o for different chosen values of μ_u, σ_u and σ_o, (d) σ_o for different chosen values of μ_u, σ_u and μ_o.

start falling in the future, and after a certain time ($t_{\rm dec}$), the quantity $\frac{\ddot{a_{\mathcal{D}}}}{a_{\mathcal{D}}H_{\mathcal{D}}^2}$ exhibits negative values, depicting the deceleration of the Universe. The value of $t_{\rm dec}$ varies with all four model parameters *i.e.* μ_u, σ_u, μ_o and σ_o. In (Fig. 5.4)(a), the variation of $t_{\rm dec}$ with μ_u is graphically represented for various sets of the other three parameters (*i.e.* σ_u, μ_o, and σ_o). Similar variations with σ_u, μ_o and σ_o are shown in (Fig. 5.4)(b), (Fig. 5.4)(c) and (Fig. 5.4)(d) respectively. From these figures, it can be seen that, with an increase in the model parameters, we get lower values of $t_{\rm dec}$. An increase in μ_o or μ_u, results in the increase of the most frequent value of q_{o_i} or β_i in the distribution of overdense or underdense subdomains, respectively. Hence, higher values of μ_o result in overdense subdomains with higher values of q_{o_i} becoming more prominent which leads to the acceleration parameter falling faster (refer to the discussion for Fig. 5.1) and hence, results in lower values of $t_{\rm dec}$. Similarly, higher values of μ_u result in underdense subdomains with higher values of β_i becoming more prominent, leading to lower values of $t_{\rm dec}$. Higher values of σ_o for a given μ_o result in the distribution of subdomains becoming wider around the mean value of μ_o. Therefore, there are now more subdomains with a larger value of q_{o_i} in the distribution, resulting in lower values of $t_{\rm dec}$. Similarly, higher values of σ_u for a given μ_u result in more subdomains with a larger value of β_i in the distribution, resulting in lower values of $t_{\rm dec}$. In (Fig. 5.4)(a) and (Fig. 5.4)(b), one can see that for higher values of μ_u in the presence of higher σ_u, the values of $t_{\rm dec}$ is less than t_0, which contradicts with observational evidence. Hence, such values are ruled out of the permissible range (grey shaded region).

In (Fig. 5.5), the variation of $t_{\rm dec}$ in $\mu_u - \sigma_u$ plane is shown for different sets of μ_o and σ_o. The values of $t_{\rm dec}$ are described using different colors, as mentioned in the color bar furnished at the bottom of (Fig. 5.5). Here, the white regions denote the area where $t_{\rm dec} \leq t_0$ is beyond the permissible range. From (Fig. 5.5) one can see that, the value of $t_{\rm dec}$ falls sharply with respect to the point $(\mu_u, \sigma_o) = (0.67, 0.01)$ in the scaled axes ($\mu_u \in [0.67, 1.00]$, $\sigma_u \in [0.01, 0.25]$). The plot of (Fig. 5.5)(a) represents the case of $\mu_o = 0.6$, $\sigma_o = 0.01$, where the maximum possible value of $t_{\rm dec} \approx 7.5 t_0$ is obtained at $\mu_u = 0.67$, $\sigma_o = 0.01$. But it decreases remarkably at a higher value of σ_o ($\sigma_o = 0.05$) (comparing parts (a) and (b) of the figure). $t_{\rm dec}$ also decreases on increasing the value of μ_o as can be seen by comparing parts (a) and (c) of the figure, where μ_o has increased from 0.6 to 0.8. This is in accordance with our previous analysis of (Fig. 5.4) and the related discussion showing that $t_{\rm dec}/t_0$ has lower values for higher values of μ_o and μ_u. (Fig. 5.5)(c) and (Fig. 5.5)(d) are the same to the plots of (Fig. 5.5)(a) and (Fig. 5.5)(b) respectively, where the parameter μ_u is set at 0.8. Comparing those plots, it can be seen that, at higher values of μ_o, the variation of $t_{\rm dec}$ is comparatively small and $t_{\rm dec}/t_0$ is very close to unity ($t_{\rm dec} \lessapprox 3t_0$ for $\mu_o = 0.8$). It can also be seen from parts (c) and (d) of the figure that the variation of $t_{\rm dec}$ is also negligible on increasing the value of σ_o for

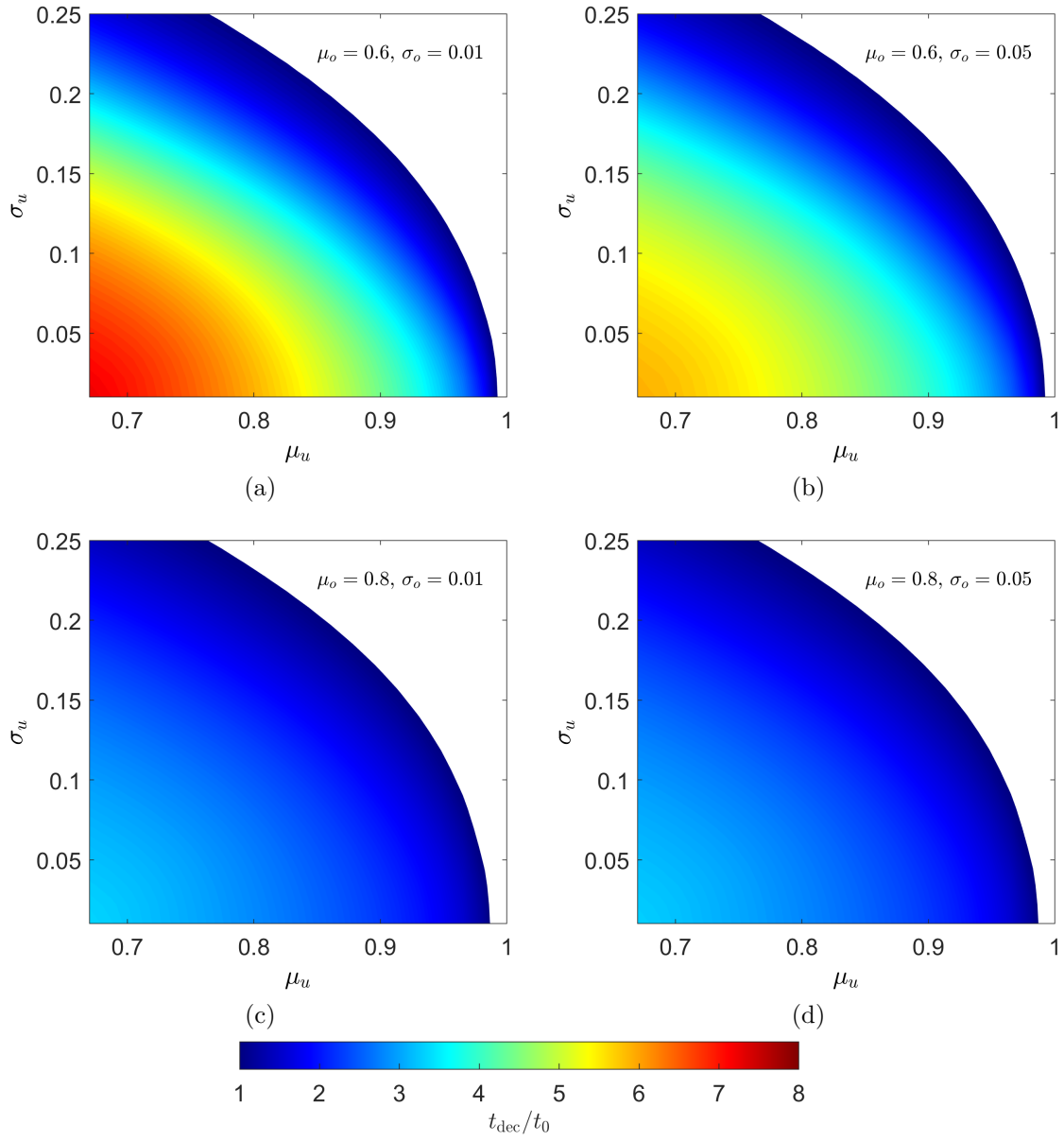

Figure 5.5: Contour representation of t_{dec} in $\sigma_u - \mu_u$ plane at (a) $\mu_o = 0.6$, $\sigma_o = 0.01$ (b) $\mu_o = 0.6$, $\sigma_o = 0.05$, (c) $\mu_o = 0.8$, $\sigma_o = 0.01$, (d) $\mu_o = 0.8$, $\sigma_o = 0.05$.

such higher values of μ_o.

A similar analysis is performed in the $\sigma_o - \mu_o$ plane. In (Fig. 5.6)(a), the contour representation shown the variation of $t_{\rm dec}$ for the case of $\mu_u = 0.7$ and $\sigma_u = 0.1$. (Fig. 5.6)(b) is plotted for $\mu_u = 0.7$ and $\sigma_u = 0.2$. (Fig. 5.6)(c) and (Fig. 5.6)(d) are the same to the plots (Fig. 5.6)(a) and (Fig. 5.6)(b) respectively, but for $\mu_u = 0.8$. Larger values of $t_{\rm dec}/t_0$ are obtained in part (a) of the figure for lower values of μ_o and σ_o. As the values of μ_o and σ_o are increased, the value of $t_{\rm dec}/t_0$ decreases. From parts (a) and (c), one can notice that for higher values of μ_u, the value of $t_{\rm dec}/t_0$ decreases if the values of (μ_o, σ_o) are kept fixed. The variation of $t_{\rm dec}$ becomes insignificant for higher values of the parameters. Parts (b) and (d) show that at higher values of σ_u, the variation in the $\sigma_o - \mu_o$ plane almost vanishes. These results are in accordance with the analysis and discussion relating to (Fig. 5.4).

5.4 Observational constraints

In (Fig. 5.1 - Fig. 5.6), we have utilized our model to examine the future evolution of an inhomogeneous multi-domain-ed spacetime, and analyzed the variation of various cosmological quantities with respect to our model parameters. Now, we examine our model with respect to observational data and determine the optimum values of our model parameters. We carry out a Bayesian analysis in order to compare our model with Union2.1 supernova Ia data [155]. We use the distance modulus versus redshift data from Union2.1. In order to compare our model with the observational data, we need a scheme to relate the theoretically calculated quantities from our model to observational quantities. For this purpose, we employ the covariant scheme explained in detail in (Sec. 2.2).

In this analysis, the resulting posterior distributions of different parameters are obtained by the Markov Chain Monte Carlo (MCMC) iteration method (Fig. 5.7) by using the `MCMCSTAT` package [91, 92]. We use total 10^5 number of events with the adaptation interval of 300, within the parameter range: $\mu_u \in [0.67, 1.00]$, $\log_{10}\sigma_u \in [-0.60, -0.15]$, $\mu_o \in [0.51, 1.00]$ and $\log_{10}\sigma_o \in [-3.00, -0.30]$. Initially, the same analysis was carried out with a wider range of $\log_{10}\sigma_u$ and $\log_{10}\sigma_o$, but later those ranges were redefined in order to skip the extremely lower posterior regions.

In (Fig. 5.7), the parameters σ_u and σ_o are shown in log-scale while the other two parameters μ_u and μ_o are shown in linear-scale. The topmost plots of the first, second, third and fourth column of (Fig. 5.7) represent the posterior distribution for the parameters μ_u, $\log_{10}\sigma_u$, μ_o and $\log_{10}\sigma_o$ respectively, while the other plots of (Fig. 5.7) show the contour representation of the posterior distribution in different sets of two-parameter space. In these contour plots, the regions with darker

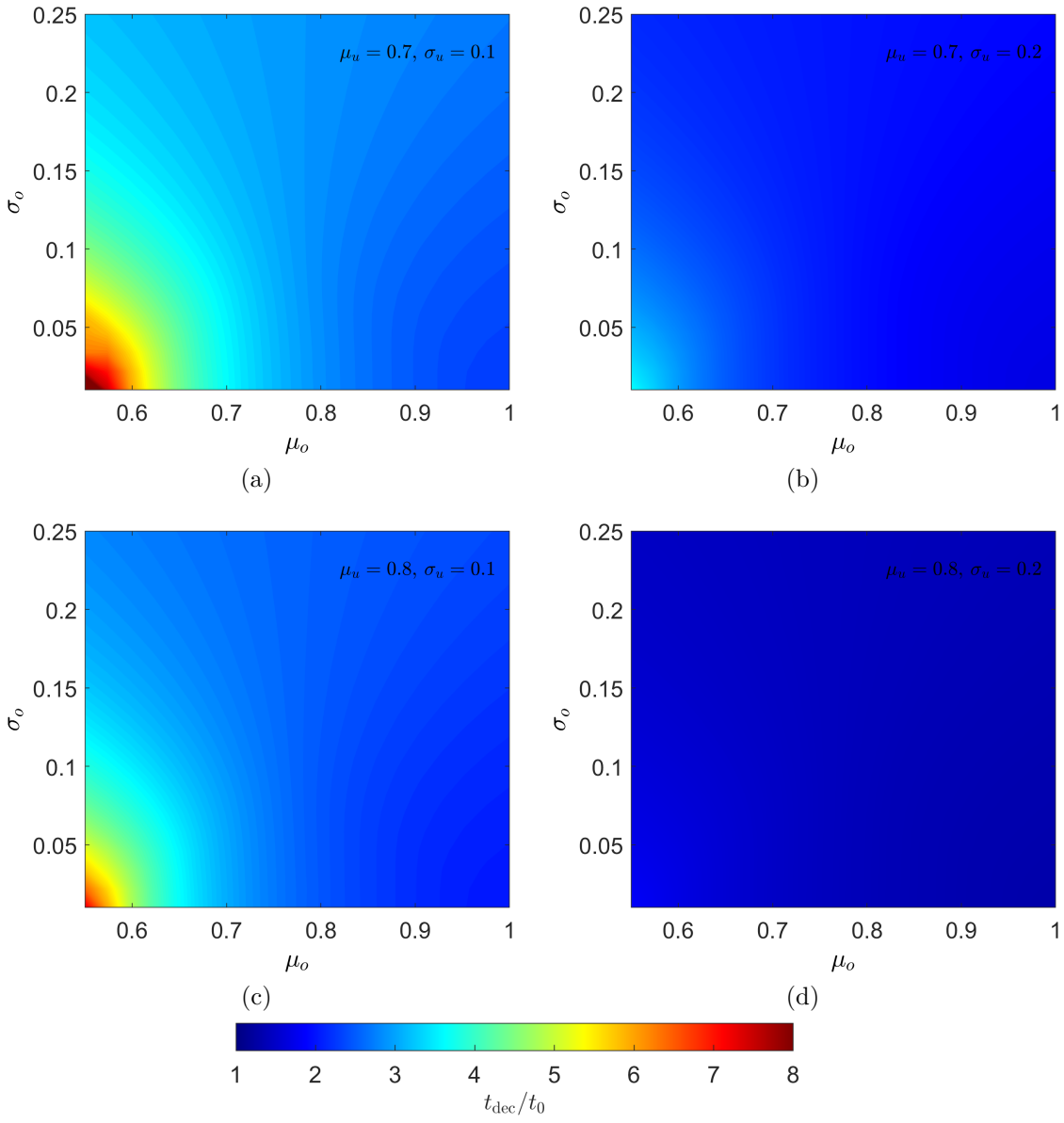

Figure 5.6: Contour representation of $t_{\rm dec}$ in $\sigma_o - \mu_o$ plane at (a) $\mu_u = 0.7$, $\sigma_u = 0.1$ (b) $\mu_u = 0.7$, $\sigma_u = 0.2$, (c) $\mu_u = 0.8$, $\sigma_u = 0.1$, (d) $\mu_u = 0.8$, $\sigma_u = 0.2$.

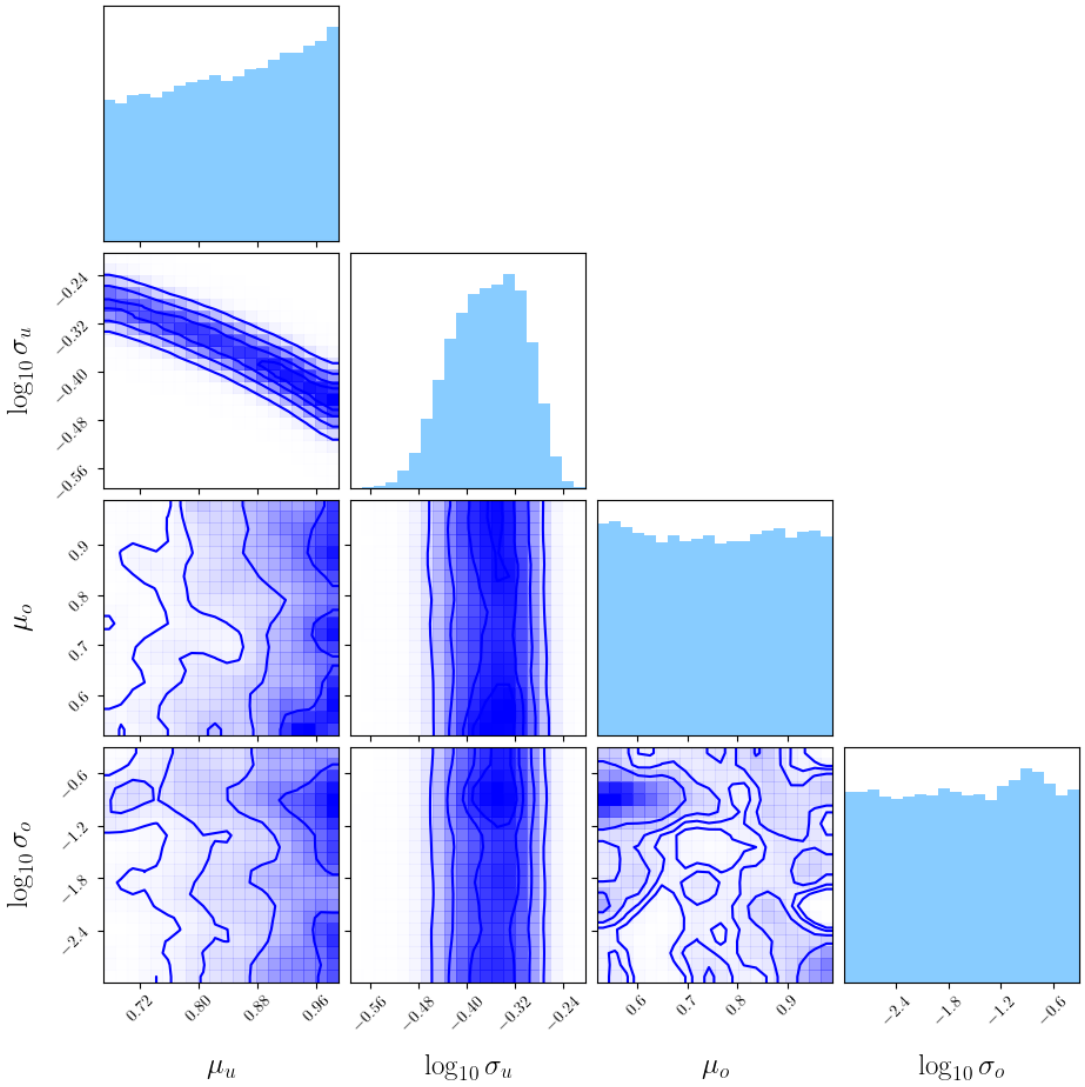

Figure 5.7: Corner plot showing the MCMC result for our model carried out using the observational results of Union 2.1 supernova Ia data [155]. The histograms on the diagonal show the marginalized posterior densities for each parameter.

colors denote higher posterior regions, and the lines indicate the boundaries of 1σ, 2σ, and 3σ regions, respectively. The posterior plots essentially describe the epistemic uncertainties of the corresponding model parameters. The diagonal panels show the 1-D histogram of the posterior distribution for each model parameter obtained by marginalizing the other parameters. The off-diagonal panels show 2-D projections of the posterior probability distributions for each pair of parameters and correlations between the parameters, with contours.

From this analysis the obtained set of optimum points are $\mu_u = 0.85^{+0.10}_{-0.12}$, $\log_{10}\sigma_u = -0.36^{+0.06}_{-0.07}$, $\mu_o = 0.75^{+0.16}_{-0.16}$ and $\log_{10}\sigma_o = -1.63^{+0.90}_{-0.94}$ respectively. However, from the posterior plot for $\log_{10}\sigma_u$ (in Fig. 5.7), one can notice that the highest probable value (or best-fit value) of $\log_{10}\sigma_u$ is slightly higher (*i*.e. $\log_{10}\sigma_u = -0.33$) than the corresponding optimum point. On the other hand, the best-fit point for μ_u lies on its highest posterior value (*i.e.* $\mu_u = 1.00$). From the histograms of (Fig. 5.7), it is evident that variation of the parameters of the overdense regions (μ_o and σ_o) do not play a very significant role as histograms depicting the marginalized posterior distributions for these two parameters do not show any specific significant trend. Similarly, in the off-diagonal panels of these two parameters, there is no specific trend, while the off-diagonal panels of other pairs show some specific trend. For example, the $\mu_u - log_{10}\sigma_o$ and $\mu_u - \mu_o$ panels show a specific trend towards higher values of μ_u (darker regions are towards higher values of μ_u and this trend is also indicated by the histogram for μ_u). These indicate that the modification of the volume fractions distribution of the overdense regions by modifying the mean and standard deviation of the distribution (Eq. 5.7) doesn't have much effect on the future evolution of the Universe, as the fraction of overdense region at the present era is taken to be $\sim 9\%$ [27].

5.5 Conclusions

In this work, we have considered a multi-domain model of spacetime with an inhomogeneous matter distribution. The multiple subregions in our model are broadly categorized into two types - overdense and underdense, with all such subregions having distinct evolution parameters. In the context of the Buchert formalism, we have computed the averaged backreaction of the matter inhomogeneities on the late-time global evolution of the Universe.

Our results clearly indicate that the global acceleration falls with time beyond the present epoch for a significant range of values of our model parameters. Such a feature was predicted earlier for dust Universe models [154], and also observed in the context of simplified two-scale models [44–46], is further corroborated here through the analysis of a more realistic model. We have shown here that after a particular time (t_{dec}), the value of the global acceleration parameter can become

negative, signifying the transition of the presently accelerating Universe to a phase of future deceleration.

Through our analysis, we have optimized our model for the maximum number of subregions to be considered for a reliable result for future global evolution. The dependence of the deceleration time (t_{dec}) on the various model parameters has been analyzed systematically. The variation of (t_{dec}) shows that the model parameters associated with the underdense subregions have more impact on the transition time for future deceleration. We have further correlated our model with observation data. We have obtained the marginalized posterior densities for each model parameter through Markov Chain Monte Carlo (MCMC) simulations using the Union2.1 supernova Ia data.

We conclude by noting that though the present era Universe is accelerating [147–150], such behaviour could indeed be transitory. Observations have shown that the present Universe has an inhomogeneous matter distribution at considerably large scales [8, 9]. It seems inevitable that an impact of backreaction of matter inhomogeneities on the global metric to plausibly avoid the future big chill in the ΛCDM model or a possible future big rip problem in the presence of phantom dark energy. Our present results motivate further investigations in the context of various backreaction schemes and upcoming probes with more accurate observations to critically examine our conjecture of the future deceleration of the Universe.

Chapter 6

Analyzing the 21-cm signal brightness temperature in the Universe with inhomogeneities

6.1 Introduction

21 cm cosmology has been an essential tool in studying the physics of the cosmic dark age for quite some time now [158–160]. It is a unique probe of the re-ionization epoch of the Universe [161, 162]. 21-cm is the wavelength corresponding to the energy shift due to hyperfine splitting in the ground state of neutral Hydrogen, the most abundant element in the Universe. It occupies $\sim 75\%$ of the entire baryonic allocation of the Universe. The transition between hydrogen atoms' electronic spin states (s = 0, 1) generates the 21-cm ($\sim$ 1.42 GHz) hyperfine spectrum.

The brightness temperature T_{21} associated with this spectrum is a function of $T_s - T_\gamma$ where T_γ is the cosmic microwave background temperature given by $T_\gamma = 2.725(1 + z)K$ and T_s is the spin temperature [158–160]. Recently, the "Experiment to Detect the Global Epoch of Re-ionization Signature" (EDGES) [163] generated quite a bit of excitement in the field with its reported T_{21} in the redshift range $14 < z < 20$ to be -500^{+200}_{-500} mK. However, the subsequent SARAS experiment [164] failed to detect the EDGES 21 cm signal [165].

The ΛCDM model of standard cosmology estimates a brightness temperature of about ≈ -200 mK without any additional thermal contribution. To account for any additional cooling, various phenomenological effects in the early Universe have been employed [166–171], including exotic models of dark matter [168, 170, 172] and dark energy [128]. The 21-cm signal provides an avenue towards discerning several physical phenomena of this epoch, such as evaporating primordial black holes (PBHs) [166, 169, 171, 173], baryon-dark matter scattering [168, 170, 172], and neutrino physics [174].

Although the ΛCDM model has been highly successful in establishing the basic tenets of standard cosmology, it has been confronted with certain discordant observations in recent times, notably among them the so-called Hubble tension [6, 7]. As highlighted in (Chap. 1), recent observations have revealed prominent matter distribution inhomogeneities up to scales as large as 500 h^{-1} Mpc [9].

Such observed deviations in LSS from the assumed smooth homogeneous ΛCDM paradigm may necessitate the inclusion of the impact of inhomogeneities in the analyses of cosmological phenomena. In this analysis, we have used Buchert's averaging procedure mentioned in detail in (Chap. 2) to incorporate the effect of matter distribution inhomogeneities in our analysis.

Specifically, in the present analysis, we employ a model of spacetime with a spectrum of matter distribution inhomogeneities in multiple domains, which can imitate our actual Universe more realistically compared to earlier analyses of cosmological dynamics under backreaction, which have primarily relied on toy two-domain models [35, 44–47]. We aim to theoretically analyze the 21-cm signal in the context of modified Hubble dynamics due to the effect of backreaction from matter distribution inhomogeneities evaluated using the Buchert formalism. We constrain our model parameters by performing Markov Chain Monte Carlo analysis using the Union2.1 supernova Ia data to determine the model parameters' best fit and optimum values. We compute the 21-cm brightness temperature, which reveals a significant dip compared to the ΛCDM prediction in the redshift range $14 < z < 20$, without invoking any additional non-standard cosmological effects or exotic physics.

This chapter is organized as follows. We briefly introduce the formalism for evaluating the 21-cm signal brightness temperature in (Sec. 6.2). Our model of multidomain inhomogeneities is presented, leading to modified Hubble dynamics in (Sec. 6.3). We then present our analysis of the 21-cm signal in the context of our multidomain model in (Sec. 6.4). In (Sec. 6.5), we use the Union2.1 supernova Ia data to constrain our model parameters and compute the 21 cm brightness temperature in the redshift range $14 < z < 20$ using the best fit and optimum values of our model parameters. Finally, we summarize our results in (Sec. 6.6).

6.2 21-cm brightness temperature

The 21-cm absorption line of the hydrogen atom is generated by the transition of an electron between the two hyperfine spin states (spin 0 and spin 1). This 21-cm line has a characteristic temperature associated with it called the brightness temperature, T_{21}, which represents the intensity of the 21-cm line as a function

of the cosmological redshift z. The expression for T_{21} is given by [167, 175],

$$T_{21} = \frac{T_s - T_\gamma}{1+z}(1 - e^{-\tau(z)}), \tag{6.1}$$

where T_s is the 21-cm spin temperature at redshift z, T_γ is the cosmic microwave background (CMB) temperature ($T_\gamma = 2.725(1+z)K$) and $\tau(z)$ is the optical depth of the inter-galactic medium (IGM). $\tau(z)$ is given by [175],

$$\tau(z) = \frac{3}{32\pi}\frac{T_*}{T_s} n_{HI}\lambda_{21}^3 \frac{A_{10}}{H(z) + (1+z)\delta_r v_r} \tag{6.2}$$

where $T_* = hc/(k_B\lambda_{21}) = 0.068$ K, $A_{10} = 2.85 \times 10^{-15} s^{-1}$ is the Einstein coefficient [176], $\lambda_{21} \approx 21$ cm, n_{HI} is the local neutral hydrogen density, $H(z)$ is the Hubble parameter and $\delta_r v_r$ is the radial gradient of the peculiar velocity. The above equations are derived from the principles of atomic physics and radiative transfer. The expression for optical depth has a term for the gradient of the proper velocity along the line of sight, and this term includes both the Hubble expansion and the peculiar velocity, as can be seen in (Eq. 6.2) [158]. This is how $H(z)$, the Hubble parameter, which measures the Universe's rate of expansion, enters the analysis. Since $H(z)$ itself depends on the model of cosmology, the values of the quantities of interest turn out to be different for different models of cosmology.

The spin temperature T_s is related to the ratio of the number density of hydrogen atoms in excited and ground states and is given by [175],

$$\frac{n_1}{n_0} = 3e^{-T_*/T_s} \tag{6.3}$$

where n_1 and n_0 are the number densities of hydrogen atoms in excited and ground states, respectively. In equilibrium, T_s is given by [169, 177],

$$T_s = \frac{T_\gamma + y_c T_b + y_{Ly\alpha} T_{Ly\alpha}}{1 + y_c + y_{Ly\alpha}} \tag{6.4}$$

where y_c is the collisional coupling parameter, T_b is the baryon temperature, $y_{Ly\alpha}$ represents the Wouthuysen-Field effect [178, 179] and $T_{Ly\alpha}$ is the Lyman-α ($Ly\alpha$) background temperature. The coefficients y_c and $y_{Ly\alpha}$ are given by $y_c = \frac{C_{10}T_*}{A_{10}T_b}$ and $y_{Ly\alpha} = \frac{P_{10}T_*}{A_{10}T_{Ly\alpha}}$ [180]. Here, C_{10} is the collisional de-excitation rate of the triplet hyperfine level, $P_{10} \approx 1.3 \times 10^{-12} S_\alpha J_{-21} s^{-1}$ is the indirect de-excitation rate due to Ly-α absorption, S_α is a factor of order unity that incorporates spectral distortions [181] and J_{-21} is the Lyman-α background intensity written in units of 10^{-21} erg cm^{-2} s^{-1} Hz^{-1} sr^{-1}, and can be estimated by the procedure mentioned in [169, 182].

The baryon temperature T_b can be obtained from the standard evolution equations of T_b and x_e, the ionization fraction. The ionization fraction x_e is given by

$x_e = n_e/n_H$, where n_e and n_H are the number densities of free electron and Hydrogen, respectively, is an important quantity in estimating thermal evolution. Here, we will not consider exotic physics or non-standard processes like dark matter decay. We just consider standard evolution equations. These equations governing thermal evolution are given by [169, 183, 184],

$$(1+z)\frac{dT_b}{dz} = 2T_b + \frac{\Gamma_c}{H(z)}(T_b - T_\gamma), \tag{6.5}$$

$$(1+z)\frac{dx_e}{dz} = \frac{C_P}{H(z)}\left(n_H\alpha_B x_e^2 - 4(1-x_e)\beta_B e^{-\frac{3E_0}{4k_B T_\gamma}}\right), \tag{6.6}$$

where Γ_c $\left(\Gamma_c = \frac{8\sigma_T a_r T_\gamma^4 x_e}{3(1+f_{He}+x_e)m_e c}\right)$ describes the Compton interaction rate (σ_T is the Thomson scattering cross-section, a_r is the radiation constant, f_{He} is the fractional abundance of Helium, m_e is the mass of an electron), C_P is the Peebles C factor [183, 185], $E_0 = 13.6$ eV, k_B is the Boltzmann constant and α_B and β_B are the recombination and ionization coefficients, respectively. The Peebles C factor is given by [183],

$$C_P = \frac{\frac{3}{4}R_{Ly\alpha} + \frac{1}{4}\Lambda_{2s1s}}{\beta_B + \frac{3}{4}R_{Ly\alpha} + \frac{1}{4}\Lambda_{2s1s}} \tag{6.7}$$

where $R_{Ly\alpha}$ represents the rate of escape of Ly α photons,
$R_{Ly\alpha} = 8\pi H/\left(3n_H(1-x_e)\lambda_{Ly\alpha}^3\right)$, n_H is the total number density of Hydrogen and $\Lambda_{2s,1s} \approx 8.22\text{s}^{-1}$ [183]. α_B and β_B can be calculated using the procedure mentioned in [166, 167]. Similar to the case of (Eq. 6.1) and (Eq. 6.2), the cosmological dependence of the equations (Eq. 6.5 and Eq. 6.6) are enshrined in $H(z)$, the Hubble parameter.

6.3 A model of multiple subregions

Several studies have been performed within the Buchert averaging scheme using models having just one type of overdense subdomain and one type of underdense subdomain [36, 42, 44–47]. This oversimplifies the actual spacetime scenario with matter inhomogeneities, where the matter density may vary from very low to very high across different subdomains. Therefore, a more realistic model would have multiple overdense and underdense subregions with distinct evolution profiles. A similar model has been used in [53] to study the future evolution of the currently accelerating Universe with multiple inhomogeneous domains.

Here, using Buchert's backreaction framework, we consider a model of the Universe in which domain $\mathcal{D}$ comprises multiple underdense and overdense subregions, *viz.*, there are i number of overdense subregions and i number of underdense subregions. The underdense subregions have densities smaller than those of the overdense subregions. Our underdense subregions are modelled to mimic al-

most empty FLRW regions with very little matter (dust) present. The overdense subregions are modeled to mimic FLRW models with matter (dust) content. The underdense subregions are taken to have Friedmann-like $1/a^2$ negative curvature, while the overdense subregions have Friedmann-like $1/a^2$ positive curvature. The time evolution of the scale factor of i^{th} overdense subregions, a_{o_i} is given in terms of a development angle ϕ_{o_i} of the i^{th} overdense subregion [136],

$$a_{o_i} = \frac{q_{o_{i,0}}}{2q_{o_{i,0}} - 1}(1 - \cos\phi_{o_i}) \tag{6.8}$$

$$t = t_0 \frac{(\phi_{o_i} - \sin\phi_{o_i})}{(\phi_{o_{i,0}} - \sin\phi_{o_{i,0}})} \tag{6.9}$$

where $q_{o_{i,0}}$ and $\phi_{o_{i,0}}$ are respectively the deceleration parameter of the i^{th} overdense subregion and the value of ϕ_{o_i} at time t_0, which is the present time. $q_{o_{i,0}}$ should be greater than $1/2$ [136]. Here, we have taken $q_{o_{i,0}}$ to have a range of values from $1/2$ to 1. The time t in (Eq. 6.9) [35, 54] is the cosmic time, although for each overdense subregion, this t is parameterized in terms of $(\phi_{o_{i,0}}, \phi_{o_i})$ ($\phi_{o_{i,0}}$ itself is a function of $q_{o_{i,0}}$). The value of t_0 is the same across all overdense subregions as well as for the global domain which is ensured by the specific form of (Eq. 6.9). The time evolution of the scale factor of i^{th} underdense subregions, a_{u_i} is given in terms of a development angle ϕ_{u_i} of the i^{th} underdense subregion [136],

$$a_{u_i} = \frac{q_{u_{i,0}}}{1 - 2q_{u_{i,0}}}(\cosh\phi_{u_i} - 1) \tag{6.10}$$

$$t = t_0 \frac{(\sinh\phi_{u_i} - \phi_{u_i})}{(\sinh\phi_{u_{i,0}} - \phi_{u_{i,0}})} \tag{6.11}$$

where $q_{u_{i,0}}$ and $\phi_{u_{i,0}}$ are respectively the deceleration parameter of the i^{th} underdense subregion and the value of ϕ_{u_i} at time t_0, which is the present time. $q_{u_{i,0}}$ has a range of values from 0 to $1/2$ [136]. The time t in (Eq. 6.11) is the cosmic time, although for each underdense subregion, this t is parameterized in terms of $(\phi_{u_{i,0}}, \phi_{u_i})$ ($\phi_{u_{i,0}}$ itself is a function of $q_{u_{i,0}}$). The value of t_0 is the same across all underdense and overdense subregions as well as for the global domain, which is ensured by the specific form of (Eq. 6.11) and (Eq. 6.9). Since the values of t_0 and $H_{\mathcal{D}_0}$ are interrelated, one needs to fix either of them [54]. In our subsequent analysis, we choose $H_{\mathcal{D}_0}$ to be 70 $km\ s^{-1}Mpc^{-1}$. The value of t_0 is calculated using the procedure used in [54], modified for our model (see Appendix B).

Note that a_{o_i} and a_{u_i} can be expressed in terms of the volume of the respective subregions using (Eq. 2.9), which gives us

$$a_{o_i}(t) := \left(\frac{|\mathcal{D}|_{o_i}}{|\mathcal{D}_0|_{o_i}}\right)^{1/3}; \quad a_{u_i}(t) := \left(\frac{|\mathcal{D}|_{u_i}}{|\mathcal{D}_0|_{u_i}}\right)^{1/3} \tag{6.12}$$

where, $|\mathcal{D}|_{o_i}$ is the volume of the i^{th} overdense subregions at time t, $|\mathcal{D}_0|_{o_i}$ is the volume of the i^{th} overdense subregion at time t_0 as was done in (Eq. 2.9), and similarly for the case of the underdense subregions. (Eq. 2.9) and (Eq. 6.12) require that at $t = t_0$, $a_{\mathcal{D}} = a_{o_i} = a_{u_i} = 1$, leading to,

$$\cos\phi_{o_{i,0}} = \left(\frac{1}{q_{o_{i,0}}} - 1\right); \quad \cosh\phi_{u_{i,0}} = \left(\frac{1}{q_{u_{i,0}}} - 1\right) \tag{6.13}$$

For a given value of $q_{o_{i,0}}$ and $q_{o_{i,0}}$; $a_{o_i}(t)$ and $a_{u_i}(t)$ can be calculated using (Eq. 6.8), (Eq. 6.9), (Eq. 6.10), (Eq. 6.11) and (Eq. 6.13). Then using (Eq. 2.23), $a_{\mathcal{D}}(t)$ can be obtained provided λ_{l_0} which is the set of all $\lambda_{u_i,0}$ and $\lambda_{o_i,0}$, is known.

It may be noted that $a_{\mathcal{D}}$ can also be obtained from solving the second-order differential equation (Eq. 2.24). Using (Eq. 6.8) and (Eq. 6.10) in (Eq. 2.24), we get,

$$\begin{aligned}\frac{\ddot{a}_{\mathcal{D}}}{a_{\mathcal{D}}} = &\left(\sum_i \lambda_{o_i}\frac{\ddot{a}_{o_i}}{a_{o_i}}\right) + \left(\sum_j \lambda_{u_j}\frac{\ddot{a}_{u_i}}{a_{u_i}}\right) \\ &+ \left(\sum_k \sum_l \lambda_k\lambda_l\,(H_l - H_k)^2\right).\end{aligned} \tag{6.14}$$

where, λ_{o_i} is the volume fraction of the i^{th} overdense subregion, λ_{u_j} is the volume fraction of the j^{th} underdense subregion, λ is the set of all λ_{o_i} and λ_{u_i} and H is respectively, the set of all H_{o_i} and H_{u_i}. The combined volume fraction of all the underdense subregions is given by λ_u, i.e., $\sum_i \lambda_{u_i} = \lambda_u$. Similarly, the total volume fraction of all the overdense subregions is given by $\sum_i \lambda_{o_i} = \lambda_o$. Clearly, $\lambda_o + \lambda_u = 1$. The evaluation of $a_{\mathcal{D}}$ obtained from these two methods is identical, as confirmed through our analysis.

The volume fraction of the i^{th} overdense subregion can be written as,

$$\lambda_{o_i} = \frac{|\mathcal{F}_{o_i}|_g}{|\mathcal{D}|_g} = \frac{a_{o_i}^3|\mathcal{F}_{o_i,0}|_g}{a_{\mathcal{D}}^3|\mathcal{D}_0|_g} = \lambda_{o_i,0}\frac{a_{o_i}^3}{a_{\mathcal{D}}^3} \tag{6.15}$$

where t_0 is a reference time which can be taken as the present time, $|\mathcal{F}_{o_i}|_g$ is the volume of the i^{th} overdense subregion, $|\mathcal{F}_{o_i,0}|_g$ is the volume of the i^{th} overdense subregion at time t_0, $|\mathcal{D}_0|_g$ is the volume of the domain $\mathcal{D}$ at time t_0 and $\lambda_{o_i,0}$ is the volume fraction of the i^{th} overdense subregion at time t_0. The present time (t_0) value of (λ_o, λ_u) is given by $(\lambda_{o,0}, \lambda_{u,0})$ which we have taken to be (0.09,0.91) [27].

In our model, we consider the present time volume fraction of i^{th} underdense subregion, $\lambda_{u_i,0}$ to have a Gaussian distribution within the allowed range of $q_{u_{i,0}}$

from 0 to 1/2, given by,

$$\lambda_{u_i,0} = \frac{N_u}{\sigma_u \sqrt{2\pi}} e^{-(q_{u_{i,0}} - \mu_u)^2 / 2\sigma_u^2}, \tag{6.16}$$

where N_u is a normalization constant which ensures that $\sum_i \lambda_{u_i,0} = \lambda_{u,0} = 0.91$, μ_u is the mean value of $q_{u_{i,0}}$ and σ_u is the standard deviation of $q_{u_{i,0}}$. Therefore, each i^{th} underdense subregion is associated with a particular value of $q_{u_{i,0}}$ and $\lambda_{u_i,0}$ such that $q_{u_{i,0}}$ varies from 0 to 1/2 in the i number of underdense subregions and $\sum_i \lambda_{u_i,0} = 0.91$.

The present-time volume fraction of i^{th} overdense subregion, $\lambda_{o_i,0}$ is considered to have a Gaussian profile within the allowed range of $q_{o_{i,0}}$ from 1/2 to 1 given by,

$$\lambda_{o_i,0} = \frac{N_o}{\sigma_o \sqrt{2\pi}} e^{-(q_{o_{i,0}} - \mu_o)^2 / 2\sigma_o^2}, \tag{6.17}$$

where N_o is a normalization constant which ensures that $\sum_i \lambda_{o_i,0} = \lambda_{u,0} = 0.09$, μ_o is the mean value of $q_{o_{i,0}}$ and σ_o is the standard deviation of $q_{o_{i,0}}$. In this case, each i^{th} overdense subregion is associated with a particular value of $q_{o_{i,0}}$ and $\lambda_{o_i,0}$, where $q_{o_{i,0}}$ lies within the range 1/2 to 1 across the i number of overdense subregions and $\sum_i \lambda_{o_i,0} = 0.09$. The volume fraction of the i^{th} underdense subregion at a time t, λ_{u_i} is related to the volume fraction at present time t_0 by,

$$\lambda_{u_i} = \lambda_{u_i,0} \left(\frac{1 - \sum_i \lambda_{o_i}}{1 - \sum_i \lambda_{o_i,0}} \right), \tag{6.18}$$

We have used the Gaussian distribution to define the present time volume fraction of various subregions. The actual physical distribution can only be known by extensive galactic surveys of the matter distribution in the Universe. Although some such surveys have been performed for the local Universe, for the redshifts of our interest, no such surveys exist. Without such surveys, we assume a normal distribution used in analysis where we do not expect any bias. The Gaussian distribution is well-known and extensively used in diverse physical analyses to model unbiased physical conditions. (Further details of our model are provided in Appendix C).

Using (Eq. 2.22), the kinematical backreaction term for the domain $\mathcal{D}$ for our model effectively becomes

$$\mathcal{Q}_{\mathcal{D}} = \sum_i \lambda_{o_i} \mathcal{Q}_{o_i} + \sum_j \lambda_{u_j} \mathcal{Q}_{u_j} + 3 \sum_{l \neq m} \lambda_l \lambda_m (H_l - H_m)^2 , \tag{6.19}$$

where $\mathcal{Q}_{o_i}$ is the kinematical backreaction term for the i^{th} overdense subregion, $\mathcal{Q}_{u_i}$ is for the i^{th} underdense subregion. The summation in the last term runs over the sets of all λ_{o_i}, λ_{u_i}, H_{o_i} and H_{u_i}. (Eq. 2.16) couples the kinematical backreaction term to the Ricci scalar, and our subregions are also governed by this coupling.

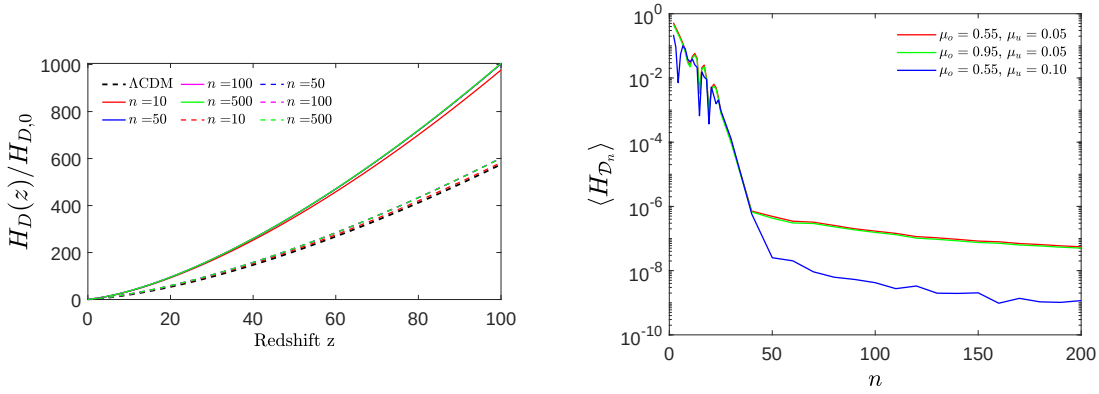

(a) (b)

Figure 6.1: Subplot (a) is the plot of $H_{\mathcal{D}}(z)/H_{\mathcal{D},0}$ for our backreaction model for different values of n, the number of underdense and overdense subregions. Here, $H_{\mathcal{D},0}$ is the value of $H_{\mathcal{D}}(z)$ at $z = 0$. The values of our model parameters are chosen as follows: $\mu_u = 0.49$, $\sigma_u = 0.01$, $\mu_o = 0.51$ and $\sigma_o = 0.01$ for solid lines and $\mu_u = 0.15$, $\sigma_u = 0.01$, $\mu_o = 0.51$ and $\sigma_o = 0.01$ for dashed lines. The ΛCDM model curve is shown with a black dashed line. Subplot (b) is the plot of $\langle H_{\mathcal{D}_n} \rangle$ versus n, the total number of subregions of each type. We take $\sigma_u = \sigma_o = 0.01$ for all three lines, while μ_u and μ_o are varied as mentioned in the legend.

Therefore, by selectively choosing the curvatures of our subregions, we can make the respective kinematical backreaction terms for these subregions equal to zero [17, 27]. Hence, in this case, the global kinematical backreaction is governed by only the interplay of the sub-domain Hubble evolutions and volume fractions (third term of (Eq. 6.19)). Note that the above assumptions are made in the context of our present model. On the other hand, if the subdomains are endowed with dynamical curvature, other intricate effects could arise through kinematical backreaction, as may also happen in a more general case where the subregions may not necessarily be FLRW.

Obtaining the values of $\lambda_{o_i,0}$ and $\lambda_{u_i,0}$ from (Eq. 6.17) and (Eq. 6.16) respectively, and using these in (Eq. 6.15) and (Eq. 6.18) gives us λ_{o_i} and λ_{u_i}. Hubble parameters for the subregions can be obtained from (Eq. 6.8, Eq. 6.9) and (Eq. 6.10, Eq. 6.11). We can then use (Eq. 6.14) to get $a_{\mathcal{D}}(t)$ and $H_{\mathcal{D}}(t)$. We next relate these quantities calculated theoretically from our model with observational quantities (redshift and angular diameter distance by using the covariant scheme (Sec. 2.2)). Here, we use (Eq. 2.25) to obtain $z(t)$ from $a_{\mathcal{D}}(t)$. We can thus evaluate $H_{\mathcal{D}}(z)$ using $H_{\mathcal{D}}(t)$ (from (Eq. 6.14)) and $z(t)$ (from (Eq. 2.25)).

In (Fig. 6.1) (a), $H_{\mathcal{D}}(z)/H_{\mathcal{D},0}$ has been plotted as a function of redshift z for different values of n, the number of each type of subregion - overdense and underdense. The total subregions is $2n$, n overdense subregions, and n underdense subregions. Here, $H_{\mathcal{D},0}$ is the value of $H_{\mathcal{D}}(z)$ at $z = 0$. Depending on the model parameters, our backreaction model may be very close to a perturbed FRW or mimic a single FRW at very early times. Considering a very high value of n does not lead to a significant difference, as can be seen in our following analysis. We

define

$$\langle H_{\mathcal{D}_n} \rangle = \frac{1}{\sum i} \sum_i \left| \frac{(H_{\mathcal{D}}(z)/H_{\mathcal{D},0})\big|_{500} - (H_{\mathcal{D}}(z)/H_{\mathcal{D},0})\big|_n}{(H_{\mathcal{D}}(z)/H_{\mathcal{D},0})\big|_{500}} \right|_{z=z_i}, \tag{6.20}$$

which denotes the redshift-averaged variation of $H_{\mathcal{D}_n}$, from the limiting case of $n = 500$. In this analysis, we split the redshift range (*i.e.* $0 \leq z \leq 100$) into 100 bins. In (Eq. 6.20), i is the index number of such bins. The variation of $\langle H_{\mathcal{D}_n} \rangle$ with n are plotted in (Fig. 6.1(b)). In this figure, the plots are for different chosen sets of μ_o and μ_u, while the other two parameters are kept at $\sigma_u = 0.01$ and $\sigma_o = 0.01$. For $n \geq 100$, the average fluctuation is less than $\sim 10^{-6}$. Given the above results, we chose $n = 100$ for our remaining calculations.

From here onward, in our calculations, we consider one hundred under-dense and one hundred over-dense sub-domains. These sub-domains are characterized by the respective volume fractions, λ_{o_i} and λ_{u_i} (Eq. 6.15 and Eq. 6.18), distributed using a Gaussian profile among these sub-domains (Eq. 6.16 and Eq. 6.17). Our underdense regions are characterized by parameters $q_{u_{i,0}}$ that vary from $0 < q_{u_{i,0}} < 0.5$ [136]. This range for $q_{u_{i,0}}$ has been taken to ensure a wide range of underdense subregions is present in our model to mimic a variety of underdense regions that may be present in the Universe. μ_u and σ_u are the mean and standard deviation of the Gaussian profile of the underdense regions. The underdense subregion with $q_{u_{i,0}} = \mu_u$ will have the largest value of λ_{u_i} and thus will be the most prominent underdense subregion in the analysis. Here, σ_u governs the distribution width about a given μ_u. Similarly, our overdense regions are characterized by parameters $q_{o_{i,0}}$ varying from $1/2 < q_{o_{i,0}} < 1$. This range for $q_{o_{i,0}}$ has been taken to ensure that a wide range of overdense subregions is present in our model to mimic a variety of overdense regions that may be present in the Universe. μ_o and σ_o are the mean and standard deviation for the Gaussian profile of overdense regions. The overdense subregion with $q_{o_{i,0}} = \mu_o$ will have the highest value of λ_{o_i} and, therefore, will be the most prominent overdense subregion in the analysis. σ_o is the standard deviation of the distribution, which governs the width of the distribution about the mean value.

In (Fig. 6.2), the average density parameters are plotted as a function of the redshift in the redshift range ($z < 30$). (See Appendix (C) for the calculation of these average density parameters). The density parameter associated with kinematical backreaction $\mathcal{Q}_{\mathcal{D}}$ plays a significant role in our backreaction model at late redshifts (around $z = 5$, as seen from the inset), embodying the departure from FLRW behavior in our framework. The $\mathcal{Q}_{\mathcal{D}}$ term becomes negligible at large redshifts, which can be seen from the corresponding plot in (Fig. 6.2). The term $\Omega_{\mathcal{Q}}^{\mathcal{D}}$ going to zero at high redshifts (or at early times) shows that our model can mimic a perturbed FLRW model at early times.

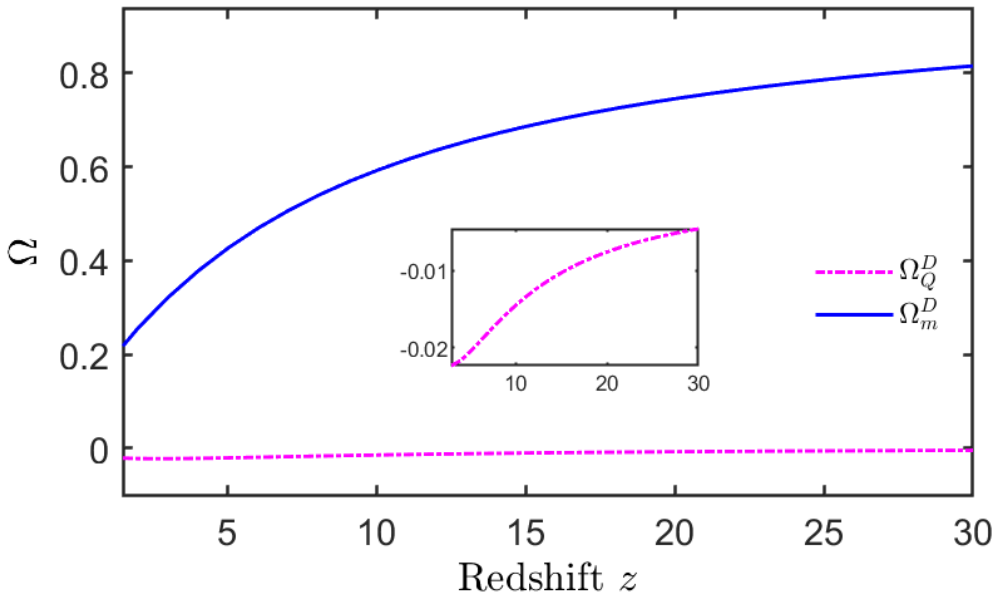

Figure 6.2: Plot of average density parameters, $\Omega_m^{\mathcal{D}}$ and $\Omega_Q^{\mathcal{D}}$ as a function of redshift, z. The values of the parameters are chosen as: $\mu_u = 0.01$, $\sigma_u = 0.01$, $\mu_o = 0.99$ and $\sigma_o = 0.01$. The inset shows the magnified plot for $\Omega_Q^{\mathcal{D}}$, the density parameter for kinematical backreaction term $\mathcal{Q}_{\mathcal{D}}$.

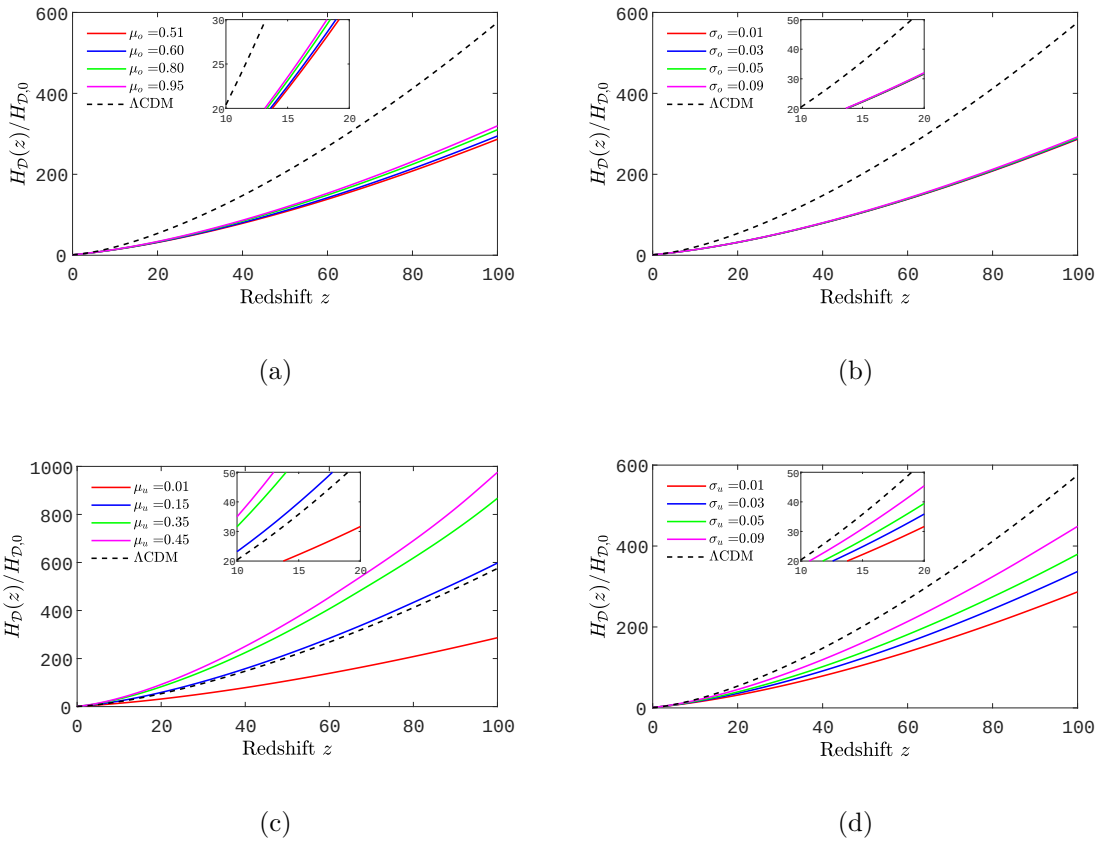

Figure 6.3: Plots of $H_{\mathcal{D}}(z)/H_{\mathcal{D},0}$ for ΛCDM and our backreaction model as a function of z. Our backreaction model has four parameters that can be varied: $\mu_u, \sigma_u, \mu_o, \sigma_o$. In (a) μ_o is varied with $\sigma_o = \sigma_u = 0.01$ and $\mu_u = 0.01$ fixed. In (b) σ_o is varied with $\mu_o = 0.51, \sigma_u = 0.01$ and $\mu_u = 0.01$ fixed. In (c), μ_u is varied with $\sigma_o = \sigma_u = 0.01$ and $\mu_o = 0.51$ fixed. In (d), σ_u is varied with $\sigma_o = 0.01, \mu_o = 0.51$ and $\mu_u = 0.01$ fixed. The insets show the plot lines for the redshift range 10-20. The value of H_0 (Hubble parameter at the present time) used is 100 h km s^{-1}Mpc^{-1} where $h = 0.7$.

In (Fig. 6.3), the variation with respect to the redshift of $H_{\mathcal{D}}(z)/H_{\mathcal{D},0}$ (here, $H_{\mathcal{D},0}$ is the value of $H_{\mathcal{D}}(z)$ at $z = 0$) for our backreaction model and for the ΛCDM model ($H(z)/H_0$ for ΛCDM, $H_0 = H(z = 0)$) are plotted. Our backreaction model has four parameters that can be varied: μ_u, σ_u, μ_o, σ_o. One of the above parameters is varied in the four sub-figures while keeping the other three fixed. From subplot (a), it can be observed that larger values of parameter μ_o result in larger values of the quantity $H_{\mathcal{D}}(z)/H_{\mathcal{D},0}$, although the variation is very less and from (c) also, it can be observed that larger values of parameter μ_u result in larger values of the quantity $H_{\mathcal{D}}(z)/H_{\mathcal{D},0}$. Let us first consider the subplot (c) where μ_u is being varied, keeping the other three parameters fixed. Since μ_u is the mean of the Gaussian distribution of $\lambda_{u_i,0}$, it corresponds to the subregion with the largest value of $\lambda_{u_i,0}$ in the distribution. The subregion with $q_{u_{i,0}} = \mu_u$ possesses the largest value of $\lambda_{u_i,0}$ and therefore, the largest value of λ_{u_i} also, from (Eq. 6.18). It follows from (Eq. 2.20) that this underdense subregion through its H_{u_i} provides the largest contribution among all other underdense subregions in the determination of H_u, the total Hubble parameter for all the underdense subregions combined, and consequently, provides the largest contribution in $H_{\mathcal{D}}$ among all other underdense subregions. Therefore, in subplot (c) with all other parameters fixed, the plotlines for $H_{\mathcal{D}}$ follow the trend of variation of H_{u_i} with respect to the redshift z, of the subregion with $q_{u_{i,0}} = \mu_u$. The higher values of $q_{u_{i,0}}$ result in higher values of $H_u(z)$ at higher values of z, which is observed in subplot (c), where higher values of μ_u give higher values of $H_{\mathcal{D}}(z)/H_{\mathcal{D},0}$. The behavior of the plotlines in subplot (a) can also be explained similarly, where the corresponding underdense subregion analysis replaces the overdense subregion analysis. In subplot (a), there is not much difference between the plotlines. This can be attributed to the fact that overdense subregions have less impact on the global domain dynamics. The reason for this is that the collective volume fraction of the overdense subregions is much smaller than the collective volume fraction of the underdense subregions.

On the other hand, from the subplots (b) and (d), it can be seen that larger values of σ_o and σ_u lead to larger values of the quantity $H_{\mathcal{D}}(z)/H_{\mathcal{D},0}$. Note that σ_o and σ_u represent the spread of the Gaussian distributions. In subplots (b) and (d), only σ_o and σ_u are varied, respectively, keeping the other three parameters fixed. Therefore, a wider distribution with the same mean is considered in subplots (b) and (d). A wider distribution results in more subregions becoming significant than for a narrower distribution. As the contributions of more subregions become effective, the values of the combined Hubble parameters for the overdense and underdense subregions, H_o and H_u, respectively, increase, and hence the value of $H_{\mathcal{D}}$ also increases, which is observed in subplots (b) and (d). Similar to the case of subplot (a), varying σ_o in subplot (b) does not have much effect on the

plotlines. Therefore, model parameters associated with the overdense subregions do not have a significant impact on the global domain dynamics.

6.4 Effect of inhomogeneities on the 21 cm brightness temperature

To analyze the brightness temperature of the 21-cm signal in the context of our model of multiple subregions of spacetime with matter distribution inhomogeneities, we replace $H(z)$ in the equations of 21-cm cosmology with $H_{\mathcal{D}}(z)$ (Fig. 6.3) which is the effective Hubble parameter calculated from our model using (Eq. 6.14). Here, we employ the general scheme to calculate the 21-cm brightness temperature T_{21} for both ΛCDM and our backreaction model. The only difference between these two models is in calculating the Hubble parameter $H(z)$, where z is the redshift. For the ΛCDM model, $H(z)$ is calculated using the standard relation of the Hubble parameter with various density parameters, Ωs. In contrast, for our model $H(z)$ is replaced by $H_{\mathcal{D}}(z)$, since we are interested in the evaluation of all physical quantities with respect to the global domain.

From (Eq. 6.1), using Taylor expansion of $e^{-\tau(z)}$, and ignoring higher order terms of $\tau(z)$, we get

$$T_{21} \approx \frac{T_s - T_\gamma}{1+z}\tau(z)$$

Now, from (Eq. 6.2), for $\delta_r v_r = 0$, $\tau(z) \propto 1/H(z)$. Therefore,

$$T_{21} \propto \frac{T_s - T_\gamma}{1+z}\frac{1}{H(z)} \tag{6.21}$$

Thus, for a given value of T_s and T_γ, T_{21} is inversely proportional to $H(z)$. Note that the sign of T_{21} is governed by T_s and T_γ. If $T_s > T_\gamma$, then T_{21} is positive and negative for vice versa. $H(z)$ has effect only on the magnitude of T_{21}. Also note that T_{21} is related to $H(z)$ via T_s, which itself depends on $H(z)$ (from (Eq. 6.4) and (Eq. 6.5)), but the dominant and more direct relationship between T_{21} and $H(z)$ is from (Eq. 6.21).

Though the primary redshift range of interest for our present analysis is $14 < z < 20$ corresponding to the range of the EDGES result [163], there are various future proposed experiments to analyze the 21 cm signal at various redshift ranges [186–190]. In Fig. 6.4, we display results for a large redshift range up to $z = 1000$, given the above-proposed observations. The current analysis focuses on a much narrower regime of $14 < z < 20$ as displayed in the figure insets.

In (Fig. 6.4), the variations of the brightness temperature T_{21} in mK as a function of redshift z (using (Eq. 6.1)) in the redshift range $14 - 1000$ are plotted for both the ΛCDM model and our backreaction model. In the case of our model,

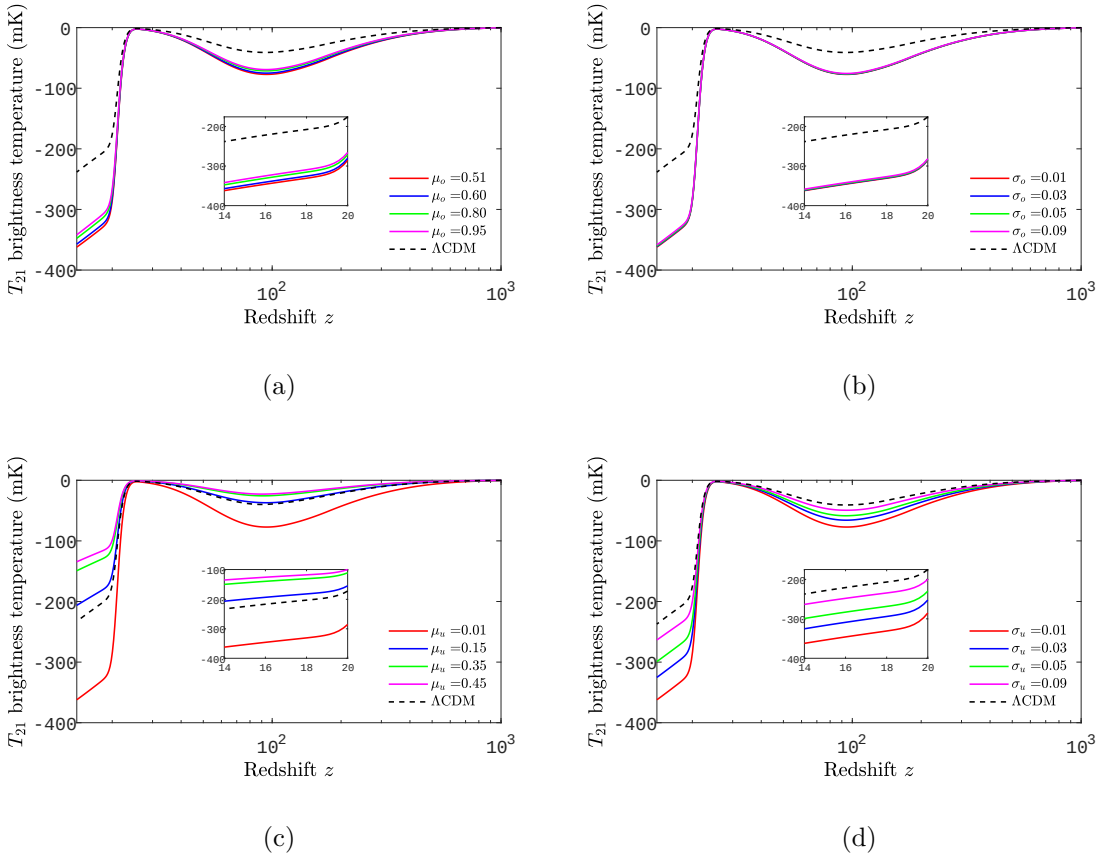

Figure 6.4: Plots of brightness temperature T_{21} for the ΛCDM model and our backreaction model for the redshift range 14 – 1000. Our backreaction model has four parameters that can be varied: $\mu_u, \sigma_u, \mu_o, \sigma_o$. In (a) μ_o is varied with $\sigma_o = \sigma_u = 0.01$ and $\mu_u = 0.01$ fixed. In (b) σ_o is varied with $\mu_o = 0.51, \sigma_u = 0.01$ and $\mu_u = 0.01$ fixed. In (c), μ_u is varied with $\sigma_o = \sigma_u = 0.01$ and $\mu_o = 0.51$ fixed. In (d), σ_u is varied with $\sigma_o = 0.01, \mu_o = 0.51$ and $\mu_u = 0.01$ fixed. The value of H_0 (Hubble parameter at the present time) used is 100 h km s^{-1}Mpc^{-1} where $h = 0.7$. The insets show the plot lines in the redshift range of our interest.

$H(z)$ is replaced by $H_{\mathcal{D}}(z)$ (plotted in (Fig. 6.3)). Our backreaction model has four parameters that can be varied: $\mu_u, \sigma_u, \mu_o, \sigma_o$. One of the parameters varied in each of the four subfigures, while the other three were fixed. Each subplot of (Fig. 6.4) has a relation with the corresponding subplot of (Fig. 6.3) via (Eq. 6.21). In subplot (c) of (Fig. 6.3), lower values of μ_u yielded lower values of $H_{\mathcal{D}}(z)$, and since $H_{\mathcal{D}}(z)$ is inversely proportional to the magnitude of T_{21}, lower values of μ_u should give us the greater magnitude of T_{21}. This is what is observed in subplot (c) of (Fig. 6.4). Other subplots of (Fig. 6.4) also have a one-to-one correspondence with their counterparts in (Fig. 6.3), which can be explained similarly. At lower values of the redshift z, our backreaction model for a large range of parameters leads to lower brightness temperature than the ΛCDM model. In general, lower values of μ_o, μ_u, σ_o and σ_u lead to lower (more negative) values of T_{21}.

In (Fig. 6.5), the variation of T_{21} at $z = 17.2$ in the $\mu_o - \sigma_o$ plane is shown for different sets of values of (μ_u, σ_u) using a contour plot. The value of μ_o varies in the range of $0.5 - 1.0$ along the x-axis, while σ_o is varied in the range $0.01 - 0.09$ along the y-axis. The contour colors describe the value of $T_{21}(z = 17.2)$ per the color bar at the bottom of the figure. In subplots (a) and (b), (μ_u, σ_u) are $(0.01, 0.01)$ and $(0.01, 0.09)$, respectively. Subplot (a) has a lower value (more negative) of $T_{21}(z = 17.2)$ compared to subplot (b). There is also very little variation within the individual subplots (a) and (b). This shows that fixing (μ_u, σ_u) and varying (μ_o, σ_o) has very little effect on the calculation of T_{21} at $z = 17.2$. However, changing σ_u between subplots (a) and (b) results in significant variation. This also shows the insignificance of the model parameters associated with overdense subregions in the dynamics of the global domain. From subplots (c) and (d), it can be seen that $T_{21}(z = 17.2)$ has high values (from -150 mK to -110 mK) for $(\mu_u, \sigma_u) = (0.45, 0.01)$ and $(0.45, 0.09)$. Changing σ_u from 0.01 to 0.09 while keeping μ_u fixed in (c) and (d) has little effect on the value of $T_{21}(z = 17.2)$. In these subplots, $T_{21}(z = 17.2)$ has the lowest value of around -350 mK in the lower left portion of the subplot (a). This affirms our analysis of (Fig. 6.4) that lower values of σ_u, σ_o, μ_o and μ_u lead to lower values (more negative) of $T_{21}(z = 17.2)$. From subplots (a) and (c), it can be seen that changing the value of μ_u keeping σ_u fixed has a more prominent effect on the brightness temperature than vice versa.

In (Fig. 6.6), the variation of T_{21} at $z = 17.2$ in the $\mu_u - \sigma_u$ plane is shown for different sets of values of (μ_o, σ_o) using a contour plot. The value of μ_u varies in the range of $0 - 0.5$ along the x-axis while σ_u is varied along the y-axis in the range of $0.01 - 0.09$. In subplots (a) and (b) of the figure, μ_o is fixed at 0.51, and σ_o has the values of 0.01 and 0.09, respectively. In subplots (c) and (d) of the figure, μ_o is fixed at 0.99 while σ_u has the values of 0.01 and 0.09, respectively. The effect of varying σ_o while keeping μ_o fixed can also be seen from these two subplots. From subplots (a) and (c), it can be seen that changing the value of μ_o, keeping

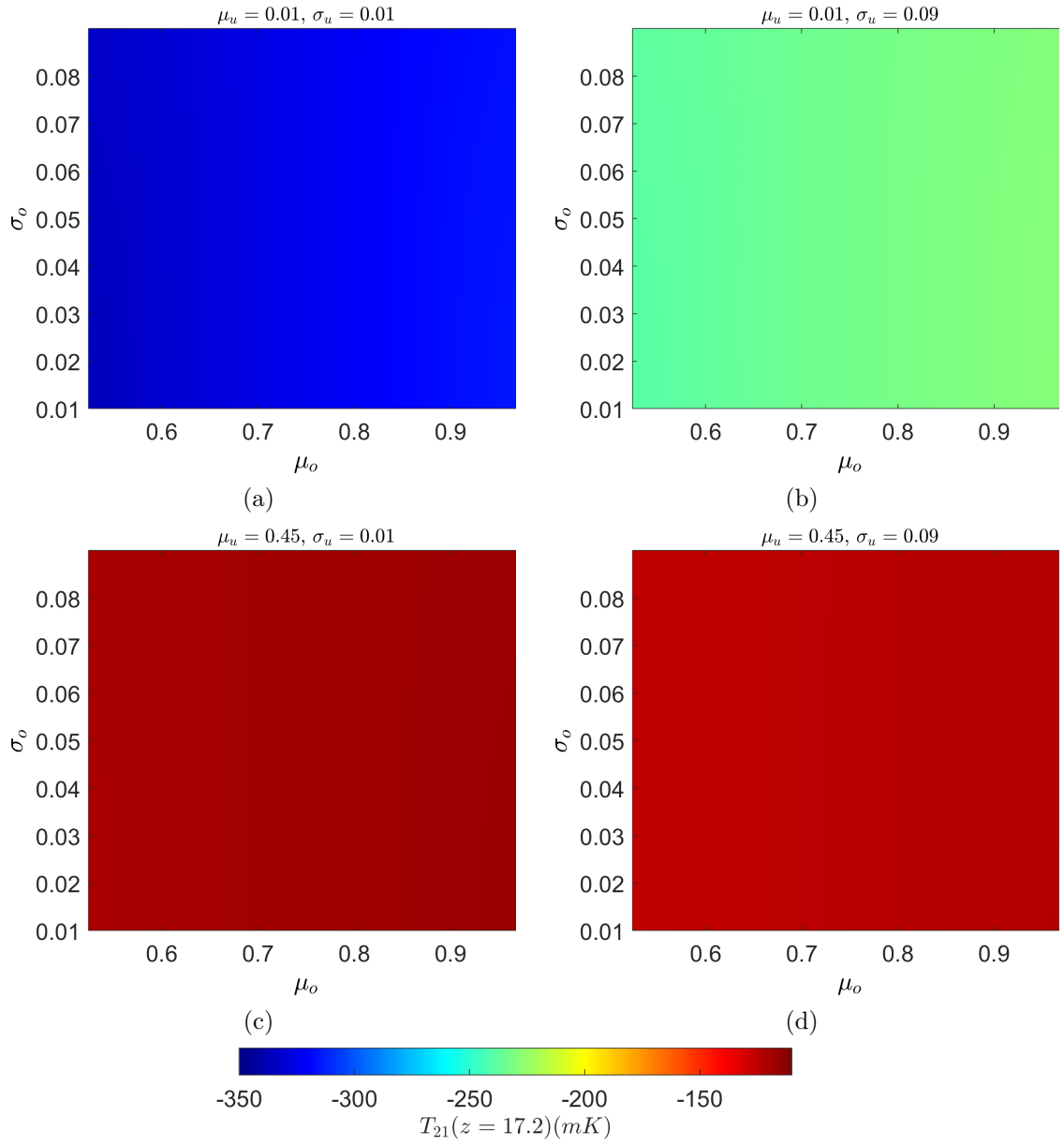

Figure 6.5: Contour representation of $T_{21}(z = 17.2)(mK)$ in the $\sigma_o - \mu_o$ plane for (a) $\mu_u = 0.01$, $\sigma_u = 0.01$ (b) $\mu_u = 0.01$, $\sigma_o = 0.09$, (c) $\mu_u = 0.45$, $\sigma_u = 0.01$, (d) $\mu_u = 0.45$, $\sigma_u = 0.09$.

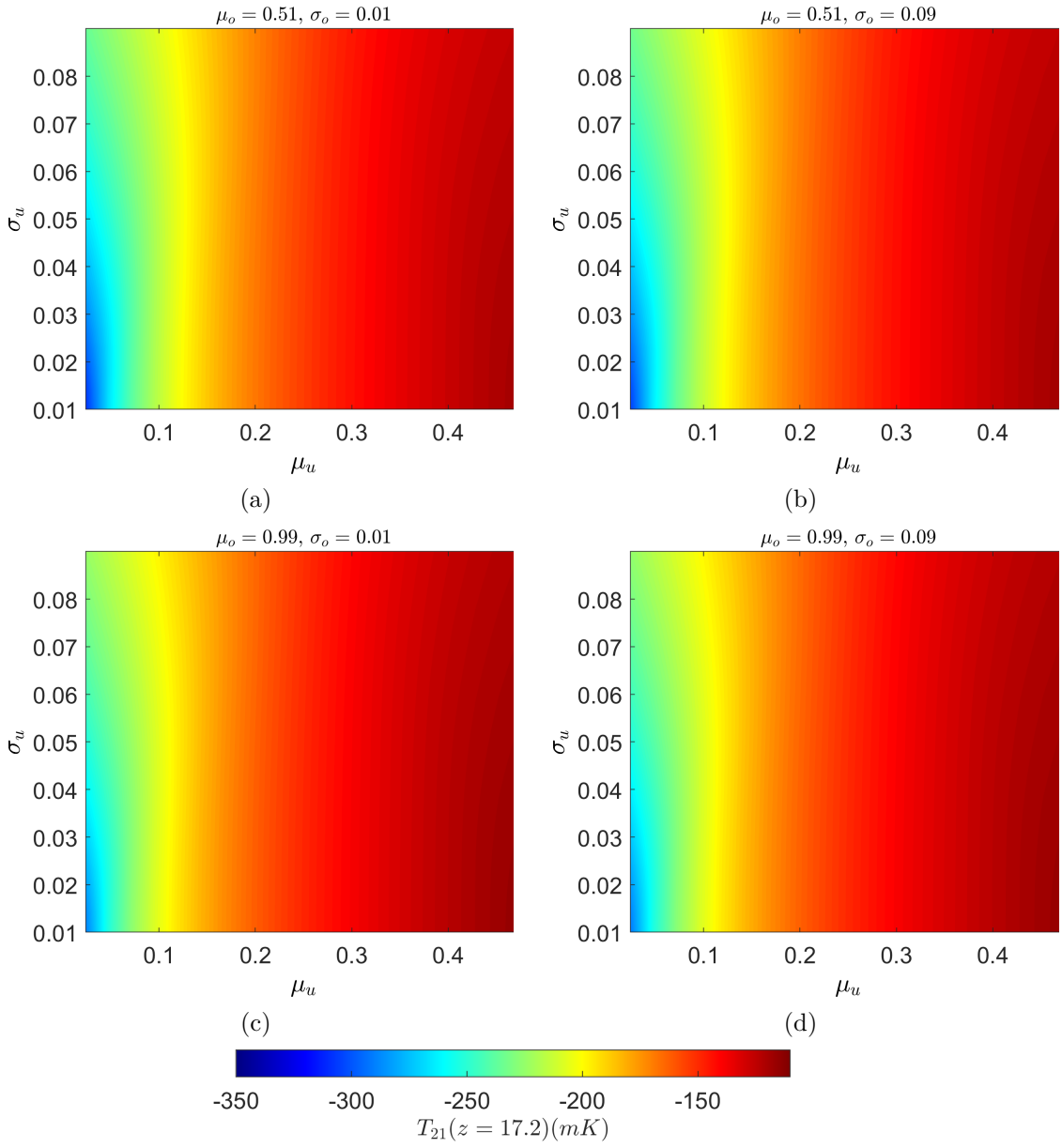

Figure 6.6: Contour representation of $T_{21}(z = 17.2)$ (mK) in $\sigma_u - \mu_u$ plane for (a) $\mu_o = 0.51$, $\sigma_o = 0.01$ (b) $\mu_o = 0.51$, $\sigma_o = 0.09$, (c) $\mu_o = 0.99$, $\sigma_o = 0.01$, (d) $\mu_o = 0.99$, $\sigma_o = 0.09$.

σ_o fixed, has a slightly more prominent effect on the brightness temperature than vice versa. The lowest value of $T_{21}(z = 17.2)$ of around -320 mK is obtained in the bottom left part of the subplot (a) of the figure for $\mu_u \approx 0.01$. This also affirms our analysis of (Fig. 6.4) that lower values of σ_u, σ_o, μ_o and μ_u lead to lower values (more negative) of $T_{21}(z = 17.2)$. This figure also highlights the insignificance of overdense parameters, as all four subplots are very much alike, so changing the overdense parameters does not affect the output much.

6.5 Observational Constraints

We now examine the backreaction framework in the context of our model of multiple subregions with respect to observational data and determine the optimum values of our model parameters. We perform a Bayesian analysis to compare our model with the Union2.1 supernova Ia distance modulus versus redshift data [155]. To compare our model with the observational data, we employ the earlier-mentioned (Sec. 2.2) covariant scheme (Eq. 2.25, Eq. 2.26). The first equation of the covariant scheme (Eq. 2.25) relates the theoretically calculated quantity from our model $a_{\mathcal{D}}$ with the cosmological redshift, z, and the second equation (Eq. 2.26) relates the theoretically calculated quantity from our model $\langle\rho\rangle_{\mathcal{D}}$ with the observational quantity, the angular diameter distance D_A. From this D_A, we can calculate the distance modulus using standard cosmological distance relations and thus compare our model with the Union2.1 supernova Ia data.

In this analysis, the resulting posterior distributions of different parameters are obtained by the Markov Chain Monte Carlo (MCMC) iteration method (Fig. 6.7) by using the `MCMCSTAT` package [91, 92]. We use a total of 3×10^3 number of events with the adaptation interval of 100, within the parameter range: $\mu_u \in [0.01, 0.49]$, $\sigma_u \in [0.01, 0.09]$, $\mu_o \in [0.51, 0.99]$ and $\sigma_o \in [0.01, 0.09]$. The topmost plots of the first, second, third and fourth columns of (Fig. 6.7) represent the posterior distribution of the parameters μ_u, σ_u, μ_o and σ_o, respectively, obtained by marginalizing the other parameters. The other plots of (Fig. 6.7) show the contour representation of the posterior distribution in different sets of a two-parameter space. In these contour plots, the darker-coloured regions denote higher posterior regions, and the lines indicate the boundaries of 1σ, 2σ and 3σ regions, respectively. The diagonal panels show the 1-D histogram of the posterior distribution for each model parameter obtained by marginalizing the other parameters. The off-diagonal panels show 2-D projections of the posterior probability distributions for each pair of parameters and correlations between the parameters and contours.

From this analysis the obtained set of optimum points are $\mu_u = 0.01^{+0.00}_{-0.00}$, $\sigma_u = 0.01^{+0.00}_{-0.00}$, $\mu_o = 0.63^{+0.16}_{-0.08}$ and $\sigma_o = 0.05^{+0.03}_{-0.03}$ respectively. These optimum points are obtained considering all four parameters. However, from the marginal-

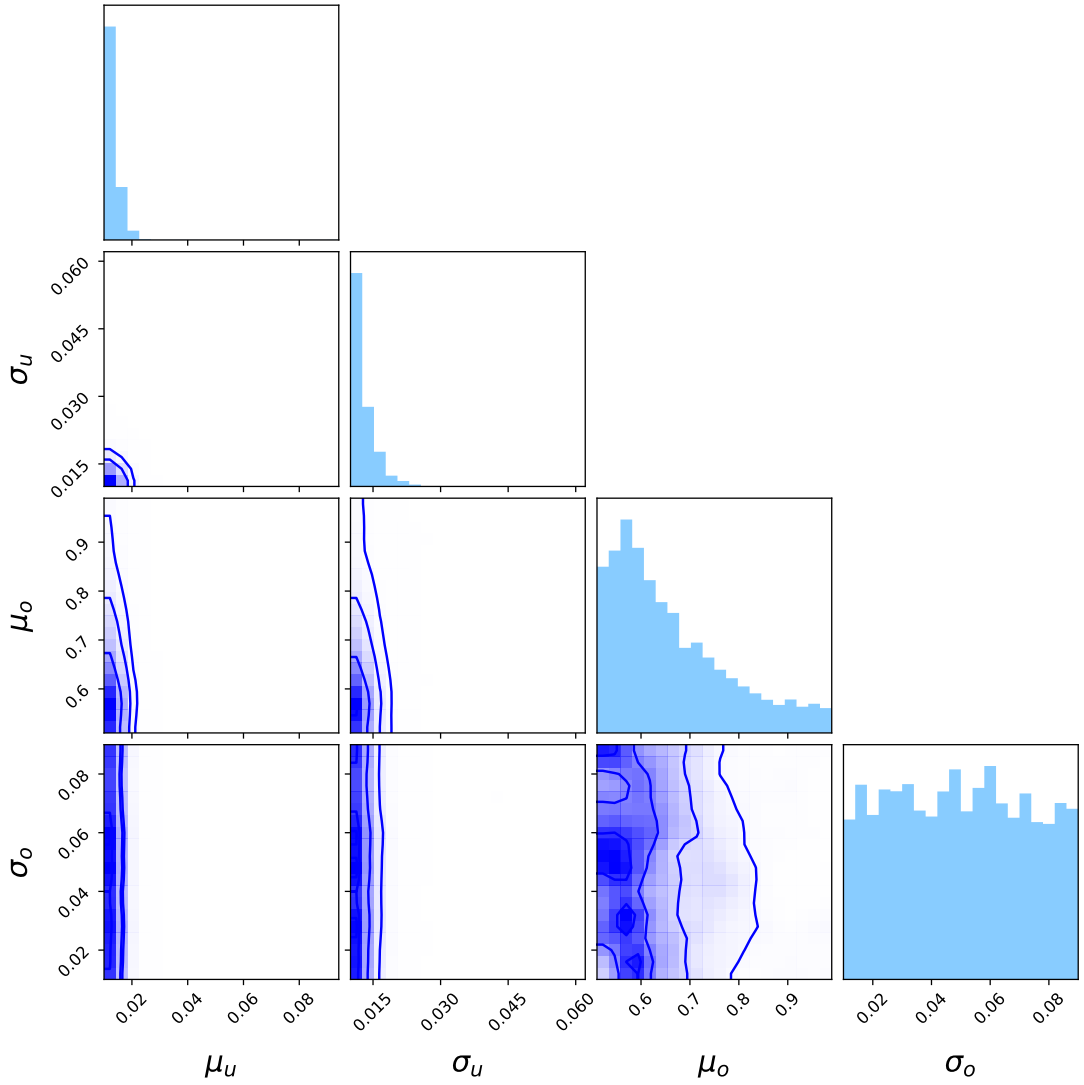

Figure 6.7: Corner plot showing the MCMC result for our model carried out using the observational results of the Union2.1 supernova Ia data [155]. The diagonal histograms show the marginalized posterior densities for each parameter.

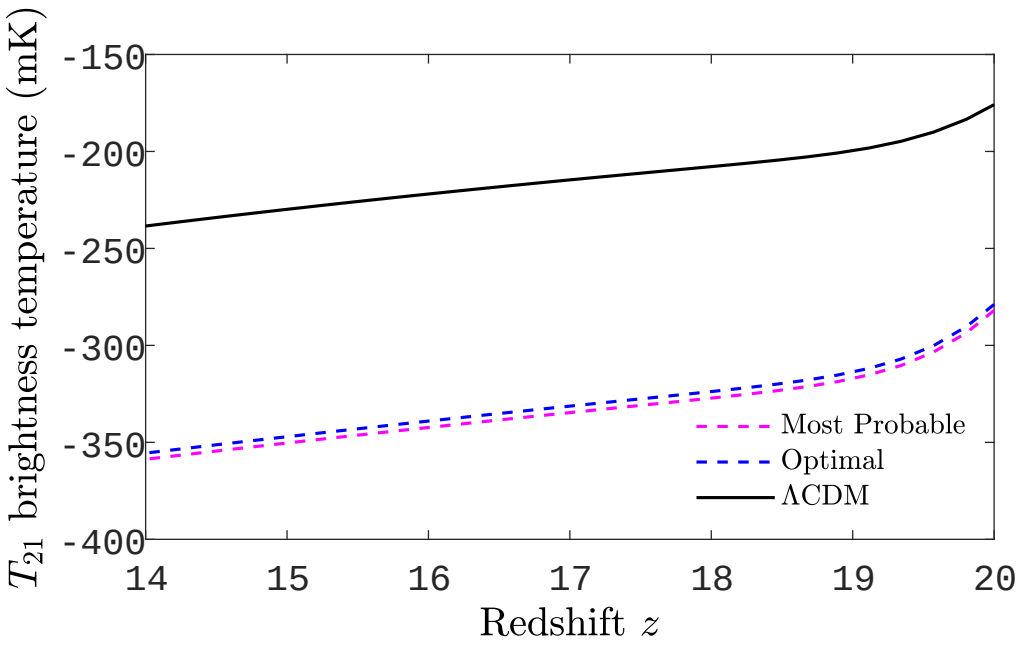

Figure 6.8: Plots of brightness temperature T_{21} (mK) for the ΛCDM model and our backreaction model for the optimal values and the most probable values of our model parameters obtained from the MCMC analysis for the redshift range 14-20. Dashed plotlines are for our backreaction model.

ized posterior plot for μ_o (in (Fig. 6.7)), one can notice that the most probable value of μ_o is slightly lower ($\mu_o = 0.55$) than the corresponding optimal point. This is because posterior plots for each parameter plotted along the diagonal are obtained by marginalizing the other parameters. These plots do not consider other parameters; therefore, the most probable values differ from the optimum values. Similarly, the most probable values for other model parameters are $\mu_u = 0.01$, $\sigma_u = 0.01$ and $\sigma_o = 0.06$. It can be seen that lower values of σ_u, μ_u and μ_o are favored, which in turn favors a reduced brightness temperature of the T_{21} signal, as determined from our analysis of (Fig. 6.4 - Fig. 6.6).

In (Fig. 6.8), the brightness temperature T_{21} is plotted in units of mK as a function of redshift z in the range $14-20$ for the ΛCDM model and for the optimal and most probable values of the parameters of our backreaction model, obtained from the MCMC analysis. The set of optimal values used is $(\mu_u, \sigma_u, \mu_o, \sigma_o) = (0.01, 0.01, 0.63, 0.05)$ and the set of most probable value used is $(\mu_u, \sigma_u, \mu_o, \sigma_o) = (0.01, 0.01, 0.55, 0.06)$. Both the most probable and optimal sets of values gives a brightness temperature considerably lower than the ΛCDM model for this redshift range. At $z = 14$, T_{21} for our backreaction model, the optimal and most probable set of parameter values is around $\approx -350mK$ which is within the range of the

EDGES result. This value is lower than the ≈ -240mK given by the ΛCDM model.

6.6 Conclusions

Recent observations indicate that our Universe contains an inhomogeneous matter distribution at considerably large scales [8–10]. The effect of these inhomogeneities on various cosmological phenomena calls for close scrutiny. In the present study, we revisit the 21-cm cosmology [158–160], in a spacetime with matter distribution inhomogeneities. We explore the brightness temperature of the 21-cm signal as a function of the redshift under the impact of backreaction from matter inhomogeneities.

In our analysis, we use the widely used Buchert formalism [25] (Sec. 2.1) of averaging over inhomogeneities to evaluate the backreaction effect. The Buchert framework facilitates the relation of theoretically evaluated quantities with observables such as redshift and angular diameter distance [33–37]. Within this framework, we construct a model of multiple subregions with a Gaussian distribution of parameters to mimic the actual Universe containing multiple voids and structures at the present epoch. We employ the covariant scheme to relate our theoretically evaluated parameters to observational quantities.

Using this model, we calculate the brightness temperature T_{21} of the 21-cm signal as a function of the redshift and analyze it for our model parameters. Such a model of spacetime that we have employed leads to a modification of the Hubble evolution, making it desirable to constrain our model parameters using observational results. To correlate our model with observation data, we obtain the marginalized posterior densities for each model parameter through Markov Chain Monte Carlo (MCMC) simulations using Union2.1 supernova Ia data [155].

Our analysis shows that the 21-cm brightness temperature T_{21} could be lowered by a significant amount under the impact of altered Hubble evolution resulting from backreaction from matter distribution inhomogeneities. Such a result follows without utilizing any exotic physics or non-standard models of dark matter and dark energy, such as schemes employed in a host of previous works [128, 166–172] to lower the 21-cm brightness temperature. In particular, using the optimal and most probable values of our model parameters obtained through the MCMC simulations, it can be seen that T_{21} could drop to levels below the predictions of ΛCDM and within the range of the EDGES result.

We conclude by noting that several earth-based and space-based experiments have been proposed to observe and record the 21-cm signal effectively [186–190]. Our analysis obtains the evolution of T_{21} over a wide range of redshift z in (Fig. 6.4). Thus, it can be used in conjunction with data from such ex-

periments to analyze the role of matter distribution inhomogeneities in 21-cm cosmology. Specifically, if any dip in temperature below the ΛCDM prediction is observed in the 21-cm signal, our present analysis should motivate further detailed investigations of other backreaction scenarios [13, 19, 21–23], as well.

Chapter 7

Summary and future outlook

This thesis explores how inhomogeneous distributions of matter in the Universe affect various astrophysical and cosmological phenomena. We applied Buchert's averaging method to incorporate these inhomogeneities into our study. Initially, we developed simple two-domain spacetime models featuring inhomogeneous matter distribution, which gradually evolved into more complex and realistic multidomain models. In two chapters of our work (Chap. 5 and Chap. 6), we also employed observational data from the Union2.1 redshift vs. distance modulus dataset (Sec. 2.4) to constrain our model parameters through MCMC analysis (Sec. 2.5). Each of our studies generates verifiable predictions that can be evaluated using future observational data.

In (Chap. 3), we explored how gravitational waves emitted by compact binary systems propagate through a background spacetime in the presence of matter distribution inhomogeneities. To address the impact of these inhomogeneities, we utilized Buchert's backreaction framework, incorporating a simplified two-partition model. This analysis results in a modification in the relationship between redshift and distance. Our findings reveal a significant divergence in the variation of the redshift-dependent part of the amplitude of gravitational waves when comparing (i) the ΛCDM model and (ii) our model based on Buchert's backreaction approach. This deviation grows with the increasing influence of inhomogeneities, which is measured through volume fractions and the expansion rate of voids.

In (Chap. 4), we explored the behavior of gravitational waves originating from compact binary systems as they traverse a viscous, inhomogeneous Universe. This study is based on a model employing the averaging procedure for scalars according to Buchert's backreaction framework. Within this framework, the relationship between redshift and distance diverges from predictions by the ΛCDM model, with variations depending on specific model parameters. We have assumed that the matter within the overdense regions of our inhomogeneous spacetime model exhibits viscosity, resulting in an attenuation of the amplitude of gravitational

waves as they pass through these areas. By incorporating the effects of viscous attenuation into our model, we've derived a formula illustrating the redshift-dependent changes in the wave amplitude. Our findings reveal that accounting for viscous attenuation leads to a significant discrepancy in the redshift-related amplitude of gravitational waves, as opposed to scenarios where the role of viscosity is minimal or absent. Therefore, including the impact of viscosity on gravitational wave observations from compact binaries is crucial when considering local inhomogeneities in the Universe.

In (Chap. 5), we developed a multi-domain spacetime model featuring an inhomogeneous distribution of matter. The model divides into two main categories of subregions: overdense and underdense, each with unique evolution dynamics. Utilizing the Buchert formalism, we evaluated the averaged backreaction effects of these inhomogeneities on the Universe's global evolution at late times. Our findings reveal a decrease in global acceleration after the present epoch across a substantial range of model parameter values. We demonstrated that beyond a certain time point (t_{dec}), the global acceleration parameter may turn negative, indicating a transition from the current accelerating phase to one of future deceleration. We also optimized our model for the maximum number of subregions to be considered for a reliable result for future global evolution. The dependence of the deceleration time (t_{dec}) on the various model parameters was analyzed systematically, indicating that parameters linked to underdense regions notably influence the timing of this transition. We further correlated our model with observational data, using Markov Chain Monte Carlo (MCMC) simulations with the Union 2.1 supernova Ia dataset to obtain marginalized posterior densities for each parameter.

In (Chap. 6), we revisit the 21-cm cosmology considering spacetime with an inhomogeneous matter distribution. We study the 21-cm signal's brightness temperature as a function of redshift under the influence of the backreaction of these matter distribution inhomogeneities. Our investigation employs the Buchert formalism to average over inhomogeneities to calculate the backreaction effect. Within this framework, we develop a model featuring multiple subregions with a Gaussian parameter distribution to mimic our Universe, which comprises numerous voids and structures at the current era. We use the covariant scheme to connect our theoretical parameters to observable data. With this model, we determine and examine the brightness temperature T_{21} of the 21-cm signal as a function of redshift corresponding to our model parameters. The spacetime model adopted here modifies the Hubble evolution, necessitating the use of observational data to constrain our model parameters. Compared with observational data, we derive marginalized posterior densities for each parameter using Markov Chain Monte Carlo (MCMC) simulations with Union 2.1 supernova Ia data. Our

findings indicate that the 21-cm brightness temperature T_{21} may significantly decrease due to modified Hubble evolution driven by backreaction from inhomogeneous matter distribution. This conclusion emerges without resorting to exotic physics or unconventional dark matter and energy models that are often used in earlier studies to reduce the 21-cm brightness temperature. Notably, according to the optimal and most probable parameter values obtained via MCMC simulations, T_{21} can decrease to levels beneath the predictions of the ΛCDM model, aligning with the EDGES result.

The present thesis leaves open some important questions and possibilities for further study.

This thesis exclusively uses Buchert's averaging procedure and related frameworks. The analysis done here can be done with other averaging procedures and other frameworks.

In (Chap. 5 and Chap. 6), we have used a Gaussian distribution for distributing our model parameters across the multiple subregions. But the actual distribution in the Universe may not be Gaussian. The actual distribution may be revealed with extensive future galactic surveys. These analyses can be redone by employing a more realistic distribution, keeping the results of these surveys in mind.

In (Chap. 5 and Chap. 6), we have used the Union2.1 distance modulus vs redshift dataset to constrain our model parameters using MCMC analysis. These constraints can be updated by using more recent and more extensive datasets.

In (Chap. 6), we have demonstrated that using our model and backreaction framework, T_{21} for the 21 cm signal can be constrained within the EDGES reported range. However, the subsequent SARAS experiment has failed to detect the EDGES 21 cm signal. So, we have to wait for future reporting of 21 cm signal observations for clarity of the situation.

The averaging procedure, framework, along with the model of spacetime with inhomogeneous matter distribution employed in this thesis, can also be used to analyze Hubble tension.

Appendix A

GWs in the presence of viscosity

GWs are affected by the viscosity of the propagating medium [108–114]. It was shown [108] that only the coefficient of shear viscosity has any influence on the attenuation of GW.

Here, we discuss some essential steps in the derivation of the attenuation factor of a GW propagating through a viscous fluid in an FRW Universe. The same relation of the attenuation factor is also valid for our backreaction models, incorporating the redshift-distance relation given by the covariant scheme. We use the mechanism employed by [113]. The general form of the energy-momentum tensor for a non-ideal fluid is given by [113, 136],

$$T_{\mu\nu} = (\rho + p)u_\mu u_\nu + p g_{\mu\nu} - 2\eta\sigma_{\mu\nu} - \xi\theta\Delta_{\mu\nu} \tag{A.1}$$

where ρ is the density of the fluid, p is the pressure of the fluid, u_μ is the fluid four velocity, $g_{\mu\nu}$ is the metric tensor, η is the coefficient of shear viscosity, $\sigma_{\mu\nu}$ is the shear, ξ is the coefficient of bulk viscosity, θ is the volume expansion of the fluid and $\Delta_{\mu\nu}$ is the projection tensor on the subspace normal to u_μ and it is given by the relation, $\Delta_{\mu\nu} = g_{\mu\nu} + u_\mu u_\nu$. Throughout, $\hbar = c = 1$.

Next, we consider tensor perturbations in the background FRW metric,

$$ds^2 = -dt^2 + a^2(t)[\delta_{ij} + h_{ij}]dx^i dx^j, \tag{A.2}$$

The tensor perturbations are considered in the transverse and traceless gauge, $\partial^i h_{ij} = h^i_i = 0$.

The total four-velocity is given by $u_\mu = u^{(0)}_\mu + \partial u_\mu$. Normalizing the four-velocity, considering only up to first-order terms in the metric and velocity perturbations, and going to the rest frame of the fluid, the velocity perturbations ∂u^μ vanish. In the rest frame of the fluid, we have,

$$\theta = 3H \tag{A.3}$$

$$\sigma_{ij} = \frac{1}{2}a^2\dot{h}_{ij}, \tag{A.4}$$

where H is the Hubble parameter and dot denotes derivative with respect to cosmic time t.

Einstein's equation in zeroth order in h_{ij}, $G_{ij} = 8\pi G T_{ij}$ and in first order in h_{ij}, $\partial G_{ij} = 8\pi G T_{ij}$ gives us the wave equation for GWs in a viscous fluid,

$$\ddot{h}_{ij} + (3H + 16\pi G\eta)\dot{h}_{ij} - \frac{\nabla^2}{a^2}h_{ij} = 0 \tag{A.5}$$

ξ doesn't come into (Eq. A.5) as it only couples to scalar perturbations.

Next, performing the Fourier transform of (Eq. A.5) and defining h_{ij} as μ_{ij}/a one gets,

$$\ddot{\mu}_{ij} + (H + 16\pi G\eta)\dot{\mu}_{ij} + \left(\frac{k^2}{a^2} - \frac{\ddot{a}}{a} - H^2 - 16\pi G\eta H\right)\mu_{ij} = 0 \tag{A.6}$$

Defining conformal time τ as $dt = ad\tau$ and using it in (Eq. A.6) leads to

$$\mu_{ij}'' + 16\pi G\eta a\mu_{ij}' + \left(k^2 - \frac{a''}{a} - 16\pi G\eta a\mathcal{H}\right)\mu_{ij} = 0 \tag{A.7}$$

where $'$ denotes derivatives with respect to τ. On sub-horizon scales $k^2 >> \frac{a'}{a}$, (Eq. A.7) reduces to,

$$\mu_{ij}'' + 16\pi G\eta a\mu_{ij}' + k^2\mu_{ij} = 0. \tag{A.8}$$

Let $A_{\times,+} = r\mu_{ij}$ represent the amplitude of the two polarization modes $\times$ and $+$ of the radial component of the wave. Then, at large distances from the source, A satisfies the following 1-D wave equation,

$$\ddot{A} + \beta a\dot{A} + k^2 A = 0 \tag{A.9}$$

where $\beta \equiv 16\pi G\eta$. Assuming the solution of (Eq. A.9) is of the form,

$$A(\tau, \omega) = \tilde{A}(\omega)e^{ikr - \int i\omega d\tau}. \tag{A.10}$$

and substituting (Eq. A.10) in (Eq. A.9), gives us the dispersion relation,

$$-\omega^2 - i\beta a\omega + k^2 = 0 \tag{A.11}$$

Separating the real and imaginary part of k, $k = k_R + ik_I$, (Eq. A.11) in conjugation with the weak damping approximation $\beta << \omega$, and keeping only the leading order terms gives us,

$$\begin{aligned} k_R &= \omega \\ k_I &= \frac{\beta a}{2} \end{aligned} \tag{A.12}$$

The presence of the imaginary part of k, k_I, results in attenuation of the wave. (Eq. A.10) now becomes,

$$A(\tau, \omega) = \tilde{A}(\omega) e^{ik_R r - \int i\omega d\tau} \times e^{-k_I r}. \tag{A.13}$$

The strain h_{ij} of the GW in cosmic time t now becomes,

$$h_{ij} = \frac{\tilde{A}(\omega(t))}{L_0} e^{ik_R r - \int i\omega_p dt} \times \frac{L_0 e^{-\frac{\beta}{2}L}}{L} \tag{A.14}$$

where $L = ar$ is the source distance, L_0 is the source distance for zero shear viscosity and $\omega_p = \frac{\omega}{a}$ is the physical angular frequency. Therefore, the attenuation factor is given by $\frac{L_0 e^{-\frac{\beta}{2}L}}{L}$ where $\beta \equiv 16\pi G\eta$.

Appendix B

Calculation of t_0

Using (Eq. 2.20), we can break down H_D as,

$$H_{\mathcal{D}} = \sum_i \lambda_{o_i} H_{o_i} + \sum_j \lambda_{u_j} H_{u_j} = \lambda_o H_o + \lambda_u H_u, \tag{B.1}$$

where, $\lambda_o H_o = \sum_i \lambda_{o_i} H_{o_i}$ represents the collective contribution of overdense subregions, and similarly $\lambda_u H_u = \sum_i \lambda_{u_i} H_{u_i}$ represents the collective contribution of underdense subregions. Also, using (Eq. 2.23), we can write,

$$a_{\mathcal{D}}^3 = \lambda_{o,0} a_o^3 + \lambda_{u,0} a_u^3 \tag{B.2}$$

where, $\lambda_{o,0} a_o^3$ represents the collective contribution of the overdense subregions and similarly $\lambda_{u,0} a_u^3$ for the underdense subregions. Using (Eq. 6.15), (Eq. B.1) can be written as

$$\begin{aligned} H_{\mathcal{D}} &= \lambda_{o,0} \frac{a_o^3}{a_{\mathcal{D}}^3} H_o + \lambda_{u,0} \frac{a_u^3}{a_{\mathcal{D}}^3} H_u \\ &= H_o \left(\frac{\lambda_{o,0} a_o^3}{\lambda_{o,0} a_o^3 + \lambda_{u,0} a_u^3} + \frac{\lambda_{u,0} a_u^3}{\lambda_{o,0} a_o^3 + \lambda_{u,0} a_u^3} \frac{H_u}{H_o} \right) \\ &= H_o (1 - v + vh), \end{aligned} \tag{B.3}$$

where, using the definitions of h and v from [54], we have defined similarly $h := H_u/H_o$ and $v := \frac{\lambda_{u,0} a_u^3}{\lambda_{o,0} a_o^3 + \lambda_{u,0} a_u^3}$. Our definition of v is different from theirs due to the different scaling of $a_{\mathcal{D}}$ that we have used here. Therefore,

$$H_{\mathcal{D}} = H_o (1 - v + vh) = \frac{\sum_i \lambda_{o_i} H_{o_i}}{\lambda_o} (1 - v + vh) \tag{B.4}$$

Now, using (Eq. 6.8) and (Eq. 6.9),

$$H_{o_i} = \frac{\sin \phi_{o_i} (\phi_{o_i} - \sin \phi_{o_i})}{t_0 (1 - \cos \phi_{o_i})^2} \tag{B.5}$$

Therefore,

$$H_{\mathcal{D}} = \frac{1}{\lambda_o t_0}(1 - v + vh) \sum_i \lambda_{o_i} \frac{\sin\phi_{o_i}(\phi_{o_i} - \sin\phi_{o_i})}{(1 - \cos\phi_{o_i})^2} \tag{B.6}$$

At present time, t_0,

$$H_{\mathcal{D}_0} = \frac{1}{\lambda_{o,0} t_0}(1 - v_0 + v_0 h_0) \sum_i \lambda_{o_{i,0}} \frac{\sin\phi_{o_{i,0}}(\phi_{o_{i,0}} - \sin\phi_{o_{i,0}})}{(1 - \cos\phi_{o_{i,0}})^2} \tag{B.7}$$

We see that,

$$t_0 = \frac{1}{\lambda_{o,0} H_{\mathcal{D}_0}}(1 - v_0 + v_0 h_0) \sum_i \lambda_{o_{i,0}} \frac{\sin\phi_{o_{i,0}}(\phi_{o_{i,0}} - \sin\phi_{o_{i,0}})}{(1 - \cos\phi_{o_{i,0}})^2} \tag{B.8}$$

so we need to fix either t_0 or $H_{\mathcal{D}_0}$. Here, we have chosen $H_{\mathcal{D}_0} = 70$ km/s/Mpc. Now, we have,

$$v_0 = \frac{\lambda_{u,0} a_{u,0}^3}{\lambda_{o,0} a_{o,0}^3 + \lambda_{u,0} a_{u,0}^3}; \qquad h_0 = \frac{H_{u,0}}{H_{o,0}}$$

We have defined our model in such a way that, $a_{o,0} = a_{u,0} = a_{\mathcal{D},0} = 1$. Also, $(\lambda_{o,0}, \lambda_{u,0}) = (0.09, 0.91)$ [27]. Therefore, $v_0 = 0.91$. Also,

$$\begin{aligned} \lambda_o H_o = \sum_i \lambda_{o_i} H_{o_i} \implies H_o &= \frac{1}{\lambda_o} \sum_i \lambda_{o_i} H_{o_i} \\ \implies H_{o,0} &= \frac{1}{\lambda_{o,0}} \sum_i \lambda_{o_i,0} H_{o_{i,0}} \\ = \frac{1}{\lambda_{o,0} \times t_0} \sum_i \left(\frac{N_o}{\sigma_o \sqrt{2\pi}} e^{-(q_{o_{i,0}} - \mu_o)^2 / 2\sigma_o^2} \times \frac{\sin\phi_{o_{i,0}}(\phi_{o_{i,0}} - \sin\phi_{o_{i,0}})}{(1 - \cos\phi_{o_{i,0}})^2} \right) & \end{aligned} \tag{B.9}$$

where we have used (Eq. 6.17). Similarly, using (Eq. 6.10), (Eq. 6.11) and (Eq. 6.16), we get the following,

$$H_{u,0} = \frac{1}{\lambda_{u,0} \times t_0} \sum_i \left(\frac{N_u}{\sigma_u \sqrt{2\pi}} e^{-(q_{u_{i,0}} - \mu_u)^2 / 2\sigma_u^2} \times \frac{\sinh\phi_{u_{i,0}}(\sinh\phi_{u_{i,0}} - \phi_{u_{i,0}})}{(\cosh\phi_{u_{i,0}} - 1)^2} \right) \tag{B.10}$$

The t_0 term in the denominators of (Eq. B.9) and (Eq. B.10) cancels out and all the other quantities are known. Therefore, we have,

$$h_0 = \frac{H_{u,0}}{H_{o,0}} = \frac{\lambda_{o,0}}{\lambda_{u,0}} \frac{\sum_i \left(\frac{N_u}{\sigma_u \sqrt{2\pi}} e^{-(q_{u_{i,0}} - \mu_u)^2 / 2\sigma_u^2} \times \frac{\sinh\phi_{u_{i,0}}(\sinh\phi_{u_{i,0}} - \phi_{u_{i,0}})}{(\cosh\phi_{u_{i,0}} - 1)^2} \right)}{\sum_i \left(\frac{N_o}{\sigma_o \sqrt{2\pi}} e^{-(q_{o_{i,0}} - \mu_o)^2 / 2\sigma_o^2} \times \frac{\sin\phi_{o_{i,0}}(\phi_{o_{i,0}} - \sin\phi_{o_{i,0}})}{(1 - \cos\phi_{o_{i,0}})^2} \right)} \tag{B.11}$$

So, from (Eq. B.11), we can calculate h_0 and then using this value of h_0 and v_0 in (Eq. B.8), we can obtain t_0. In this way, using the above procedure, we can fix t_0 for a given set of values of our model parameters $(\mu_u, \sigma_u, \mu_o, \sigma_o)$.

Appendix C

Our multidomain model

Our multidomain model is made up of multiple subdomains of overdense and underdense. The underdense subdomains are negatively curved FLRW regions, while the overdense subdomains are positively curved FLRW regions having densities greater than those of the underdense subdomains. Both of these subregions are composed of dust. Now, the scale factor for these overdense and underdense subdomains as functions of cosmic time t is given by (Eq. 6.8, Eq. 6.9) and (Eq. 6.10, Eq. 6.11) respectively.

The densities of underdense subregions are given by [136],

$$\rho_{u_i} = \frac{\rho_{u_{i,0}}}{a_{u_i}^3} \tag{C.1}$$

where $\rho_{u_{i,0}}$ is the density at present time t_0, which is given by,

$$\frac{\rho_{u_{i,0}}}{\rho_{u_{i,c}}} = q_{u_{i,0}}; \quad \text{where} \quad \rho_{u_{i,c}} = \frac{3H_{u_i,0}^2}{8\pi G} \tag{C.2}$$

where $\rho_{u_{i,c}}$ is the critical density and $H_{u_i,0}$ is the value of present time Hubble parameter for the i^{th} underdense subregion.

Densities for the overdense subregions can also be defined similarly,

$$\rho_{o_i} = \frac{\rho_{o_{i,0}}}{a_{o_i}^3} \tag{C.3}$$

where $\rho_{o_{i,0}}$ is the density at present time t_0, which is given by,

$$\frac{\rho_{o_{i,0}}}{\rho_{o_{i,c}}} = q_{o_{i,0}}; \quad \text{where} \quad \rho_{o_{i,c}} = \frac{3H_{o_i,0}^2}{8\pi G} \tag{C.4}$$

where $\rho_{o_{i,c}}$ is the critical density and $H_{o_i,0}$ is the value of present time Hubble parameter for the i^{th} overdense subregion.

Choosing our parameters in the range $0 < q_{u_{i,0}} < 0.5$ and $1/2 < q_{o_{i,0}} < 1$, it follows from Eq. C.2 and Eq. C.4 that the densities of underdense subdomains

remain always less than the densities of overdense subdomains.

The combined density for all overdense subregions (ρ_o) is given by,

$$\lambda_o \rho_o = \sum_i \lambda_{o_i} \rho_{o_i} \implies \rho_o = \frac{\sum_i \lambda_{o_i} \rho_{o_i}}{\sum_i \lambda_{o_i}} \tag{C.5}$$

where λ_{o_i} are defined in (Eq. 6.15) and λ_o is the total volume fraction of the overdense subregions. Similarly,

$$\lambda_u \rho_u = \sum_i \lambda_{u_i} \rho_{u_i} \implies \rho_u = \frac{\sum_i \lambda_{u_i} \rho_{u_i}}{\sum_i \lambda_{u_i}} \tag{C.6}$$

where λ_{u_i} are defined in (Eq. 6.18) and λ_u is the total volume fraction of the underdense subregions.

Also, $\langle \rho \rangle_{\mathcal{D}}$, the averaged density of the global domain is given by

$$\begin{aligned} \langle \rho \rangle_{\mathcal{D}} &= \lambda_o \rho_o + \lambda_u \rho_u \\ &= \sum_i \lambda_{o_i} \rho_{o_i} + \sum_i \lambda_{u_i} \rho_{u_i} \end{aligned} \tag{C.7}$$

The various density parameters are obtained in our analysis in the following way. From (Eq. 2.14), we have

$$3H_{\mathcal{D}}^2 = 8\pi G \langle \rho \rangle_{\mathcal{D}} - \frac{1}{2} \langle \mathcal{R} \rangle_{\mathcal{D}} - \frac{1}{2} \mathcal{Q}_{\mathcal{D}} \tag{C.8}$$

Dividing by $3H_{\mathcal{D}}^2$ throughout, we get,

$$1 = \Omega_m^{\mathcal{D}} + \Omega_{\mathcal{R}}^{\mathcal{D}} + \Omega_{\mathcal{Q}}^{\mathcal{D}} \tag{C.9}$$

where,

$$\Omega_m^{\mathcal{D}} = \frac{8\pi G \langle \rho \rangle_{\mathcal{D}}}{3H_{\mathcal{D}}^2}; \quad \Omega_{\mathcal{R}}^{\mathcal{D}} = -\frac{\langle \mathcal{R} \rangle_{\mathcal{D}}}{6H_{\mathcal{D}}^2}; \quad \Omega_{\mathcal{Q}}^{\mathcal{D}} = -\frac{\mathcal{Q}_{\mathcal{D}}}{6H_{\mathcal{D}}^2} \tag{C.10}$$

From (Eq. 6.19), we can calculate $\mathcal{Q}_{\mathcal{D}}$ for our model and then from (Eq. C.10), $\Omega_{\mathcal{Q}}^{\mathcal{D}}$ can be calculated. Then using (Eq. C.7) and (Eq. C.10), $\Omega_m^{\mathcal{D}}$ can be calculated and $\Omega_{\mathcal{R}}^{\mathcal{D}}$ can be calculated from (Eq. C.9). In this way, all the average density parameters can be obtained.

Bibliography

[1] Wendy L. Freedman. "Cosmology at a crossroads." In: *Nature Astronomy* 1.5 (2017), p. 0121. ISSN: 2397-3366. DOI: 10.1038/s41550-017-0121. URL: https://doi.org/10.1038/s41550-017-0121.

[2] du Mas des Bourboux, Hélion et al. "Baryon acoustic oscillations from the complete SDSS-III Lyα-quasar cross-correlation function at z = 2.4." In: *A&A* 608 (2017), A130. DOI: 10.1051/0004-6361/201731731. URL: https://doi.org/10.1051/0004-6361/201731731.

[3] Brian D. Fields. "The Primordial Lithium Problem." In: *Annual Review of Nuclear and Particle Science* 61.Volume 61, 2011 (2011), pp. 47–68. ISSN: 1545-4134. DOI: https://doi.org/10.1146/annurev-nucl-102010-130445. URL: https://www.annualreviews.org/content/journals/10.1146/annurev-nucl-102010-130445.

[4] H Hildebrandt et al. "KiDS-450: cosmological parameter constraints from tomographic weak gravitational lensing." In: *Monthly Notices of the Royal Astronomical Society* 465.2 (Oct. 2016), pp. 1454–1498. ISSN: 0035-8711. DOI: 10.1093/mnras/stw2805. eprint: https://academic.oup.com/mnras/article-pdf/465/2/1454/24243465/stw2805.pdf. URL: https://doi.org/10.1093/mnras/stw2805.

[5] Thomas Buchert, Alan A. Coley, Hagen Kleinert, Boudewijn F. Roukema, and David L. Wiltshire. "Observational challenges for the standard FLRW model." In: *International Journal of Modern Physics D* 25.03 (2016), p. 1630007. DOI: 10.1142/S021827181630007X. eprint: https://doi.org/10.1142/S021827181630007X. URL: https://doi.org/10.1142/S021827181630007X.

[6] Adam G. Riess et al. "Cosmic Distances Calibrated to 1% Precision with Gaia EDR3 Parallaxes and Hubble Space Telescope Photometry of 75 Milky Way Cepheids Confirm Tension with ΛCDM." In: *The Astrophysical Journal Letters* 908.1 (2021), p. L6. DOI: 10.3847/2041-8213/abdbaf. URL: https://dx.doi.org/10.3847/2041-8213/abdbaf.

[7] Wendy L. Freedman. "Measurements of the Hubble Constant: Tensions in Perspective*." In: *The Astrophysical Journal* 919.1 (2021), p. 16. DOI: 10.3847/1538-4357/ac0e95. URL: https://dx.doi.org/10.3847/1538-4357/ac0e95.

[8] F. Sylos Labini, N. L. Vasilyev, L. Pietronero, and Y. V. Baryshev. "Absence of self-averaging and of homogeneity in the large-scale galaxy distribution." In: *Europhysics Letters* 86.4 (2009), p. 49001. DOI: 10.1209/0295-5075/86/49001. URL: https://dx.doi.org/10.1209/0295-5075/86/49001.

[9] Alexander Wiegand, Thomas Buchert, and Matthias Ostermann. "Direct Minkowski Functional analysis of large redshift surveys: a new high-speed code tested on the luminous red galaxy Sloan Digital Sky Survey-DR7 catalogue." In: *Monthly Notices of the Royal Astronomical Society* 443.1 (July 2014), pp. 241–259. ISSN: 0035-8711. DOI: 10.1093/mnras/stu1118. URL: https://doi.org/10.1093/mnras/stu1118.

[10] Alexia M Lopez, Roger G Clowes, and Gerard M Williger. "A Giant Arc on the Sky." In: *Monthly Notices of the Royal Astronomical Society* 516.2 (Aug. 2022), pp. 1557–1572. ISSN: 0035-8711. DOI: 10.1093/mnras/stac2204. URL: https://doi.org/10.1093/mnras/stac2204.

[11] M. F. Shirokov and I. Z. Fisher. "Isotropic Space with Discrete Gravitational-Field Sources. On the Theory of a Nonhomogeneous Isotropic Universe." In: Soviet Ast. 6 (Apr. 1963), p. 699.

[12] M. F. Shirokov and I. Z. Fisher. "Isotropic Space with Discrete Gravitational-Field Sources. On the Theory of a Nonhomogeneous Isotropic Universe." In: *General Relativity and Gravitation* 30.9 (1998), pp. 1411–1427. ISSN: 1572-9532. DOI: 10.1023/A:1018860826417. URL: https://doi.org/10.1023/A:1018860826417.

[13] G. F. R. Ellis. "Relativistic Cosmology: Its Nature, Aims and Problems." In: *General Relativity and Gravitation: Invited Papers and Discussion Reports of the 10th International Conference on General Relativity and Gravitation, Padua, July 3–8, 1983*. Dordrecht: Springer Netherlands, 1984, pp. 215–288. ISBN: 978-94-009-6469-3. DOI: 10.1007/978-94-009-6469-3_14. URL: https://doi.org/10.1007/978-94-009-6469-3_14.

[14] G F R Ellis and W Stoeger. "The 'fitting problem' in cosmology." In: *Classical and Quantum Gravity* 4.6 (1987), p. 1697. DOI: 10.1088/0264-9381/4/6/025. URL: https://dx.doi.org/10.1088/0264-9381/4/6/025.

[15] George F.R. Ellis and Thomas Buchert. "The universe seen at different scales." In: *Physics Letters A* 347.1 (2005). Einstein Special Issue, pp. 38–46. ISSN: 0375-9601. DOI: https://doi.org/10.1016/j.physleta.2005.06.087. URL: https://www.sciencedirect.com/science/article/pii/S0375960105010339.

[16] SYKSY RÄSÄNEN. "COSMOLOGICAL ACCELERATION FROM STRUCTURE FORMATION." In: *International Journal of Modern Physics D* 15.12 (Dec. 2006), pp. 2141–2146. ISSN: 1793-6594. DOI: 10.1142/s0218271806009728. URL: http://dx.doi.org/10.1142/S0218271806009728.

[17] Syksy Räsänen. "Accelerated expansion from structure formation." In: *Journal of Cosmology and Astroparticle Physics* 2006.11 (2006), p. 003. DOI: 10.1088/1475-7516/2006/11/003. URL: https://dx.doi.org/10.1088/1475-7516/2006/11/003.

[18] Albert Einstein and Ernst G. Straus. "The Influence of the Expansion of Space on the Gravitation Fields Surrounding the Individual Stars." In: *Rev. Mod. Phys.* 17 (2-3 1945), pp. 120–124. DOI: 10.1103/RevModPhys.17.120. URL: https://link.aps.org/doi/10.1103/RevModPhys.17.120.

[19] Toshifumi Futamase. "Approximation Scheme for Constructing a Clumpy Universe in General Relativity." In: *Phys. Rev. Lett.* 61 (19 1988), pp. 2175–2178. DOI: 10.1103/PhysRevLett.61.2175. URL: https://link.aps.org/doi/10.1103/PhysRevLett.61.2175.

[20] Toshifumi Futamase and Misao Sasaki. "Light propagation and the distance-redshift relation in a realistic inhomogeneous universe." In: *Phys. Rev. D* 40 (8 1989), pp. 2502–2510. DOI: 10.1103/PhysRevD.40.2502. URL: https://link.aps.org/doi/10.1103/PhysRevD.40.2502.

[21] M Gasperini, G Marozzi, F Nugier, and G Veneziano. "Light-cone averaging in cosmology: formalism and applications." In: *Journal of Cosmology and Astroparticle Physics* 2011.07 (2011), pp. 008–008. DOI: 10.1088/1475-7516/2011/07/008. URL: https://doi.org/10.1088/1475-7516/2011/07/008.

[22] Roustam M. Zalaletdinov. "Averaging out the Einstein equations." In: *General Relativity and Gravitation* 24.10 (1992), pp. 1015–1031. ISSN: 1572-9532. DOI: 10.1007/BF00756944. URL: https://doi.org/10.1007/BF00756944.

[23] Roustam M. Zalaletdinov. "Towards a theory of macroscopic gravity." In: *General Relativity and Gravitation* 25.7 (1993), pp. 673–695. ISSN: 1572-9532. DOI: 10.1007/BF00756937. URL: https://doi.org/10.1007/BF00756937.

[24] Roustam M. Zalaletdinov. "Averaging problem in general relativity, macroscopic gravity and using Einstein's equations in cosmology." In: *Bulletin of the Astronomical Society of India* 25 (Sept. 1997), p. 401. DOI: 10.48550/arXiv.gr-qc/9703016. arXiv: gr-qc/9703016 [gr-qc].

[25] Thomas Buchert. "On Average Properties of Inhomogeneous Fluids in General Relativity: Dust Cosmologies." en. In: *General Relativity and Gravitation* 32.1 (Jan. 2000), pp. 105–125. ISSN: 1572-9532. DOI: 10.1023/A:1001800617177. URL: https://doi.org/10.1023/A:1001800617177 (visited on 04/05/2024).

[26] Thomas Buchert. "On Average Properties of Inhomogeneous Fluids in General Relativity: Perfect Fluid Cosmologies." en. In: *General Relativity and Gravitation* 33.8 (Aug. 2001), pp. 1381–1405. ISSN: 1572-9532. DOI: 10.1023/A:1012061725841. URL: https://doi.org/10.1023/A:1012061725841 (visited on 08/30/2023).

[27] Alexander Wiegand and Thomas Buchert. "Multiscale cosmology and structure-emerging dark energy: A plausibility analysis." In: *Phys. Rev. D* 82 (2 2010), p. 023523. DOI: 10.1103/PhysRevD.82.023523. URL: https://link.aps.org/doi/10.1103/PhysRevD.82.023523.

[28] Dominik J. Schwarz. *Accelerated expansion without dark energy*. 2002. DOI: 10.48550/ARXIV.ASTRO-PH/0209584. URL: https://arxiv.org/abs/astro-ph/0209584.

[29] DAVID L. Wiltshire. "Dark Energy without Dark Energy." In: *Dark Matter in Astroparticle and Particle Physics*. World Scientific, 2008, pp. 565–596. DOI: 10.1142/9789812814357_0053. eprint: https://www.worldscientific.com/doi/pdf/10.1142/9789812814357_0053. URL: https://www.worldscientific.com/doi/abs/10.1142/9789812814357_0053.

[30] Edward W Kolb, Sabino Matarrese, and Antonio Riotto. "On cosmic acceleration without dark energy." In: *New Journal of Physics* 8.12 (2006), p. 322. DOI: 10.1088/1367-2630/8/12/322. URL: https://dx.doi.org/10.1088/1367-2630/8/12/322.

[31] Akihiro Ishibashi and Robert M Wald. "Can the acceleration of our universe be explained by the effects of inhomogeneities?" In: *Classical and Quantum Gravity* 23.1 (2005), p. 235. DOI: 10.1088/0264-9381/23/1/012. URL: https://dx.doi.org/10.1088/0264-9381/23/1/012.

[32] Thomas Buchert. "Dark Energy from structure: a status report." In: *General Relativity and Gravitation* 40.2 (2008), pp. 467–527. ISSN: 1572-9532. DOI: 10.1007/s10714-007-0554-8. URL: https://doi.org/10.1007/s10714-007-0554-8.

[33] Syksy Räsänen. "Light propagation in statistically homogeneous and isotropic dust universes." en. In: *Journal of Cosmology and Astroparticle Physics* 2009.02 (Feb. 2009), p. 011. ISSN: 1475-7516. DOI: 10.1088/1475-7516/2009/02/011. URL: https://dx.doi.org/10.1088/1475-7516/2009/02/011 (visited on 08/30/2023).

[34] Syksy Räsänen. "Light propagation in statistically homogeneous and isotropic universes with general matter content." en. In: *Journal of Cosmology and Astroparticle Physics* 2010.03 (Mar. 2010), p. 018. ISSN: 1475-7516. DOI: 10.1088/1475-7516/2010/03/018. URL: https://dx.doi.org/10.1088/1475-7516/2010/03/018 (visited on 08/30/2023).

[35] S.M. Koksbang. "Another look at redshift drift and the backreaction conjecture." In: *Journal of Cosmology and Astroparticle Physics* 2019.10 (2019), p. 036. DOI: 10.1088/1475-7516/2019/10/036. URL: https://dx.doi.org/10.1088/1475-7516/2019/10/036.

[36] S M Koksbang. "Observations in statistically homogeneous, locally inhomogeneous cosmological toy models without FLRW backgrounds." In: *Monthly Notices of the Royal Astronomical Society: Letters* 498.1 (Sept. 2020), pp. L135–L139. ISSN: 1745-3925. DOI: 10.1093/mnrasl/slaa146. URL: https://doi.org/10.1093/mnrasl/slaa146.

[37] S M Koksbang. "Towards statistically homogeneous and isotropic perfect fluid universes with cosmic backreaction." In: *Classical and Quantum Gravity* 36.18 (2019), p. 185004. DOI: 10.1088/1361-6382/ab376c. URL: https://doi.org/10.1088/1361-6382/ab376c.

[38] S.M. Koksbang. "On the relationship between mean observations, spatial averages and the Dyer-Roeder approximation in Einstein-Straus models." In: *Journal of Cosmology and Astroparticle Physics* 2020.11 (2020), p. 061. DOI: 10.1088/1475-7516/2020/11/061. URL: https://dx.doi.org/10.1088/1475-7516/2020/11/061.

[39] T Buchert et al. "Is there proof that backreaction of inhomogeneities is irrelevant in cosmology?" In: *Classical and Quantum Gravity* 32.21 (2015), p. 215021. DOI: 10.1088/0264-9381/32/21/215021. URL: https://dx.doi.org/10.1088/0264-9381/32/21/215021.

[40] Thomas Buchert, Alan A. Coley, Hagen Kleinert, Boudewijn F. Roukema, and David L. Wiltshire. "Observational challenges for the standard FLRW model." In: *International Journal of Modern Physics D* 25.03 (2016), p. 1630007. DOI: 10.1142/S021827181630007X. URL: https://doi.org/10.1142/S021827181630007X.

[41] Syksy Räsänen. "Dark energy from back-reaction." In: *Journal of Cosmology and Astroparticle Physics* 2004.02 (2004), p. 003. DOI: 10.1088/1475-7516/2004/02/003. URL: https://dx.doi.org/10.1088/1475-7516/2004/02/003.

[42] S. M. Koksbang. "Searching for Signals of Inhomogeneity Using Multiple Probes of the Cosmic Expansion Rate $H(z)$." In: *Phys. Rev. Lett.* 126 (23 2021), p. 231101. DOI: 10.1103/PhysRevLett.126.231101. URL: https://link.aps.org/doi/10.1103/PhysRevLett.126.231101.

[43] Syksy Räsänen. "Evaluating backreaction with the peak model of structure formation." In: *Journal of Cosmology and Astroparticle Physics* 2008.04 (2008), p. 026. DOI: 10.1088/1475-7516/2008/04/026. URL: https://dx.doi.org/10.1088/1475-7516/2008/04/026.

[44] Nilok Bose and A. S. Majumdar. "Future deceleration due to cosmic backreaction in presence of the event horizon." In: *Monthly Notices of the Royal Astronomical Society: Letters* 418.1 (Nov. 2011), pp. L45–L48. ISSN: 1745-3925. DOI: 10.1111/j.1745-3933.2011.01140.x. URL: https://doi.org/10.1111/j.1745-3933.2011.01140.x.

[45] Nilok Bose and A. S. Majumdar. "Effect of cosmic backreaction on the future evolution of an accelerating universe." In: *General Relativity and Gravitation* 45.10 (2013), pp. 1971–1987. ISSN: 1572-9532. DOI: 10.1007/s10714-013-1572-3. URL: https://doi.org/10.1007/s10714-013-1572-3.

[46] Amna Ali and A.S. Majumdar. "Future evolution in a backreaction model and the analogous scalar field cosmology." In: *Journal of Cosmology and Astroparticle Physics* 2017.01 (2017), pp. 054–054. DOI: 10.1088/1475-7516/2017/01/054. URL: https://doi.org/10.1088/1475-7516/2017/01/054.

[47] Shashank Shekhar Pandey, Arnab Sarkar, Amna Ali, and A.S. Majumdar. "Effect of inhomogeneities on the propagation of gravitational waves from binaries of compact objects." In: *Journal of Cosmology and Astroparticle Physics* 2022.06 (2022), p. 021. DOI: 10.1088/1475-7516/2022/06/021. URL: https://dx.doi.org/10.1088/1475-7516/2022/06/021.

[48] Shashank Shekhar Pandey, Arnab Sarkar, Amna Ali, and Archan S. Majumdar. "Viscous attenuation of gravitational waves propagating through an inhomogeneous background." In: *The European Physical Journal C* 83.5 (2023), p. 435. ISSN: 1434-6052. DOI: 10.1140/epjc/s10052-023-11605-9. URL: https://doi.org/10.1140/epjc/s10052-023-11605-9.

[49] S.M. Koksbang and S. Hannestad. "Redshift drift in an inhomogeneous universe: averaging and the backreaction conjecture." In: *Journal of Cosmology and Astroparticle Physics* 2016.01 (2016), pp. 009–009. DOI: 10.1088/1475-7516/2016/01/009. URL: https://doi.org/10.1088/1475-7516/2016/01/009.

[50] S. M. Koksbang. "Quantifying effects of inhomogeneities and curvature on gravitational wave standard siren measurements of $H(z)$." In: *Phys. Rev. D* 106 (6 2022), p. 063514. DOI: 10.1103/PhysRevD.106.063514. URL: https://link.aps.org/doi/10.1103/PhysRevD.106.063514.

[51] S. M. Koksbang. "Cosmic backreaction and the mean redshift drift from symbolic regression." In: *Phys. Rev. D* 107 (10 2023), p. 103522. DOI: 10.1103/PhysRevD.107.103522. URL: https://link.aps.org/doi/10.1103/PhysRevD.107.103522.

[52] S. M. Koksbang. "Machine Learning Cosmic Backreaction and Its Effects on Observations." In: *Phys. Rev. Lett.* 130 (20 2023), p. 201003. DOI: 10.1103/PhysRevLett.130.201003. URL: https://link.aps.org/doi/10.1103/PhysRevLett.130.201003.

[53] Ashadul Halder, Shashank Shekhar Pandey, and A.S. Majumdar. "Future deceleration due to backreaction in a Universe with multiple inhomogeneous domains." In: *Journal of Cosmology and Astroparticle Physics* 2023.08 (2023), p. 064. DOI: 10.1088/1475-7516/2023/08/064. URL: https://dx.doi.org/10.1088/1475-7516/2023/08/064.

[54] S. M. Koksbang. "Cosmic backreaction and the mean redshift drift from symbolic regression." In: *Phys. Rev. D* 107 (10 2023), p. 103522. DOI: 10.1103/PhysRevD.107.103522. URL: https://link.aps.org/doi/10.1103/PhysRevD.107.103522.

[55] Syksy Räsänen. "Constraints on backreaction in dust universes." In: *Classical and Quantum Gravity* 23.6 (2006), p. 1823. DOI: 10.1088/0264-9381/23/6/001. URL: https://dx.doi.org/10.1088/0264-9381/23/6/001.

[56] Syksy Räsänen. "Applicability of the linearly perturbed FRW metric and Newtonian cosmology." In: *Phys. Rev. D* 81 (10 2010), p. 103512. DOI: 10.1103/PhysRevD.81.103512. URL: https://link.aps.org/doi/10.1103/PhysRevD.81.103512.

[57] Thomas Buchert and Syksy Räsänen. "Backreaction in Late-Time Cosmology." In: *Annual Review of Nuclear and Particle Science* 62.1 (2012), pp. 57–79. DOI: 10.1146/annurev.nucl.012809.104435. URL: https://doi.org/10.1146/annurev.nucl.012809.104435.

[58] Samae Bagheri and Dominik J. Schwarz. "Light propagation in the averaged universe." In: *Journal of Cosmology and Astroparticle Physics* 2014.10 (2014), pp. 073–073. DOI: 10.1088/1475-7516/2014/10/073. URL: https://doi.org/10.1088/1475-7516/2014/10/073.

[59] M Gasperini, G Marozzi, and G Veneziano. "Gauge invariant averages for the cosmological backreaction." In: *Journal of Cosmology and Astroparticle Physics* 2009.03 (2009), pp. 011–011. DOI: 10.1088/1475-7516/2009/03/011. URL: https://doi.org/10.1088/1475-7516/2009/03/011.

[60] I. Ben-Dayan, M. Gasperini, G. Marozzi, F. Nugier, and G. Veneziano. "Backreaction on the luminosity-redshift relation from gauge invariant light-cone averaging." In: *Journal of Cosmology and Astroparticle Physics* 2012.04 (2012), p. 036. DOI: 10.1088/1475-7516/2012/04/036. URL: https://dx.doi.org/10.1088/1475-7516/2012/04/036.

[61] Mikołaj Korzyński. "Covariant coarse graining of inhomogeneous dust flow in general relativity." In: *Classical and Quantum Gravity* 27.10 (2010), p. 105015. DOI: 10.1088/0264-9381/27/10/105015. URL: https://dx.doi.org/10.1088/0264-9381/27/10/105015.

[62] Timothy Clifton, Kjell Rosquist, and Reza Tavakol. "An exact quantification of backreaction in relativistic cosmology." In: *Phys. Rev. D* 86 (4 2012), p. 043506. DOI: 10.1103/PhysRevD.86.043506. URL: https://link.aps.org/doi/10.1103/PhysRevD.86.043506.

[63] Harald Skarke. "Inhomogeneity implies accelerated expansion." In: *Phys. Rev. D* 89 (4 2014), p. 043506. DOI: 10.1103/PhysRevD.89.043506. URL: https://link.aps.org/doi/10.1103/PhysRevD.89.043506.

[64] A. A. Coley, N. Pelavas, and R. M. Zalaletdinov. "Cosmological Solutions in Macroscopic Gravity." In: *Phys. Rev. Lett.* 95 (15 2005), p. 151102. DOI: 10.1103/PhysRevLett.95.151102. URL: https://link.aps.org/doi/10.1103/PhysRevLett.95.151102.

[65] Pierre Fleury, Hélène Dupuy, and Jean-Philippe Uzan. "Interpretation of the Hubble diagram in a nonhomogeneous universe." In: *Phys. Rev. D* 87 (12 2013), p. 123526. DOI: 10.1103/PhysRevD.87.123526. URL: https://link.aps.org/doi/10.1103/PhysRevD.87.123526.

[66] Pierre Fleury, Hélène Dupuy, and Jean-Philippe Uzan. "Can All Cosmological Observations Be Accurately Interpreted with a Unique Geometry?" In: *Phys. Rev. Lett.* 111 (9 2013), p. 091302. DOI: 10.1103/PhysRevLett.111.091302. URL: https://link.aps.org/doi/10.1103/PhysRevLett.111.091302.

[67] Pierre Fleury. "Swiss-cheese models and the Dyer-Roeder approximation." In: *Journal of Cosmology and Astroparticle Physics* 2014.06 (2014), pp. 054–054. DOI: 10.1088/1475-7516/2014/06/054. URL: https://doi.org/10.1088/1475-7516/2014/06/054.

[68] Shashank Shekhar Pandey, Ashadul Halder, and A. S. Majumdar. "Analyzing the 21-cm signal brightness temperature in the Universe with inhomogeneities." In: *Physical Review D* 110.4 (Aug. 2024). Publisher: American Physical Society, p. 043531. DOI: 10.1103/PhysRevD.110.043531. URL: https://link.aps.org/doi/10.1103/PhysRevD.110.043531 (visited on 09/24/2024).

[69] T. Buchert and J. Ehlers. "Averaging inhomogeneous Newtonian cosmologies." In: A&A 320 (Apr. 1997), pp. 1–7. DOI: 10.48550/arXiv.astro-ph/9510056. arXiv: astro-ph/9510056 [astro-ph].

[70] Jürgen Ehlers. "Contributions to the relativistic mechanics of continuous media." In: *General Relativity and Gravitation* 25.12 (1993), pp. 1225–1266. ISSN: 1572-9532. DOI: 10.1007/BF00759031. URL: https://doi.org/10.1007/BF00759031.

[71] George F. R. Ellis. "Republication of: Relativistic cosmology." In: *General Relativity and Gravitation* 41.3 (2009), pp. 581–660. ISSN: 1572-9532. DOI: 10.1007/s10714-009-0760-7. URL: https://doi.org/10.1007/s10714-009-0760-7.

[72] Julian Adamek, Chris Clarkson, David Daverio, Ruth Durrer, and Martin Kunz. "Safely smoothing spacetime: backreaction in relativistic cosmological simulations." In: *Classical and Quantum Gravity* 36.1 (2018), p. 014001. DOI: 10.1088/1361-6382/aaeca5. URL: https://dx.doi.org/10.1088/1361-6382/aaeca5.

[73] Julien Larena, Jean-Michel Alimi, Thomas Buchert, Martin Kunz, and Pier-Stefano Corasaniti. "Testing backreaction effects with observations." In: *Phys. Rev. D* 79 (8 2009), p. 083011. DOI: 10.1103/PhysRevD.79.083011. URL: https://link.aps.org/doi/10.1103/PhysRevD.79.083011.

[74] Valerio Marra, Edward W. Kolb, and Sabino Matarrese. "Light-cone averages in a Swiss-cheese universe." In: *Phys. Rev. D* 77 (2 2008), p. 023003. DOI: 10.1103/PhysRevD.77.023003. URL: https://link.aps.org/doi/10.1103/PhysRevD.77.023003.

[75] Julien Larena, Jean-Michel Alimi, Thomas Buchert, Martin Kunz, and Pier-Stefano Corasaniti. "Testing backreaction effects with observations." In: *Phys. Rev. D* 79 (8 2009), p. 083011. DOI: 10.1103/PhysRevD.79.083011. URL: https://link.aps.org/doi/10.1103/PhysRevD.79.083011.

[76] Aseem Paranjape and T. P. Singh. "Explicit cosmological coarse graining via spatial averaging." In: *General Relativity and Gravitation* 40.1 (2008), pp. 139–157. ISSN: 1572-9532. DOI: 10.1007/s10714-007-0523-2. URL: https://doi.org/10.1007/s10714-007-0523-2.

[77] Albert Einstein. "Näherungsweise Integration der Feldgleichungen der Gravitation." In: *Sitzungsberichte der Königlich Preussischen Akademie der Wissenschaften* (Jan. 1916), pp. 688–696.

[78] Albert Einstein. "Über Gravitationswellen." In: *Sitzungsberichte der Königlich Preußischen Akademie der Wissenschaften (Berlin* (Jan. 1918), pp. 154–167.

[79] Michele Maggiore. *Gravitational Waves: Volume 1: Theory and Experiments*. Oxford University Press, Oct. 2007. ISBN: 9780198570745. DOI: 10.1093/acprof:oso/9780198570745.001.0001. URL: https://doi.org/10.1093/acprof:oso/9780198570745.001.0001.

[80] W. Baade. "The Absolute Photographic Magnitude of Supernovae." In: ApJ 88 (Oct. 1938), p. 285. DOI: 10.1086/143983.

[81] C. T. Kowal. "Absolute magnitudes of supernovae." In: AJ 73 (Dec. 1968), pp. 1021–1024. DOI: 10.1086/110763.

[82] J. C. Wheeler and R. Levreault. "The peculiar type I supernova in NGC 991." In: ApJ 294 (July 1985), pp. L17–L20. DOI: 10.1086/184500.

[83] A. Uomoto and R. P. Kirshner. "Peculiar type I supernovae." In: A&A 149 (Aug. 1985), pp. L7–L9.

[84] Douglas L. Miller and David Branch. "Supernova Absolute-Magnitude Distributions." In: AJ 100 (Aug. 1990), p. 530. DOI: 10.1086/115534.

[85] David Branch and G. A. Tammann. "Type IA supernovae as standard candles." In: ARA&A 30 (Jan. 1992), pp. 359–389. DOI: 10.1146/annurev.aa.30.090192.002043.

[86] David Branch and Douglas L. Miller. "Type IA Supernovae as Standard Candles." In: ApJ 405 (Mar. 1993), p. L5. DOI: 10.1086/186752.

[87] G. A. Tammann and B. Leibundgut. "Supernova studies. IV. The global value of HO from supernovae IA and the peculiar motion of field galaxies." In: A&A 236 (Sept. 1990), p. 9.

[88] M. Kowalski et al. "Improved Cosmological Constraints from New, Old, and Combined Supernova Data Sets." In: *The Astrophysical Journal* 686.2 (2008), p. 749. DOI: 10.1086/589937. URL: https://dx.doi.org/10.1086/589937.

[89] R. Amanullah, C. Lidman, D. Rubin, et al. In: *ApJ* 716 (2010), p. 712. DOI: 10.1088/0004-637X/716/1/712. URL: https://doi.org/10.1088/0004-637X/716/1/712.

[90] Dani Gamerman and Hedibert F. Lopes. *Markov Chain Monte Carlo: Stochastic Simulation for Bayesian Inference, Second Edition*. 2nd ed. Chapman and Hall/CRC, 2006. DOI: 10.1201/9781482296426. URL: https://doi.org/10.1201/9781482296426.

[91] Heikki Haario, Marko Laine, Antonietta Mira, and Eero Saksman. "DRAM: Efficient adaptive MCMC." In: *Statistics and Computing* 16.4 (2006), pp. 339–354. ISSN: 1573-1375. DOI: 10.1007/s11222-006-9438-0. URL: https://doi.org/10.1007/s11222-006-9438-0.

[92] Heikki Haario, Eero Saksman, and Johanna Tamminen. "An Adaptive Metropolis Algorithm." In: *Bernoulli* 7.2 (2001), pp. 223–242. ISSN: 13507265. DOI: 10.2307/3318737. URL: http://www.jstor.org/stable/3318737 (visited on 06/06/2023).

[93] B. P. Abbott *et al.* "Observation of Gravitational Waves from a Binary Black Hole Merger." In: *Phys. Rev. Lett.* 116 (6 2016), p. 061102. DOI: 10.1103/PhysRevLett.116.061102. URL: https://link.aps.org/doi/10.1103/PhysRevLett.116.061102.

[94] B. P. Abbott *et al.* "GW170104: Observation of a 50-Solar-Mass Binary Black Hole Coalescence at Redshift 0.2." In: *Phys. Rev. Lett.* 118 (22 2017), p. 221101. DOI: 10.1103/PhysRevLett.118.221101. URL: https://link.aps.org/doi/10.1103/PhysRevLett.118.221101.

[95] B. P. Abbott *et al.* "GW170814: A Three-Detector Observation of Gravitational Waves from a Binary Black Hole Coalescence." In: *Phys. Rev. Lett.* 119 (14 2017), p. 141101. DOI: 10.1103/PhysRevLett.119.141101. URL: https://link.aps.org/doi/10.1103/PhysRevLett.119.141101.

[96] B. P. Abbott *et al.* "GW170817: Observation of Gravitational Waves from a Binary Neutron Star Inspiral." In: *Phys. Rev. Lett.* 119 (16 2017), p. 161101. DOI: 10.1103/PhysRevLett.119.161101. URL: https://link.aps.org/doi/10.1103/PhysRevLett.119.161101.

[97] B. P. Abbott *et al.* "GW170608: Observation of a 19 Solar-mass Binary Black Hole Coalescence." In: *The Astrophysical Journal* 851.2 (2017), p. L35. DOI: 10.3847/2041-8213/aa9f0c. URL: https://doi.org/10.3847/2041-8213/aa9f0c.

[98] S.M. Koksbang and S. Hannestad. "Redshift drift in an inhomogeneous universe: averaging and the backreaction conjecture." In: *Journal of Cosmology and Astroparticle Physics* 2016.01 (2016), pp. 009–009. DOI: 10.1088/1475-7516/2016/01/009. URL: https://doi.org/10.1088/1475-7516/2016/01/009.

[99] Alexander H. Nitz et al. "1-OGC: The First Open Gravitational-wave Catalog of Binary Mergers from Analysis of Public Advanced LIGO Data." In: *The Astrophysical Journal* 872.2 (2019), p. 195. DOI: 10.3847/1538-4357/ab0108. URL: https://dx.doi.org/10.3847/1538-4357/ab0108.

[100] B. P. Abbott et al. "GWTC-1: A Gravitational-Wave Transient Catalog of Compact Binary Mergers Observed by LIGO and Virgo during the First and Second Observing Runs." In: *Phys. Rev. X* 9 (3 2019), p. 031040. DOI: 10.1103/PhysRevX.9.031040. URL: https://link.aps.org/doi/10.1103/PhysRevX.9.031040.

[101] A. N. Baushev. "The central region of a void: an analytical solution." In: *Monthly Notices of the Royal Astronomical Society: Letters* 504.1 (Apr. 2021), pp. L56–L60. ISSN: 1745-3925. DOI: 10.1093/mnrasl/slab036. eprint: https://academic.oup.com/mnrasl/article-pdf/504/1/L56/37929693/slab036.pdf. URL: https://doi.org/10.1093/mnrasl/slab036.

[102] Asta Heinesen. "Multipole decomposition of redshift drift: Model-independent mapping of the expansion history of the Universe." In: *Phys. Rev. D* 103 (2 2021), p. 023537. DOI: 10.1103/PhysRevD.103.023537. URL: https://link.aps.org/doi/10.1103/PhysRevD.103.023537.

[103] Pablo A. Rosado et al. "Detectability of Gravitational Waves from High-Redshift Binaries." In: *Phys. Rev. Lett.* 116 (10 2016), p. 101102. DOI: 10.1103/PhysRevLett.116.101102. URL: https://link.aps.org/doi/10.1103/PhysRevLett.116.101102.

[104] Juan García-Bellido. "Massive Primordial Black Holes as Dark Matter and their detection with Gravitational Waves." In: *Journal of Physics: Conference Series* 840.1 (2017), p. 012032. DOI: 10.1088/1742-6596/840/1/012032. URL: https://dx.doi.org/10.1088/1742-6596/840/1/012032.

[105] Arnab Sarkar, K. Rajesh Nayak, and A. S. Majumdar. "Stochastic gravitational wave background from accreting primordial black hole binaries during early inspiral stage." In: *Phys. Rev. D* 100 (10 2019), p. 103514. DOI: 10.1103/PhysRevD.100.103514. URL: https://link.aps.org/doi/10.1103/PhysRevD.100.103514.

[106] Huai-Ke Guo, Kuver Sinha, Daniel Vagie, and Graham White. "Phase transitions in an expanding universe: stochastic gravitational waves in standard and non-standard histories." In: *Journal of Cosmology and Astroparticle Physics* 2021.01 (2021), pp. 001–001. DOI: 10.1088/1475-7516/2021/01/001. URL: https://doi.org/10.1088/1475-7516/2021/01/001.

[107] B. P. Abbott *et al.* "GW151226: Observation of Gravitational Waves from a 22-Solar-Mass Binary Black Hole Coalescence." In: *Phys. Rev. Lett.* 116 (24 2016), p. 241103. DOI: 10.1103/PhysRevLett.116.241103. URL: https://link.aps.org/doi/10.1103/PhysRevLett.116.241103.

[108] A.R. Prasanna. "Propagation of gravitational waves through a dispersive medium." In: *Physics Letters A* 257.3 (1999), pp. 120–122. ISSN: 0375-9601. DOI: https://doi.org/10.1016/S0375-9601(99)00313-8. URL: https://www.sciencedirect.com/science/article/pii/S0375960199003138.

[109] S. W. Hawking. "Perturbations of an Expanding Universe." In: *The Astrophysical Journal* 145 (Aug. 1966), p. 544. DOI: 10.1086/148793.

[110] F. Paul Esposito. "Absorption of Gravitational Energy by a Viscous Compressible Fluid." In: *The Astrophysical Journal* 165 (Apr. 1971), p. 165. DOI: 10.1086/150884.

[111] J. Madore. "The absorption of gravitational radiation by a dissipative fluid." In: *Communications in Mathematical Physics* 30.4 (1973), pp. 335–340. ISSN: 1432-0916. DOI: 10.1007/BF01645508. URL: https://doi.org/10.1007/BF01645508.

[112] A. M. Anile and V. Pirronello. "High-frequency gravitational waves in a dissipative fluid." In: *Il Nuovo Cimento B (1971-1996)* 48.1 (1978), pp. 90–101. ISSN: 1826-9877. DOI: 10.1007/BF02748651. URL: https://doi.org/10.1007/BF02748651.

[113] Gaurav Goswami, Girish Kumar Chakravarty, Subhendra Mohanty, and A. R. Prasanna. "Constraints on cosmological viscosity and self-interacting dark matter from gravitational wave observations." In: *Phys. Rev. D* 95 (10 2017), p. 103509. DOI: 10.1103/PhysRevD.95.103509. URL: https://link.aps.org/doi/10.1103/PhysRevD.95.103509.

[114] Iver Brevik and Shin'ichi Nojiri. "Gravitational waves in the presence of viscosity." In: *International Journal of Modern Physics D* 28.10 (2019), p. 1950133. DOI: 10.1142/S0218271819501335. eprint: https://doi.org/10.1142/S0218271819501335. URL: https://doi.org/10.1142/S0218271819501335.

[115] Nahuel Mirón-Granese. "Relativistic viscous effects on the primordial gravitational waves spectrum." In: *Journal of Cosmology and Astroparticle Physics* 2021.06 (2021), p. 008. DOI: 10.1088/1475-7516/2021/06/008. URL: https://dx.doi.org/10.1088/1475-7516/2021/06/008.

[116] Fabio Moretti, Flavio Bombacigno, and Giovanni Montani. "Gravitational Landau damping for massive scalar modes." In: *The European Physical Journal C* 80.12 (2020), p. 1203. ISSN: 1434-6052. DOI: 10.1140/epjc/s10052-020-08769-z. URL: https://doi.org/10.1140/epjc/s10052-020-08769-z.

[117] Fabio Moretti, Flavio Bombacigno, and Giovanni Montani. "The Role of Longitudinal Polarizations in Horndeski and Macroscopic Gravity: Introducing Gravitational Plasmas." In: *Universe* 7.12 (2021). ISSN: 2218-1997. DOI: 10.3390/universe7120496. URL: https://www.mdpi.com/2218-1997/7/12/496.

[118] T. Padmanabhan and S.M. Chitre. "Viscous universes." In: *Physics Letters A* 120.9 (1987), pp. 433–436. ISSN: 0375-9601. DOI: https://doi.org/10.1016/0375-9601(87)90104-6. URL: https://www.sciencedirect.com/science/article/pii/0375960187901046.

[119] George L. Murphy. "Big-Bang Model Without Singularities." In: *Phys. Rev. D* 8 (12 1973), pp. 4231–4233. DOI: 10.1103/PhysRevD.8.4231. URL: https://link.aps.org/doi/10.1103/PhysRevD.8.4231.

[120] J. C. Fabris, S. V. B. Gonçalves, and R. de Sá Ribeiro. "Bulk viscosity driving the acceleration of the Universe." In: *General Relativity and Gravitation* 38.3 (2006), pp. 495–506. ISSN: 1572-9532. DOI: 10.1007/s10714-006-0236-y. URL: https://doi.org/10.1007/s10714-006-0236-y.

[121] Jean-Sebastien Gagnon and Julien Lesgourgues. "Dark goo: bulk viscosity as an alternative to dark energy." In: *Journal of Cosmology and Astroparticle Physics* 2011.09 (2011), pp. 026–026. DOI: 10.1088/1475-7516/2011/09/026. URL: https://doi.org/10.1088/1475-7516/2011/09/026.

[122] Stefan Floerchinger, Nikolaos Tetradis, and Urs Achim Wiedemann. "Accelerating Cosmological Expansion from Shear and Bulk Viscosity." In: *Phys. Rev. Lett.* 114 (9 2015), p. 091301. DOI: 10.1103/PhysRevLett.114.091301. URL: https://link.aps.org/doi/10.1103/PhysRevLett.114.091301.

[123] Abhishek Atreya, Jitesh R. Bhatt, and Arvind Mishra. "Viscous self interacting dark matter and cosmic acceleration." In: *Journal of Cosmology and Astroparticle Physics* 2018.02 (2018), pp. 024–024. DOI: 10.1088/1475-7516/2018/02/024. URL: https://doi.org/10.1088/1475-7516/2018/02/024.

[124] N. D. Jerin Mohan, Athira Sasidharan, and Titus K. Mathew. "Bulk viscous matter and recent acceleration of the universe based on causal viscous theory." In: *The European Physical Journal C* 77.12 (2017), p. 849. ISSN: 1434-6052. DOI: 10.1140/epjc/s10052-017-5428-y. URL: https://doi.org/10.1140/epjc/s10052-017-5428-y.

[125] Sudipta Das and Narayan Banerjee. "Can Neutrino Viscosity Drive the Late Time Cosmic Acceleration?" In: *International Journal of Theoretical Physics* 51.9 (2012), pp. 2771–2778. ISSN: 1572-9575. DOI: 10.1007/s10773-012-1152-4. URL: https://doi.org/10.1007/s10773-012-1152-4.

[126] Iver Brevik, Øyvind Grøn, Jaume de Haro, Sergei D. Odintsov, and Emmanuel N. Saridakis. "Viscous cosmology for early- and late-time universe." In: *International Journal of Modern Physics D* 26.14 (2017), p. 1730024. DOI: 10.1142/S0218271817300245. eprint: https://doi.org/10.1142/S0218271817300245. URL: https://doi.org/10.1142/S0218271817300245.

[127] Sampurn Anand, Prakrut Chaubal, Arindam Mazumdar, Subhendra Mohanty, and Priyank Parashari. "Bounds on neutrino mass in viscous cosmology." In: *Journal of Cosmology and Astroparticle Physics* 2018.05 (2018), pp. 031–031. DOI: 10.1088/1475-7516/2018/05/031. URL: https://doi.org/10.1088/1475-7516/2018/05/031.

[128] Ashadul Halder, Shashank Shekhar Pandey, and A.S. Majumdar. "Global 21-cm brightness temperature in viscous dark energy models." In: *Journal of Cosmology and Astroparticle Physics* 2022.10 (2022), p. 049. DOI: 10.1088/1475-7516/2022/10/049. URL: https://dx.doi.org/10.1088/1475-7516/2022/10/049.

[129] Pravin Kumar Natwariya, Jitesh R. Bhatt, and Arun Kumar Pandey. "Viscosity in cosmic fluids." In: *The European Physical Journal C* 80.8 (2020), p. 767. ISSN: 1434-6052. DOI: 10.1140/epjc/s10052-020-8341-8. URL: https://doi.org/10.1140/epjc/s10052-020-8341-8.

[130] David N. Spergel and Paul J. Steinhardt. "Observational Evidence for Self-Interacting Cold Dark Matter." In: *Phys. Rev. Lett.* 84 (17 2000), pp. 3760–3763. DOI: 10.1103/PhysRevLett.84.3760. URL: https://link.aps.org/doi/10.1103/PhysRevLett.84.3760.

[131] Sean Tulin and Hai-Bo Yu. "Dark matter self-interactions and small scale structure." In: *Physics Reports* 730 (2018), pp. 1–57. ISSN: 0370-1573. DOI: https://doi.org/10.1016/j.physrep.2017.11.004. URL: https://www.sciencedirect.com/science/article/pii/S0370157317304039.

[132] Manoj Kaplinghat, Sean Tulin, and Hai-Bo Yu. "Dark Matter Halos as Particle Colliders: Unified Solution to Small-Scale Structure Puzzles from Dwarfs to Clusters." In: *Phys. Rev. Lett.* 116 (4 2016), p. 041302. DOI: 10.1103/PhysRevLett.116.041302. URL: https://link.aps.org/doi/10.1103/PhysRevLett.116.041302.

[133] Sampurn Anand, Prakrut Chaubal, Arindam Mazumdar, and Subhendra Mohanty. "Cosmic viscosity as a remedy for tension between PLANCK and LSS data." In: *Journal of Cosmology and Astroparticle Physics* 2017.11 (2017), pp. 005–005. DOI: 10.1088/1475-7516/2017/11/005. URL: https://doi.org/10.1088/1475-7516/2017/11/005.

[134] Asta Heinesen and Thomas Buchert. "Solving the curvature and Hubble parameter inconsistencies through structure formation-induced curvature." In: *Classical and Quantum Gravity* 37.16 (2020), p. 164001. DOI: 10.1088/1361-6382/ab954b. URL: https://dx.doi.org/10.1088/1361-6382/ab954b.

[135] Syksy Räsänen. "Light propagation in statistically homogeneous and isotropic dust universes." In: *Journal of Cosmology and Astroparticle Physics* 2009.02 (2009), pp. 011–011. DOI: 10.1088/1475-7516/2009/02/011. URL: https://doi.org/10.1088/1475-7516/2009/02/011.

[136] Steven Weinberg. *Gravitation and Cosmology: Principles and Applications of the General Theory of Relativity*. 1972.

[137] Oscar M. Pimentel, F. D. Lora-Clavijo, and Guillermo A. González. "The energy-momentum tensor for a dissipative fluid in general relativity." In: *General Relativity and Gravitation* 48.10 (2016), p. 124. ISSN: 1572-9532. DOI: 10.1007/s10714-016-2121-7. URL: https://doi.org/10.1007/s10714-016-2121-7.

[138] C. M. S. Barbosa, H. Velten, J. C. Fabris, and Rudnei O. Ramos. "Assessing the impact of bulk and shear viscosities on large scale structure formation." In: *Phys. Rev. D* 96 (2 2017), p. 023527. DOI: 10.1103/PhysRevD.96.023527. URL: https://link.aps.org/doi/10.1103/PhysRevD.96.023527.

[139] Hermano Velten, Thiago R. P. Caramês, Júlio C. Fabris, Luciano Casarini, and Ronaldo C. Batista. "Structure formation in a Λ viscous CDM universe." In: *Phys. Rev. D* 90 (12 2014), p. 123526. DOI: 10.1103/PhysRevD.90.123526. URL: https://link.aps.org/doi/10.1103/PhysRevD.90.123526.

[140] Ben David Normann and Iver Brevik. "Characteristic properties of two different viscous cosmology models for the future universe." In: *Modern Physics Letters A* 32.04 (2017), p. 1750026. DOI: 10.1142/S0217732317500262. eprint: https://doi.org/10.1142/S0217732317500262. URL: https://doi.org/10.1142/S0217732317500262.

[141] Ben David Normann and Iver Brevik. "General Bulk-Viscous Solutions and Estimates of Bulk Viscosity in the Cosmic Fluid." In: *Entropy* 18.6 (2016). ISSN: 1099-4300. DOI: 10.3390/e18060215. URL: https://www.mdpi.com/1099-4300/18/6/215.

[142] JIAXIN WANG and XINHE MENG. "EFFECTS OF NEW VISCOSITY MODEL ON COSMOLOGICAL EVOLUTION." In: *Modern Physics Letters A* 29.03 (2014), p. 1450009. DOI: 10.1142/S0217732314500096. eprint: https://doi.org/10.1142/S0217732314500096. URL: https://doi.org/10.1142/S0217732314500096.

[143] Athira Sasidharan and Titus K. Mathew. "Phase space analysis of bulk viscous matter dominated universe." In: *Journal of High Energy Physics* 2016.6 (2016), p. 138. ISSN: 1029-8479. DOI: 10.1007/JHEP06(2016)138. URL: https://doi.org/10.1007/JHEP06(2016)138.

[144] Hermano Velten and Dominik J. Schwarz. "Dissipation of dark matter." In: *Phys. Rev. D* 86 (8 2012), p. 083501. DOI: 10.1103/PhysRevD.86.083501. URL: https://link.aps.org/doi/10.1103/PhysRevD.86.083501.

[145] Lars Husdal. "Viscosity in a lepton-photon universe." In: *Astrophysics and Space Science* 361.8 (2016), p. 263. ISSN: 1572-946X. DOI: 10.1007/s10509-016-2847-4. URL: https://doi.org/10.1007/s10509-016-2847-4.

[146] Pablo A. Rosado et al. "Detectability of Gravitational Waves from High-Redshift Binaries." In: *Phys. Rev. Lett.* 116 (10 2016), p. 101102. DOI: 10.1103/PhysRevLett.116.101102. URL: https://link.aps.org/doi/10.1103/PhysRevLett.116.101102.

[147] S. Perlmutter et al. "Discovery of a supernova explosion at half the age of the Universe." In: *Nature* 391.6662 (1998), pp. 51–54. ISSN: 1476-4687. DOI: 10.1038/34124. URL: https://doi.org/10.1038/34124.

[148] Adam G. Riess et al. "Observational Evidence from Supernovae for an Accelerating Universe and a Cosmological Constant." In: *The Astronomical Journal* 116.3 (1998), p. 1009. DOI: 10.1086/300499. URL: https://dx.doi.org/10.1086/300499.

[149] Malcolm Hicken et al. "IMPROVED DARK ENERGY CONSTRAINTS FROM ~100 NEW CfA SUPERNOVA TYPE Ia LIGHT CURVES." In: *The Astrophysical Journal* 700.2 (2009), p. 1097. DOI: 10.1088/0004-637X/700/2/1097. URL: https://dx.doi.org/10.1088/0004-637X/700/2/1097.

[150] Marina Seikel and Dominik J. Schwarz. "Model- and calibration-independent test of cosmic acceleration." In: *Journal of Cosmology and Astroparticle Physics* 2009.02 (2009), p. 024. DOI: 10.1088/1475-7516/2009/02/024. URL: https://dx.doi.org/10.1088/1475-7516/2009/02/024.

[151] R.R Caldwell. "A phantom menace? Cosmological consequences of a dark energy component with super-negative equation of state." In: *Physics Letters B* 545.1 (2002), pp. 23–29. ISSN: 0370-2693. DOI: https://doi.org/10.1016/S0370-2693(02)02589-3. URL: https://www.sciencedirect.com/science/article/pii/S0370269302025893.

[152] Robert R. Caldwell, Marc Kamionkowski, and Nevin N. Weinberg. "Phantom Energy: Dark Energy with $\omega < -1$ Causes a Cosmic Doomsday." In: *Phys. Rev. Lett.* 91 (7 2003), p. 071301. DOI: 10.1103/PhysRevLett.91.071301. URL: https://link.aps.org/doi/10.1103/PhysRevLett.91.071301.

[153] Marcelo M. Disconzi, Thomas W. Kephart, and Robert J. Scherrer. "New approach to cosmological bulk viscosity." In: *Phys. Rev. D* 91 (4 2015), p. 043532. DOI: 10.1103/PhysRevD.91.043532. URL: https://link.aps.org/doi/10.1103/PhysRevD.91.043532.

[154] Syksy Räsänen. "Constraints on backreaction in dust universes." In: *Classical and Quantum Gravity* 23.6 (2006), p. 1823. DOI: 10.1088/0264-9381/23/6/001. URL: https://dx.doi.org/10.1088/0264-9381/23/6/001.

[155] N. Suzuki et al. "THE HUBBLE SPACE TELESCOPE CLUSTER SUPERNOVA SURVEY. V. IMPROVING THE DARK-ENERGY CONSTRAINTS ABOVE z > 1 AND BUILDING AN EARLY-TYPE-HOSTED SUPERNOVA SAMPLE⋆." In: *The Astrophysical Journal* 746.1 (2012), p. 85. DOI: 10.1088/0004-637X/746/1/85. URL: https://dx.doi.org/10.1088/0004-637X/746/1/85.

[156] David L Wiltshire. "Cosmic clocks, cosmic variance and cosmic averages." In: *New Journal of Physics* 9.10 (2007), p. 377. DOI: 10.1088/1367-2630/9/10/377. URL: https://dx.doi.org/10.1088/1367-2630/9/10/377.

[157] Planck Collaboration et al. "Planck 2018 results - VI. Cosmological parameters." In: *A&A* 641 (2020), A6. DOI: 10.1051/0004-6361/201833910. URL: https://doi.org/10.1051/0004-6361/201833910.

[158] Steven R. Furlanetto, S. Peng Oh, and Frank H. Briggs. "Cosmology at low frequencies: The 21cm transition and the high-redshift Universe." In: *Physics Reports* 433.4 (2006), pp. 181–301. ISSN: 0370-1573. DOI: https://doi.org/10.1016/j.physrep.2006.08.002. URL: https://www.sciencedirect.com/science/article/pii/S0370157306002730.

[159] Miguel F. Morales and J. Stuart B. Wyithe. "Reionization and Cosmology with 21-cm Fluctuations." In: *Annual Review of Astronomy and Astrophysics* 48.1 (2010), pp. 127–171. DOI: 10.1146/annurev-astro-081309-130936.

[160] Jonathan R Pritchard and Abraham Loeb. "21 cm cosmology in the 21st century." In: *Reports on Progress in Physics* 75.8 (2012), p. 086901. DOI: 10.1088/0034-4885/75/8/086901. URL: https://dx.doi.org/10.1088/0034-4885/75/8/086901.

[161] H. I. Ewen and E. M. Purcell. "Observation of a Line in the Galactic Radio Spectrum: Radiation from Galactic Hydrogen at 1,420 Mc./sec." In: *Nature* 168.4270 (1951), pp. 356–356. ISSN: 1476-4687. DOI: 10.1038/168356a0. URL: https://doi.org/10.1038/168356a0.

[162] C. A. Muller and J. H. Oort. "Observation of a Line in the Galactic Radio Spectrum: The Interstellar Hydrogen Line at 1,420 Mc./sec., and an Estimate of Galactic Rotation." In: *Nature* 168.4270 (1951), pp. 357–358. ISSN: 1476-4687. DOI: 10.1038/168357a0. URL: https://doi.org/10.1038/168357a0.

[163] Judd D. Bowman, Alan E. E. Rogers, Raul A. Monsalve, Thomas J. Mozdzen, and Nivedita Mahesh. "An absorption profile centred at 78 megahertz in the sky-averaged spectrum." In: *Nature* 555.7694 (2018), pp. 67–70. ISSN: 1476-4687. DOI: 10.1038/nature25792. URL: https://doi.org/10.1038/nature25792.

[164] Saurabh Singh et al. "SARAS 2 Constraints on Global 21 cm Signals from the Epoch of Reionization*." In: *The Astrophysical Journal* 858.1 (2018), p. 54. DOI: 10.3847/1538-4357/aabae1. URL: https://dx.doi.org/10.3847/1538-4357/aabae1.

[165] Saurabh Singh et al. "On the detection of a cosmic dawn signal in the radio background." In: *Nature Astronomy* 6.5 (2022), pp. 607–617. ISSN: 2397-3366. DOI: 10.1038/s41550-022-01610-5. URL: https://doi.org/10.1038/s41550-022-01610-5.

[166] Ashadul Halder and Madhurima Pandey. "Probing the effects of primordial black holes on 21-cm EDGES signal along with interacting dark energy and dark matter–baryon scattering." In: *Monthly Notices of the Royal Astronomical Society* 508.3 (Oct. 2021), pp. 3446–3454. ISSN: 0035-8711. DOI: 10.1093/mnras/stab2795. URL: https://doi.org/10.1093/mnras/stab2795.

[167] Ashadul Halder and Shibaji Banerjee. "Bounds on abundance of primordial black hole and dark matter from EDGES 21-cm signal." In: *Phys. Rev. D* 103 (6 2021), p. 063044. DOI: 10.1103/PhysRevD.103.063044. URL: https://link.aps.org/doi/10.1103/PhysRevD.103.063044.

[168] Ashadul Halder, Madhurima Pandey, Debasish Majumdar, and Rupa Basu. "Exploring multimessenger signals from heavy dark matter decay with EDGES 21-cm result and IceCube." In: *Journal of Cosmology and Astroparticle Physics* 2021.10 (2021), p. 033. DOI: 10.1088/1475-7516/2021/10/033. URL: https://dx.doi.org/10.1088/1475-7516/2021/10/033.

[169] Steven J. Clark, Bhaskar Dutta, Yu Gao, Yin-Zhe Ma, and Louis E. Strigari. "21 cm limits on decaying dark matter and primordial black holes." In: *Phys. Rev. D* 98 (4 2018), p. 043006. DOI: 10.1103/PhysRevD.98.043006. URL: https://link.aps.org/doi/10.1103/PhysRevD.98.043006.

[170] Upala Mukhopadhyay, Debasish Majumdar, and Kanan K. Datta. "Probing interacting dark energy and scattering of baryons with dark matter in light of the EDGES 21-cm signal." In: *Phys. Rev. D* 103 (6 2021), p. 063510. DOI: 10.1103/PhysRevD.103.063510. URL: https://link.aps.org/doi/10.1103/PhysRevD.103.063510.

[171] Yupeng Yang. "Constraints on primordial black holes and curvature perturbations from the global 21-cm signal." In: *Phys. Rev. D* 102 (8 2020), p. 083538. DOI: 10.1103/PhysRevD.102.083538. URL: https://link.aps.org/doi/10.1103/PhysRevD.102.083538.

[172] Julian B. Muñoz, Ely D. Kovetz, and Yacine Ali-Haïmoud. "Heating of baryons due to scattering with dark matter during the dark ages." In: *Phys. Rev. D* 92 (8 2015), p. 083528. DOI: 10.1103/PhysRevD.92.083528. URL: https://link.aps.org/doi/10.1103/PhysRevD.92.083528.

[173] Akash Kumar Saha and Ranjan Laha. "Sensitivities on nonspinning and spinning primordial black hole dark matter with global 21-cm troughs." In: *Phys. Rev. D* 105 (10 2022), p. 103026. DOI: 10.1103/PhysRevD.105.103026. URL: https://link.aps.org/doi/10.1103/PhysRevD.105.103026.

[174] M. Chianese, P. Di Bari, K. Farrag, and R. Samanta. "Probing relic neutrino radiative decays with 21cm cosmology." In: *Physics Letters B* 790 (2019), pp. 64–70. ISSN: 0370-2693. DOI: https://doi.org/10.1016/j.physletb.2018.09.040. URL: https://www.sciencedirect.com/science/article/pii/S037026931830741X.

[175] Julian B. Muñoz, Ely D. Kovetz, and Yacine Ali-Haïmoud. "Heating of baryons due to scattering with dark matter during the dark ages." In: *Phys. Rev. D* 92 (8 2015), p. 083528. DOI: 10.1103/PhysRevD.92.083528. URL: https://link.aps.org/doi/10.1103/PhysRevD.92.083528.

[176] Yacine Ali-Haïmoud and Christopher M. Hirata. "Ultrafast effective multilevel atom method for primordial hydrogen recombination." In: *Phys. Rev. D* 82 (6 2010), p. 063521. DOI: 10.1103/PhysRevD.82.063521. URL: https://link.aps.org/doi/10.1103/PhysRevD.82.063521.

[177] Matias Zaldarriaga, Steven R. Furlanetto, and Lars Hernquist. "21 Centimeter Fluctuations from Cosmic Gas at High Redshifts." In: *The Astrophysical Journal* 608.2 (2004), p. 622. DOI: 10.1086/386327. URL: https://dx.doi.org/10.1086/386327.

[178] S. A. Wouthuysen. "On the excitation mechanism of the 21-cm (radio-frequency) interstellar hydrogen emission line." In: *The Astronomical Journal* 57 (Jan. 1952), pp. 31–32. DOI: 10.1086/106661.

[179] George B. Field. "Excitation of the Hydrogen 21-CM Line." In: *Proceedings of the IRE* 46.1 (1958), pp. 240–250. DOI: 10.1109/JRPROC.1958.286741.

[180] Michael Kuhlen, Piero Madau, and Ryan Montgomery. "The Spin Temperature and 21 cm Brightness of the Intergalactic Medium in the Pre-Reionization era." In: *The Astrophysical Journal* 637.1 (2006), p. L1. DOI: 10.1086/500548. URL: https://dx.doi.org/10.1086/500548.

[181] Christopher M. Hirata. "Wouthuysen-Field coupling strength and application to high-redshift 21-cm radiation." In: *Monthly Notices of the Royal Astronomical Society* 367.1 (Mar. 2006), pp. 259–274. ISSN: 0035-8711. DOI: 10.1111/j.1365-2966.2005.09949.x. URL: https://doi.org/10.1111/j.1365-2966.2005.09949.x.

[182] Benedetta Ciardi and Piero Madau. "Probing beyond the Epoch of Hydrogen Reionization with 21 Centimeter Radiation." In: *The Astrophysical Journal* 596.1 (2003), p. 1. DOI: 10.1086/377634. URL: https://dx.doi.org/10.1086/377634.

[183] Yacine Ali-Haïmoud and Christopher M. Hirata. "HyRec: A fast and highly accurate primordial hydrogen and helium recombination code." In: *Phys. Rev. D* 83 (4 2011), p. 043513. DOI: 10.1103/PhysRevD.83.043513. URL: https://link.aps.org/doi/10.1103/PhysRevD.83.043513.

[184] Mathew S. Madhavacheril, Neelima Sehgal, and Tracy R. Slatyer. "Current dark matter annihilation constraints from CMB and low-redshift data." In: *Phys. Rev. D* 89 (10 2014), p. 103508. DOI: 10.1103/PhysRevD.89.103508. URL: https://link.aps.org/doi/10.1103/PhysRevD.89.103508.

[185] P. J. E. Peebles. "Recombination of the Primeval Plasma." In: *The Astrophysical Journal* 153 (July 1968), p. 1. DOI: 10.1086/149628.

[186] Jack O. Burns et al. "A Space-based Observational Strategy for Characterizing the First Stars and Galaxies Using the Redshifted 21 cm Global Spectrum." In: *The Astrophysical Journal* 844.1 (2017), p. 33. DOI: 10.3847/1538-4357/aa77f4. URL: https://dx.doi.org/10.3847/1538-4357/aa77f4.

[187] Jack O. Burns et al. "Probing the first stars and black holes in the early Universe with the Dark Ages Radio Explorer (DARE)." In: *Advances in Space Research* 49.3 (2012), pp. 433–450. ISSN: 0273-1177. DOI: https://doi.org/10.1016/j.asr.2011.10.014. URL: https://www.sciencedirect.com/science/article/pii/S0273117711007472.

[188] Mayuri Sathyanarayana Rao et al. "PRATUSH experiment concept and design overview." In: *Experimental Astronomy* (2023). ISSN: 1572-9508. DOI: 10.1007/s10686-023-09909-5. URL: https://doi.org/10.1007/s10686-023-09909-5.

[189] J. Cumner et al. "Radio Antenna Design for Sky-Averaged 21cm Cosmology Experiments: The REACH Case." In: *Journal of Astronomical Instrumentation* 11.01 (2022), p. 2250001. DOI: 10.1142/S2251171722500015. URL: https://doi.org/10.1142/S2251171722500015.

[190] Marcin Sokolowski et al. "BIGHORNS - Broadband Instrument for Global HydrOgen ReioNisation Signal." In: *Publications of the Astronomical Society of Australia* 32 (2015), e004. DOI: 10.1017/pasa.2015.3.